Monika Gabernig, BSc

Surface structuring and microstructure development of a metastable beta-titanium alloy for biomedical application prepared by an electron-beam technique

MASTER'S THESIS

to achieve the university degree of

Diplom-Ingenieurin

Master's degree programme: Technical Physics

submitted to

Graz University of Technology

Supervisor

Assoc.Prof. Dipl.-Phys. Dr.rer.nat. Wolfgang Sprengel

Institute of Materials Physics

Co-Supervisor
Dr.techn. Fernando Gustavo Warchomicka
Institute of Materials Science and Welding

Graz, June 2016

AFFIDAVIT

I declare that I have authored this thesis independently, that I have not used other than the declared sources/resources, and that I have explicitly indicated all material which has been quoted either literally or by content from the sources used. The text document uploaded to TUGRAZonline is identical to the present master's thesis.

Date		Signature

Abstract

Titanium and titanium alloys are standard materials for dental and orthopaedic implants because of their good biocompatibility, high corrosion resistance, high strength to density ratio, relatively low elastic modulus and good fatigue strength. The surface topography of implants can influence the bone response and plays an important role to improve bone anchorage of implant materials. The electron beam technique enables a controlled and precise creation of designed surface structures and represents a promising possibility to optimise the surface of implant materials.

In this work, a surface structuring of commercial pure titanium grade 2 (TiGr2) and metastable β-titanium alloy Ti15Mo is carried out by electron beam (EB) technique. Cytocompatibility tests with osteoblast cells (MC3T3-E1) are performed on structured and ground (4000 SiC paper) Ti15Mo plates to investigate the influence of the surface condition on the cell behaviour. The influence of the structuring process and process parameters on the surface and the microstructure of the material is investigated using microstructure analysis and topography observations.

The rapid deflection of the beam leads to a shifting of molten material which enables the creation of structures on the surface. The generated figures appear homogeneous and show no defects or pores.

Different roughness values can be obtained by utilisation of specific structures and process parameters for Ti15Mo.

Cell experiments reveal a positive cell behaviour on structured Ti15Mo surface. The cells are evenly distributed, exhibit a polygonal morphology and anchor to the surface by formation of elongated actin filaments (filopodia). Furthermore, a proliferation after longer cultivation time is observed.

The structuring of the surface by EB process leads to a change in the microstructure of Ti15Mo and a formation of different distinguishable zones divided in structured zone (molten region), heat affected zone and base material. No indication for α-phase precipitation can be found. The formation of ω_{iso}-phase in each of these zones leads to increased hardness values compared to the base material in as-delivered condition.

The development of the microstructure of structured Ti15Mo is investigated by applying different heating rates and ageing temperatures. These heat treatment parameters have a strong influence on the distribution, amount and size of α-lamellae within the developed α+β-structure and thus, also on the obtained hardness values.

Kurzfassung

Titan und Titanlegierungen finden aufgrund ihrer ausgezeichneten Biokompatibilität, hohen Korossionsbeständigkeit, hohen spezifischen Festigkeiten, relativ niedrigen E-module und hohen Dauerfestigkeitswerten unter anderem Anwendung im Bereich der Zahnprothetik und als orthopädische Implantate. Die Oberflächentopographie beeinflusst die Reaktion mit dem umgebenden Knochen und kann entscheidend zur Verbesserung der Verankerung des Knochens auf der Implantatoberfläche beitragen. Die Strukturierung mittels Elektronenstrahl erlaubt die kontrollierte und präzise Erzeugung entworfener Strukturen und stellt eine vielversprechende Möglichkeit zur Optimierung der Oberfläche von Implantaten dar.

Im Zuge dieser Arbeit wurden die Oberflächen von Reintitan (Grade 2) und einer metastabilen β-Titanlegierung, Ti15Mo, mittels Elektronenstrahltechnik strukturiert. Untersuchungen der Zytokompatibilität wurden unter Verwendung von Osteoblastzellen (Zelllinie: MC3T3-E1) auf strukturierter und geschliffener Ti15Mo Oberfläche durchgeführt, um den Einfluss unterschiedlicher Oberflächen auf das Zellverhalten zu untersuchen. Der Einfluss des Strukturierungsprozesses und Prozessparameter auf die Oberfläche und Mikrostruktur der Proben wurde mittels Topographiebeobachtungen und Mikrostrukturanalyse untersucht.

Durch die rasche Ablenkung des Elektronenstrahls erfolgt eine Verschiebung des aufgeschmolzenen Materials, wodurch Strukturen auf der Oberflächer erzeugt werden können. Die auf diese Weise gebildeten Figuren waren homogen und zeigten weder Defekte noch Poren.

Die Verwendung von bestimmten Strukturen und Prozessparametern ermöglicht die Erzeugung von unterschiedlichen Rauheiten auf Ti15Mo.

Zellen zeigen ein positives Verhalten auf der strukturierten Ti15Mo Oberfläche. Sie sind gleichmäßig verteilt, zeigen eine polygonale Morphologie und sind über lange fadenförmige Aktinfilamente (Filopodia) mit der Oberfläche verankert. Weiters ist eine Proliferation der Zellen nach längerer Kultivierungszeit erkennbar.

Die Strukturierung mittels Elektronenstrahl führt zu einer Veränderung der Mikrostruktur im Material und zur Ausbildung von drei unterscheidbaren Bereichen: Strukturierte Zone (Aufgeschmolzener Bereich), Wärmeeinflusszone und Grundmaterial. In allen drei Bereichen konnten keine Anzeichen für die Bildung von α-Phase gefunden werden. Die leicht erhöhten Härtewerte im Vergleich zum Grundmaterial im Lieferzustand sind auf die Bildung von ω_{iso}-Phase in allen drei Bereichen zurückzuführen.

Durch Wärmebehandlungen von strukturierten Ti15Mo Proben kann der starke Einfluss unterschiedlicher Heizraten und Glühtemperaturen auf Verteilung, Anzahl und Größe der sich ausbildenden α-Lamellen und deren Einfluss auf die Härte untersucht werden.

Acknowledgements

Contents

1 Introduction

Permanent orthopaedic devices, e.g., knee or hip replacements, and implants for fixation of complex fractures gain in importance in modern medicine. Unfortunately, the application of medical implants can cause undesired effects and complications, whereby the postoperative infection in the vicinity of the implant occurs most frequently. This complication is caused by a too low tissue adherence at the implant/tissue interface which can result in a sliding motion of the implant. This leads to mechanical irritations and the formation of a capsule. It is possible for bacteria to spread and multiply within the liquid-filled cavity formed between this capsule and the implant. The bacteria spread leads to an infection. To prevent such complications a good and fast integration of the implant with the bone is essential. A clear influence of implant surface topography in the micrometer level on bone integration and cell behaviour is revealed [1, 2].

This work focusses on the surface structuring of the metastable β-titanium alloy Ti15Mo by an electron beam (EB) technique to improve the interaction between implant and biological environment. This titanium alloy class is capable of providing better deformability, increased corrosion resistance and lower modulus of elasticity when compared to established titanium alloys which is why this class has a particular significance in the development of new biomaterials. The aims of the current thesis can be summarised as:

- Obtaining information about the influence of different electron beam welding parameters on the creation of designed surface structures on Ti15Mo and TiGr2.

- Investigation of the connection between EB process parameters and selected surface structures on roughness values of Ti15Mo surface.

- Improvement of the understanding of the influence of surface structures on osteoblastic cell behaviour.

- Examination and understanding of the impact of the surface structuring process with the high energy electron beam on microstructure and hardness of Ti15Mo by investigations of

  - phase transformations and changes in microstructure and hardness occuring in Ti15Mo alloys during and due to heat treatments
  - structured Ti15Mo samples
  - the development of the microstructure and hardness values of structured samples due to heat treatments

2 State of the art

2.1 Biomaterials in general

"Biomaterial" is a generic term that covers a broad field of very different materials as well as different applications and requirement profiles. Regardless of the material type or application, the direct interaction between synthetic (or modified natural) materials and biological systems is the common thread. A definition of "biomaterial", endorsed by the Consensus Conference of the European Society for Biomaterials [3] is:

> ***"A biomaterial is a nonviable material used in a medical device, intended to interact with biological systems"***

The range of biomaterial applications in the medical sector is vast and includes such applications as joint and limb replacements, contact lenses, dental implants or artificial arteries and skin.
Biomaterials which are incorporated in the human body require special properties that assure that no negative interactions with living tissue can take place. The *biocompatibility* of a material is an important factor in this context. A definition of the term proposed by Williams in 1987 [3]:

> ***""Biocompatibility" is the ability of a material to perform with an appropriate host response in a specific application"***

The biocompatibility of orthopaedic implant material can be classified regarding the biological behaviour when in contact with living tissue. The following three different categories were defined according to the material induced tissue reaction phenomena by Heimke [4] :

- ""*bio-tolerant*," showing distance osteogenesis (bone formation with indirect contact to the material-implant is separated from the adjacent bone by a soft tissue layer);

- "*bio-inert*," showing contact osteogenesis (bone formation with direct contact to the implant material), and

- "*bio-active*," showing bonding osteogenesis (bone formation with chemical or biological bonding to the implant material)"

The three main classes to which typical biomaterials belong are **metals**, **ceramics-glasses-and glass-ceramics** and **polymers**.

Polymers represent the largest group of materials used in medicine. A distinction is made between synthetic (e.g., silicone) and natural (e.g., collagen) polymeric materials. They can be easily manufactured and provide a variety of different properties which enable their application in various areas. They are used in orthopedics, cardiovascular devices, hard and soft tissue replacements or dental applications. They offer good flexibility and stability but in general exhibit lower strength compared to metals. Examples of polymer

classes used are polyurethanes (PUs), silicones, and fluoropolymers like PVDF, FEP or PTFE ([5]).

The **ceramics, glasses and glass-ceramics** biomaterial class includes a wide range of inorganic/nonmetallic compositions. These materials have been essential for many applications in medical industry e.g., eyeglasses, thermometers and diagnostic instruments. Ceramics are also used in dentistry. One example is zirconia (ZrO_2) which is used for bridges, dental veneers and crowns. Ceramics which are used in traumatology and orthopedic surgery as bone tissue substitutes are primarily of tricalcium phosphate (TCP), glass ionomer or hydroxyapatite origin. This material class so far has been identified to be non-toxic. Ceramics show a bio-inert or bio-active behaviour [5, 6, 7].

Metals like stainless steels, cobalt-base alloys, titanium and titanium alloys are used in orthopaedics. Examples of application fields include trauma and spinal fixation devices, replacement spinal discs and cardiovascular stents. They also have been applied for joint replacements like knees, shoulder or hip replacements [8].

Metals used for orthopaedic implants have to cover a wide spectrum of properties: excellent resistance to corrosion (degradation), high wear resistance (important for minimisation of debris generation), low modulus of elasticity to minimise or prevent bone resorption ("stress shielding effect"), and a biocompatible composition which should prevent an adverse tissue reaction [9].

Because of its moderate mechanical properties and good corrosion resistance, *stainless steel* is often applied for implants that are designed to help in fracture repair e.g., bone screws, pins, rods and bone plates. However, even for stainless steel corrosion occurs in the hostile human body fluid environment which determines their application to only temporary implants.
Co-based alloys e.g., Co-Cr-Mo and Co-Ni-Cr-Mo are also strong, hard and show good corrosion resistance. Furthermore, they show good fatigue strength and wear resistance, which is why they are used for long service life - fracture repair implants and long term protheses like artificial joints [7, 9, 10].
Titanium and titanium alloys show superior biocompatibility and resistance to corrosion by body fluids compared to stainless steel and Co-based alloys. The high strength to density ratio is another benefit of this material class [9]. The outstanding corrosion resistance of titanium and titanium alloys is the result of stable protective surface films consisting basically of stable oxides such as TiO_2, Nb_2O_5, Zr_2O_5, Al_2O_3, and MoO_2 or MoO_3, which are very insoluble in biological fluids [11, 12]. An additional advantage of titanium and titanium alloys is their low elastic modulus in comparison with stainless steel and Co-based alloys. The values for titanium alloys are more comparable with the elastic modulus of bone which is generally between 17 and 28 GPa [9, 13] (Fig. 1).
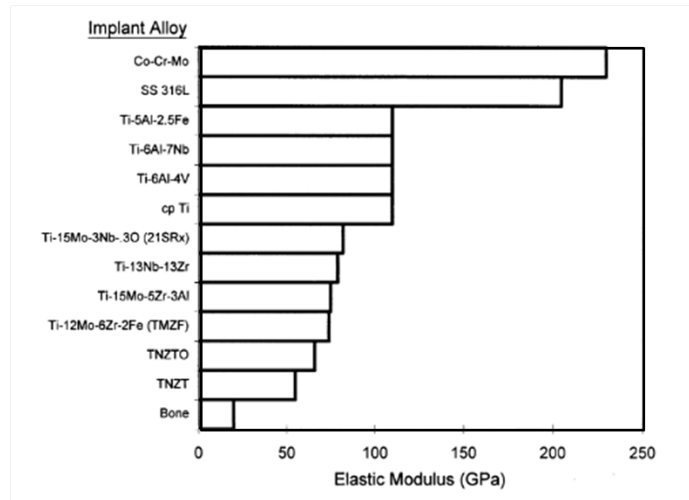
Figure 1: Modulus of elasticity values of orthopaedic alloys and natural bone. [9]

This property is important for hard tissue replacements where long term experience indicates that a resorption of the bone and eventually implant loosening can result from an insufficient load transmission from the artificial implant to the adjacent bone. This phenomenon, which is called "stress shielding" is caused by the difference in elastic modulus between hard tissue implant and bone [8, 9].

Furthermore, titanium is part of a small group of materials which, when placed in direct contact with healthy bone, does not induce the creation of a fibrous tissue barrier. This *bio-inert* behaviour permits the growth of the bone close to the implant surface, whereby filling of possibly deliberately introduced pores or grooves is enabled and a more firmly embedding of the material can be obtained which is a special benefit for dental protheses. Figure 2 depicts a human cheek bone in which a titanium plug implant is embedded. An artificial tooth can be screwed into the titanium implant [14].
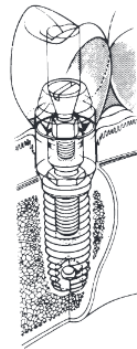
Figure 2: Human cheek bone with implanted titanium plug including an artificial tooth screwed in. [14]

Titanium alloys are also used for the fabrication of fracture fixation implants like cannulated bone screws, spinal clamps, intramedullary nails and other implants where a high resistance to stress loading is demanded.

The high strength combinations and low modulus of elasticity, offered by titanium alloys, are ideal for titanium elastic nails with small cross-section that have been developed for children.

Furthermore, titanium alloys are applied for external fixation clamps and assemblies. Thereby low weight, nonmagnetic clamps with high strength can be created.

2.2 Titanium alloys for biomedical application

Pure titanium crystallises at low temperatures in a modified hexagonal closed packed (hcp) crystal structure, known as α-titanium. The high temperature phase crystallises in a body centred cubic (bcc) structure, called β-titanium. The allotropic transformation occurs at a transus temperature of (882 ± 2)°C for pure titanium.

Figure 3 shows the atomic unit cells of the two different crystal structures with highlighted most densely packed planes.
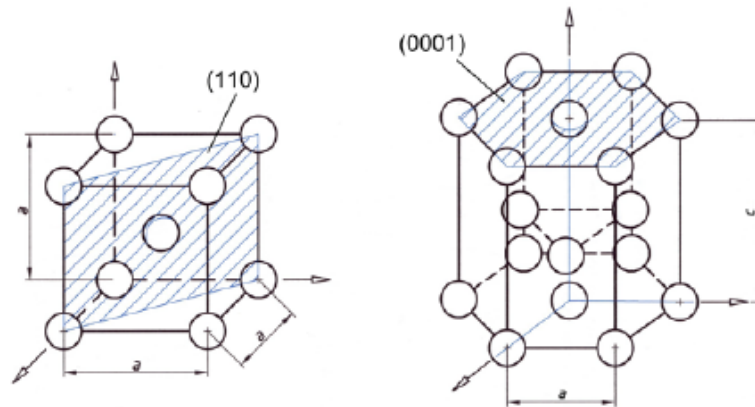
Figure 3: Crystal structure of the bcc β- and hcp α-phase (adapted from Ref. [15]).

The number of slip systems in a crystal is determined by the number of slip planes multiplied by the number of slip directions and is equivalent to the number of dislocation glide possibilities in the crystal lattice. For plastic deformation, these directions and planes of highly dense packed atoms are energetically most favourable. According to the von-Mises criterion at least 5 independent slip systems are necessary to enable a homogeneous plastic deformation of metals. The number of slip systems is 12 for the bcc lattice while it is only 3 for the hcp crystal structure, which can be an explanation for the limited plastic deformability of hcp α-titanium compared to bcc β-titanium.

The lattice parameters of the hcp α-phase unit cell at room temperature are a = 0.295 nm and c = 0.468 nm, which leads to a c/a-ratio of 1.587. However, the ideal ratio for the hcp structure is c/a = 1.633, which is a little bit higher than the ratio for the α-phase. According to Ref.[15] the lattice parameter of the bcc β-phase is a = 0,332 nm at a temperature

of 900°C. By cooling from the β-phase field, a transformation of the most densely packed {110} bcc β-phase planes into the basal planes {0001} of the hcp α-phase occurs. The slightly larger distances between the atomic centres in the hcp α basal planes compared to the corresponding distances between the {110} planes in the bcc lattice causes a slight atomic distortion during the β /α-phase transformation. This leads to a contraction of the c - axis relative to the a - axis of the hcp lattice, which causes a reduction of the c/a ratio below the ideal value for the close packed hexagonal structure. A little macroscopic increase in volume can be observed during cooling at the β/α-phase transition.

2.2.1 Classification of titanium alloys

The β-transus temperature, defined as the lowest equilibrium temperature at which the material consists of 100 % β-phase, can be altered by the presence of alloying elements. A distinction is made between *neutral-*, *β-* and *α-stabilising* elements.
Figure 4 depicts the influence of alloying elements on the phase formation as seen in the phase diagrams (schematically) of titanium alloys.
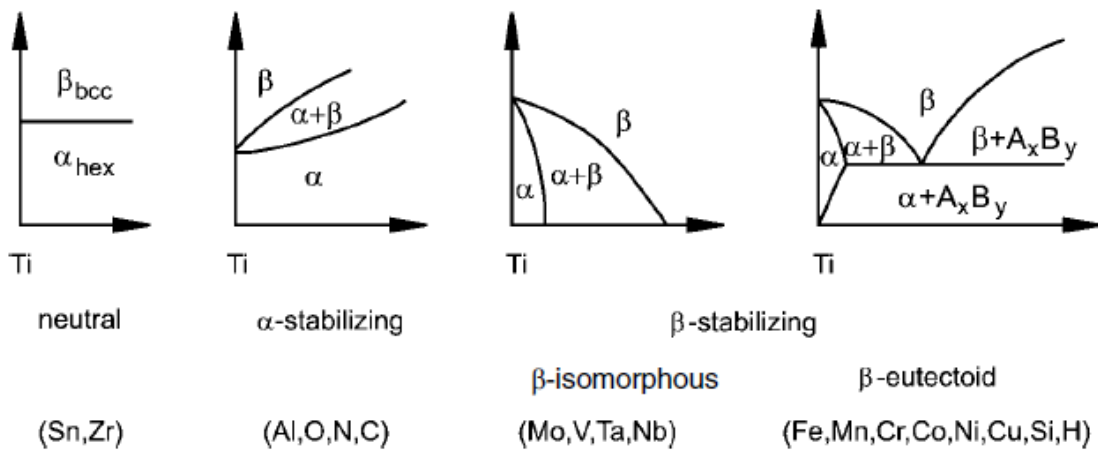
Figure 4: Alloying element influence on phase diagrams of titanium alloys. [15]

Whereas *neutral* elements (Sn, Zr) have only little influence on the β-transus temperature, *β-stabilising* elements like Mo, V, Ta, Fe or Mn have the ability to lower this characteristic temperature. They are subdivided into β-isomorphous and β-eutectic elements. The presence of *α-stabilising* elements (Al, C, O, N), extends the region of existence of the α-phase to higher temperatures and additionally causes the formation of a two-phase (α+β) region [15].

A classification of titanium alloys on the basis of the amount of *β-*or *α-stabilising* elements in the alloy can be done (see Fig. 5).
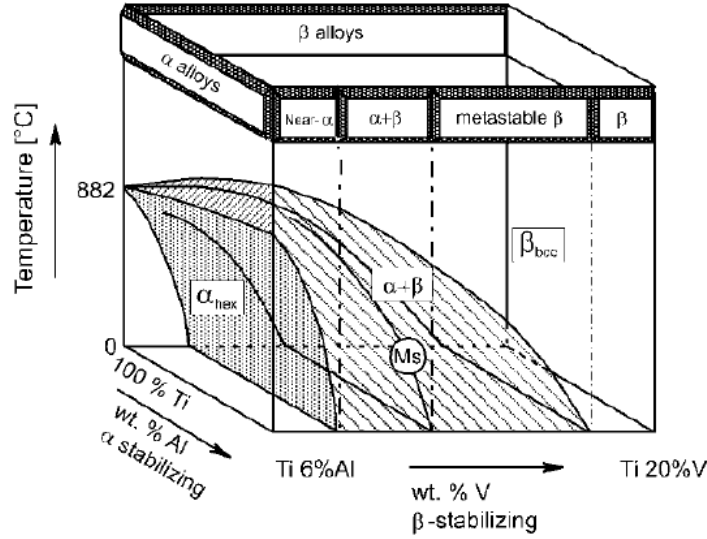
Figure 5: Illustration of the titanium alloy classification with the help of a 3 dimensional phase diagram (schematically). [15]

Pure titanium, and titanium alloys which contain only α-stabilising or neutral elements, belong to the class of **α-alloys**. If a small amount of β-stabilising elements is present, the alloy is denoted as **near-α-alloy**. This group is followed by the region of **α+β-alloys**. The α+β-alloy class, which is the most widely used one, exhibits a β-volume fraction range from about 5 to 40 % at room temperature.

In these classes, the β → α-phase transformation can occur martensitically during quenching from the β-phase field. Hexagonal martensite known as α'-phase can arise in two morphologies: "Massive" martensite (also called "1 ath" or "packet martensite") which occurs in pure titanium, very dilute titanium alloys and in alloys which exhibit a high martensitic transformation start temperature (M_S) and "acicular" martensite appearing in alloys with higher solute content with a lower M_S- temperature. With increasing amount of β-stabilising element, the hexagonal crystal structure becomes distorted and orthorhombic α''-phase is formed.

The class of **β-titanium alloys** is defined as titanium alloys containing enough amount of β-stabilising elements to suppress a martensitic transformation during quenching from a temperature above β-transus, which means that the more ductile β-phase can be retained in either a metastable or stable condition at room temperature. The stability of the β-phase can be described by the Mo-equivalent, in which the individual influence of β- stabilising elements like Mo, V, Fe, Cr, Nb, etc. is included. It is calculated as follows:

$$[Mo]\,eq = [Mo] + 0.2\,[Ta] + 0.28\,[Nb] + 0.4\,[W] + 0.67\,[V] + 1.25\,[Cr] + 1.25\,[Ni] + 1.7\,[Mn] + 1.7\,[Co] + 2.5\,[Fe]$$

A molybdenum equivalent ≥ 10 has been defined to stabilise the β-phase at room temperature. This alloy composition, i.e., at the intersection point of Ms line and room

8

temperature axis, limits the region of **metastable β-alloys** on one side whereas the alloy composition at a similar intersection point of the β-transus line is the limit on the other. Upon ageing, a second phase (usually α-phase) will precipitate in metastable β-titanium alloys. β-alloys with a higher amount of β-stabilising elements, are **stable β-alloys**. They cannot be hardened by heat treatments [12, 14, 15].

2.2.2 Phase transformations in metastable β-alloys

Athermal formation of the ω-phase during quenching

The formation of ellipsoidal shaped metastable $\omega_{athermal}$-particles can occur in metastable β-titanium alloys containing a required level of β-stabilising elements during quenching from the β-phase field. This pure displacive, diffusionless transformation can be explained by a lattice collapse mechanism. During the transformation the composition of the parent matrix is retained. The fact that the formation of athermal - ω can not be suppressed, even through ultrahigh quench rates suggest that the transformation arise without any thermal activation. Furthermore, the transformation is reversible which is another evidence for its athermal nature [16].
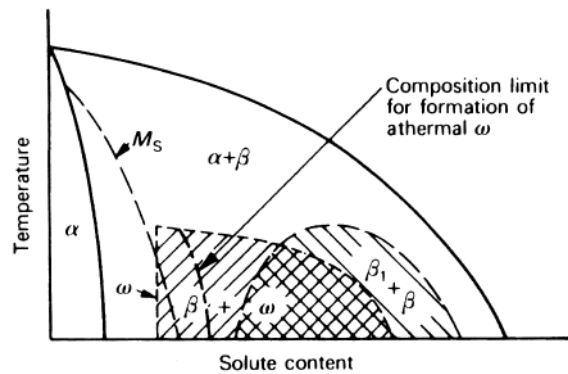
Figure 6: The β isomorphous alloy phase diagram, with the martensite (Ms) start temperature curve and ranges of stability for ω-, β- and β_1-phase are depicted. [14]

Isothermal formation of the ω-phase during ageing

The isothermal formation of ω-phase can occur on ageing at low temperatures in a temperature range of about 100-500°C. In this thermal activated process a compositional partitioning process in the parent β-phase is followed by a lattice collapse mechanism within a solute lean zone [16]. The ω_{ath}-phase, which is possibly existing in the material after quenching, undergoes compositional changes during ageing. Then ω_{iso}-particles which are depleted in the beta stabilising element form and replace the ω_{ath}-phase. An increase of

the isothermal holding time is accompanied by an increase of the volume fraction and growth of ω_{iso}-particles, which indicates a thermal activated transformation mechanism is underlying. The lattice correspondence between the bcc β-phase and ω_{iso}-structures were observed to be the same as in the case of the β→ω_{ath}-phase transformation. This fact suggests that the isothermal formation occurs by an atomistic mechanism, which is the same as that for the athermal precipitation. The stability range of the ω-phase including the limited area of ω_{ath}-phase formation is depicted schematically for a β-isomorphous phase diagram in Fig. 6.

Figure 7 depicts the β- to ω-phase transformation process. The orientation relationship between the β- and ω-phase has been determined as:

$$\{111\}_\beta \,||\, (0001)_\omega$$
$$< 1\bar{1}0 >_\beta \,||\, < 1\bar{2}10 >_\omega$$
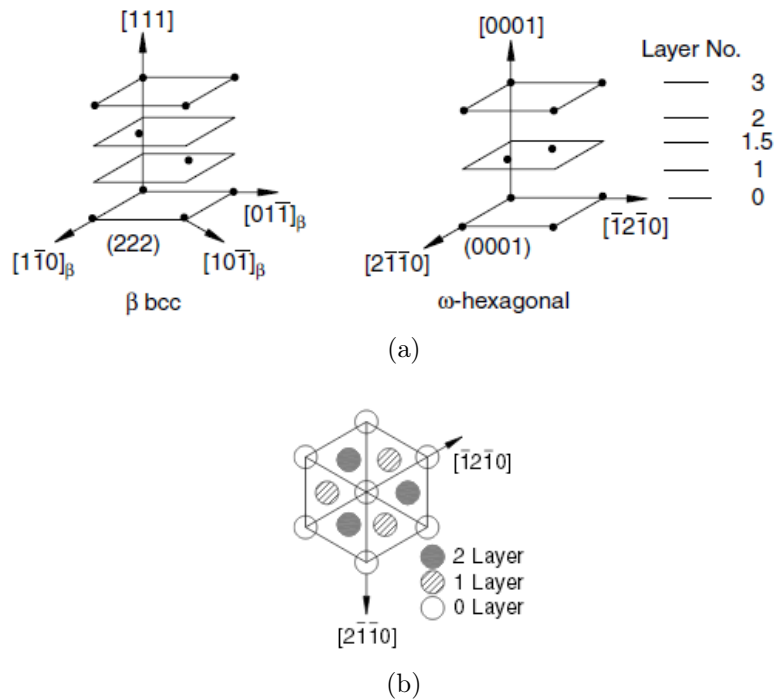
Figure 7: a) Sketch of the collapse mechanism of β planes, b) Sixfold symmetry formed by completely collapsed (222) planes. [16]

On the left side of Fig. 7a the ABCABC...stacking sequence of the $(222)_\beta$ planes of the β- phase bcc structure is depicted. This bcc structure exhibits threefold axes along the <111> direction. According to the most common model the formation of the ω-phase

10

can be created by the collapse of a pair of $(222)_\beta$ planes (labeled as 1 and 2 in Fig. 7a) of the bcc structure to the intermediate position (labeled as 1.5), remaining the next planes (0 and 3) undistorted, collapsing the following pair of planes and so on. In case of a complete collapse, a sixfold rotation symmetry arises around the <111> direction (see Fig. 7b) along which a lattice collapse occurs and a hexagonal ω-structure is obtained. If the collapse is incomplete, the resulting ω-phase is associated with a trigonal structure.

The equivalent positions of the atoms in the ω-structure unit cell are 000; 2/3 1/3 (1/2–z); 1/3 2/3 (1/2+z), with z = 0 for the ideal hexagonal ω-structure. The non-ideal ω-structure with trigonal symmetry is defined by $0 < z < 1/6$. A diffuse intensity distribution in X-ray, neutron and electron diffraction patterns has been ascribed to non-ideal structures of ω, while the ideal hexagonal ω-structure leads to discrete diffraction intensity maxima [16].

The extend of the collapse of β planes to form ω embryos and its additional growth is determined by the solute (β-stabiliser) concentration. For a metastable β-titanium alloy (Ti-15wt%Mo), the observation of diffuse streaking in the SAD pattern of ω_{ath} and the appearance of discrete spots in the ω_{iso}-diffraction pattern is reported in Ref.[17]. In this system the degree of displacement is restricted by the content of the strong β-stabiliser Mo, which leads to a trigonal, three fold symmetry of the ω-phase in the "as quenched state". A completion of the collapse occurs as a result of ageing, due to out-diffusion of Mo from the ω-phase into the enclosing β-matrix which leads to a formation of the ideal hexagonal ω-structure.

Two types of morphologies have been found for ω_{iso}-particles. Depending on the *lattice mismatch* between the β- and ω-phases in a system considered, ω_{iso}-particle have either an *cuboidal* or an *ellipsoidal* shape. In low misfit ($< 0.5\%$) systems, e.g., Ti-Mo [18], ω can precipitate with an ellipsoidal morphology, while for large misfits ($> 1\%$) (e.g., for Ti-Fe or Ti-V) the ω-phase becomes cuboidal [12, 16].

An increase of the amount of nanometer sized ω-particles leads to an increase of the hardness values in ω forming titanium alloys [17, 18]. Coherency strains induced by ω-phase have been identified as one possible reason for the strengthening effect [17]. However, these particles can cause embrittlement because dislocations have little or no mobility in the ω-phase. The restriction of slip leads to a raise of the β-phase strength above the value for brittle fracture. The slip restricting capacity of the ω-phase depends on its thickness, rigidity and the mean free path between the particles [14, 19]. [20] reports that very fine ω_{ath}-particles in as-quenched metastable β-titanium alloys do not lead to brittleness but on the contrary can have a positive influence on the ductility. Furthermore, a connection between the formation of ω-phase and an increase of the elastic modulus could be observed [19] .

Precipitation of the α-phase

Mechanical properties of β- titanium alloys are strongly influenced by the size, morphology, volume fraction and distribution of the precipitated α-phase. A variety of microstructures

can be obtained by the transformation of the β phase either during continuous cooling or in an isothermal condition within the α+β-phase field.

Typical classification of α-phases makes reference to the nucleation site and the order of appearance of α-phase during **continuous cooling from the β-phase field.**
At first *grain boundary allotriomorph a-phase* (α_{GB}) starts to nucleate at and grow primarily along high-angle grain boundaries of the parent β phase.
Then lath-shaped *Widmanstätten grain boundary a-plates* (α_{WGB}) start to appear. They can form either by branching out from GB α-phase or by nucleation at grain boundaries and growth towards the grain interior. Growth of α_{WGB} in a group and resulting formation of a colony of parallel plates is often found.
The phase *a-Widmanstätten Intragranular* (α_{WI}) is the hardest and usually the last to form. It nucleates and grows in the interior of β grains and can form either in a group or in an isolated manner [16, 21].
Figure 8 shows examples of the three types of α-phase obtained for a near β-titanium alloy (Ti17) (according to Ref.[21]).

(a)   (b)
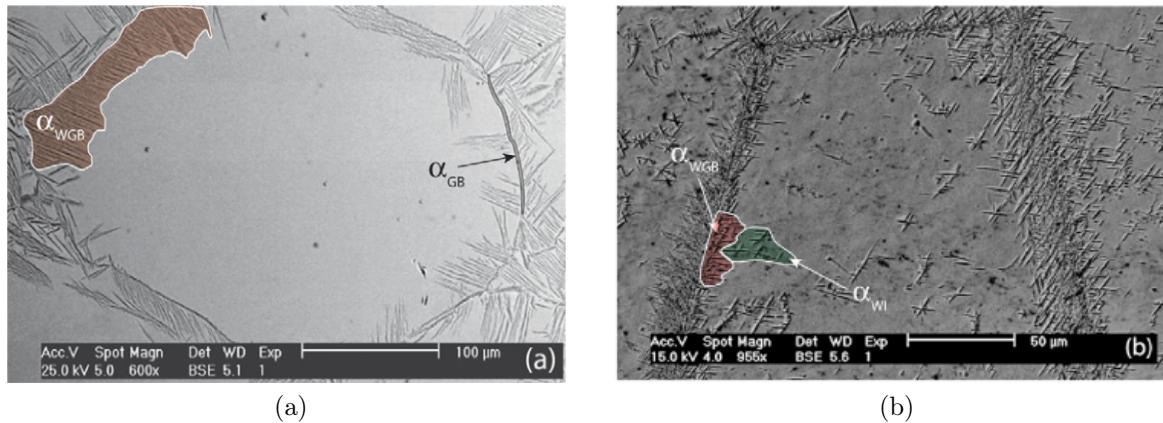
Figure 8: SEM images: a) Example of α_{GB} layer (surrounded by black line and marked by arrow) and α_{WGB} colony (surrounded by white line and highlighted in red), b) α_{WGB} and α_{WI} surrounded by white lines and highlighted in red and green respectively. [21].

The microstructure of metastable β-titanium alloys can be developed by **thermomechanical processing**, which usually consists of a hot working process followed by a heat treatment. Figure 9 shows an examples of a thermomechanical processing route. After homogenisation (I) the deformation can be carried out either in the α+β-or in the β-phase field (II) whereby the first enables the creation of smaller β grain sizes during the recrystallisation step (III). Depending on the chosen temperature for the final heat treatment in the α+β-phase field an additional classification of the α-phase regarding the morphology can be done. The coarse *primary a-phase* (α_P) forms at relatively high annealing temperatures (see IVa in Fig. 9), slightly below β-transus, predominantly at prior β grain

boundaries. A high amount of hot working leads to a formation of α_P-phase with globular shape, whereby a needle-like shape develops without working. Fine *secondary a-phase* (α_S) starts to nucleate in the form of thin plates at grain boundaries and intra granularly during intermediate temperature ageing (typically 500°C-600°C) (see IVb in Fig. 9). Depending on its volume fraction and size, this α_S-phase has a significant strengthening effect [12, 15, 22].
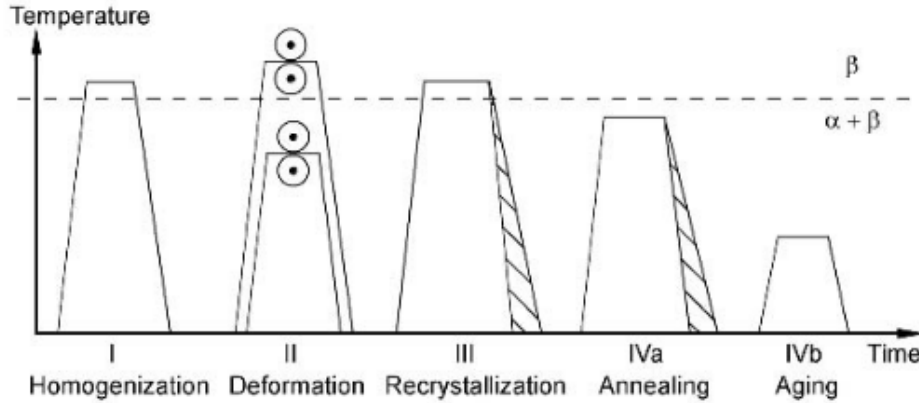
Figure 9: Schematical processing route for β-annealed microstructure of β-titanium alloys. [12]

The β→α-phase transformation can also be mediated through the ω-phase if a β-solutionization treatment is followed by a quenching of the alloy to retain the β-phase at room temperature. In this case the formation of uniformly distributed fine scale homogeneous α-phase on a subsequently performed ageing at low temperatures can be associated with ***ω-phase assisted nucleation***, whereby ω-particles, present in the β quenched alloy, act as nucleation sites for the α-phase [16, 23]. Such very fine scale α-precipitates can cause an increase in hardness of the β-titanium alloy. Because of their small size they are not able to deform plastically, which is why they act as undeformable, hard particles. Large α-plates, e.g., obtained by an annealing step at high temperatures in the α+β-phase field, have a reduced hardening efficiency, because they are big enough to deform plastically [12, 24]. According to Ref.[18] the elastic modulus of β-titanium alloys is also dependent on the α-phase. An increase of the modulus of a metastable β-titanium alloy (Ti15Mo) with increasing volume fraction of refined-secondary α-phase, which plays a more dominant role in this context than the ω-phase, was reported.

In the case of ω-assisted nucleation, for systems with a *high lattice misfit* between the ω- and the β-phase, where ω_{iso}-particles show a *cuboidal morphology*, an α-phase nucleation at dislocations on the β/ω-interface has been reported [25]. For *low ω/β misfit* systems with *ellipsoidal ω*, a controversy regarding the α-phase formation mechanism exists. According to literature [26] a nucleation of α-phase near, but a certain distance away from

13

the ω/β-interface was reported in Ti-6.8Mo-4.5Fe-1.5Al (wt.%) low-cost β (LCB) alloy. This is caused by local rejection of alloying elements which act as ω-destabilisers but as α-stabilisers at the same time (such as Al for this type of titanium alloy) during the isothermal ageing of ω-precipitates, whereby a nucleation of the α-phase in the vicinity of the ω-precipitates is supported. According to a high resolution electron microscopy study on the LCB alloy [23] a displacive transformation within the core of ω-precipitates leads to the formation of α-plates.

Figure 10 depicts the nucleation and growth mechanism of the α-phase schematically. After the nucleation of α-phase from the ω-phase caused by a displacive transformation, the α-phase grows by ω-phase consumption, which leads to a plate like morphology. After the total disappearance of the ω-phase the interface mobility between α- and β-phase governs the growth of the α-phase. The α-plate growth is limited in the coherent direction (lower mobility of the interface in the width direction) and faster in the incoherent direction (higher mobility of the interface in the length direction).
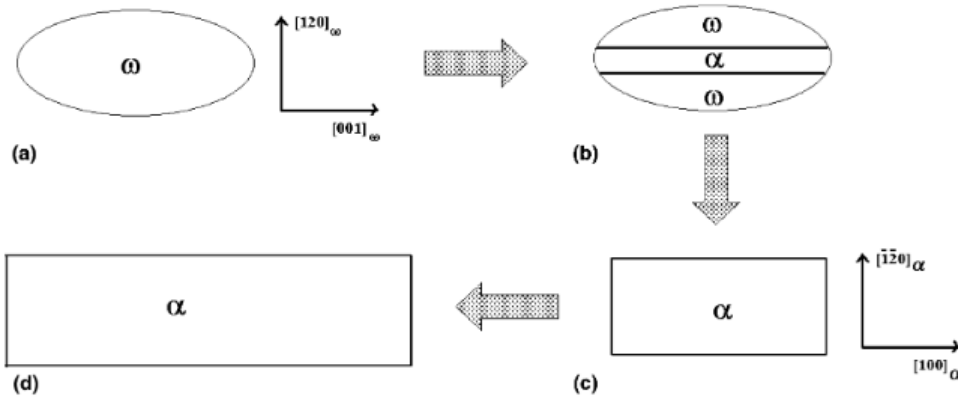
Figure 10: Nucleation and growth model of α-phase within the ω-phase: a) ω-particle acts as heterogeneous nucleation site, b) Growth of α-phase by consumption of the ω-phase, c) Disappearance of the ω-phase and d) Growth of α-phase from consumption of the β-phase. [23]

Decomposition of the β-phase

If the amount of β-stabilising elements in the alloy is high enough to prevent the formation of ω-phase during ageing at low temperatures, a separation of the β-phase into two bcc phases can occur (see Fig. 6). The differences between the phases, known as solute rich (β) and solute lean (β_1), are the solute content and the lattice parameters. The magnitude of distortion of the bcc lattice in the β_1-precipitates with respect to the lattice of the β_{rich} matrix is very small in this highly concentrated alloys. The phase separation results in a coherent mixture of the solute rich and solute lean β-phase [12, 14].

2.2.3 Advantages and areas of application of titanium alloys

About α-titanium alloys

Commercial purity (cp) titanium has long been used for biomedical devices like lead wires or cardiovascular stents. The material is also used for heart pacemaker cases or as carrier structure for artificial heart valves. Pure titanium type alloys are also one of the main materials used for implants in the dental field. An additional applicability are bone plates when strength requirements are not high [8, 12, 13].

Figure 11 shows an example of a bone plate implant consisting of cp titanium grade 3. The X-ray radiographs on the left hand side depict the broken bone before and after the fixing of the bone plate. The actual shape of the bone plate is illustrated by the schematic drawing in Fig. 11.
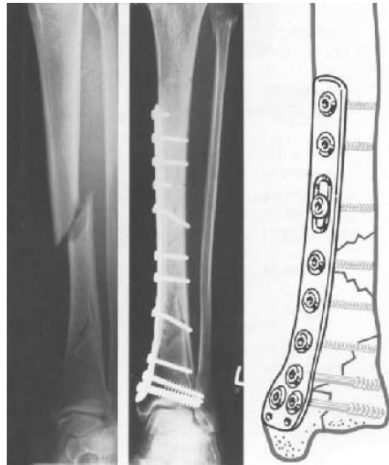
Figure 11: Bone plate implant consisting of cp titanium grade 3. [12]

About α+β-titanium alloys

Compared to commercially pure titanium (CP), α+β-titanium alloys offer less bending and tensile ductility but improved strength [11]. When higher strength bone plates are required, then the α-alloys are replaced with the α+β-titanium alloys e.g., Ti-6Al-4V and Ti-6Al-7Nb. However, the capability for contour creation is limited for both alloys which restricts the area of application to only fairy straight plates [11, 12].

The α+β-titanium alloys exhibit excellent fatigue behaviour which led to the application of these alloys in the total joint replacement sector. The alloy Ti6Al4V (extra low interstitial impurity content) ELI was early introduced in this area and it is the most widely used titanium alloy for biomedical devices. However, the use of this alloy is restricted because of the high cytotoxicity of V and tissue response of capsule type caused by Al [27] as well as due to the possible connection between the release of both V and Al ions with Alzheimer diseases and peripheral neuropathy [18].

Alloys Ti-6Al-7Nb and Ti-5Al-2.5Fe are two examples of V-free α+β-alloys, developed in the 1980's, which exhibit similar properties and microstructure as Ti6Al4V. Ti-15Sn-4Nb-

2Ta-0.2Pd alloy is one example of a recently developed V- and Al-free α+β-titanium alloy composed of non-toxic elements [12, 13].

About β-titanium alloys

In recent years there has been a large effort to develop new β-titanium alloys composed of non-toxic elements (Nb, Ta, Zr, Mo) as implant material. Figure 12 shows a comparison of elastic modulus values of α-, α+β-, and β-titanium alloys, with marked value for Ti15Mo. β-titanium alloys exhibit much greater biocompatibility compared to α- and α+β-titanium alloys because of their much lower elastic modulus values (between 55 to 85 GPa for recently developed β-alloys) which are more similar to that of bone (cf. "stress shielding"). They are also able to obtain higher strength and toughness balance in comparison to α+β-alloys.
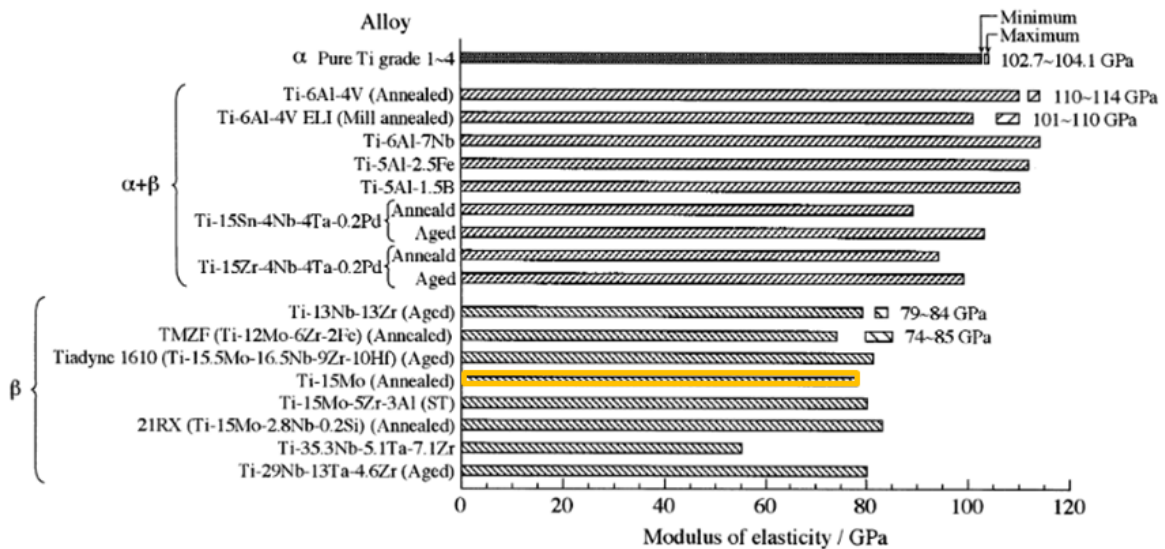
Figure 12: Comparison of elastic modulus values of different titanium alloys for biomedical application. [13]

Titanium alloys with a α+β-microstructure tend to have decreased notch sensitivity ratios compared to β-titanium alloys, as observed in Ti15Mo and Ti-15Mo-5Zr-3Al [11]. This property of β-titanium alloys is of advantage for large and small fragment plates, where the plates are exposed to reverse bending.

2.3   Surface modifications of titanium and titanium alloys

The combination of desirable properties enables the application of titanium and its alloys for many biomedical components and devices. However, not all of the clinical requirements can be fulfilled. Surface modifications are often performed to improve the chemical, biological and mechanical properties of titanium and titanium alloys for biomedical applications. Recent studies have shown that the corrosion resistance, wear resistance and biological properties can be improved by using suitable surface treatment techniques without changing the desirable bulk attributes of titanium and its alloys. A classification of surface modification technologies of the modified layer on the surface of the material can be made based on the formation principle into **mechanical**, **chemical** and **physical methods** [28].

- **Mechanical methods**

  Blasting, polishing and machining are widely used mechanical surface modification methods. They involve physical treatment by removal or by shaping of the material surface. The generation of specific surface topographies and grades of roughness are typical aims of mechanical modification [29].

- **Chemical methods**

  Chemical surface modification methods include biochemical modification, electrochemical (anodic oxidation) - and chemical treatment. During these processes biochemical, electrochemical and chemical reactions occur at the titanium/solution interface. The chemical reactions between the sample surface and the chemicals in the gas phase lead to the deposition of a non-volatile compound on the substrate during chemical vapor deposition (CVD). One further example of a chemical surface modification method is the sol gel-process where chemical reactions occur in the solution rather than at the interface between solution or gel and the sample surface [28].

- **Physical methods**

  In processes such as physical vapor deposition, ion implantation, glow discharge plasma treatment and thermal spraying no chemical reactions occur. These processes belong to the group of physical surface modification methods. The formation of surface modified films, coatings or layers on titanium or titanium alloys during this processes are mainly a product of the involved thermal, electrical and kinetic energy [29].

Influence of the topography on bone response

To ensure the efficacy and safety of implants over their useful life, a good integration

of the implant with the bone is essential. The surface condition (microtexture) of the implant is an important factor which must be controlled to establish secure osseointegration. Here the first interactions between the surface of the implant material and the surrounding tissue are crucial for tissue integration of the biomaterial. It contributes significantly to the clinical long-term success [7, 30]. A better stability during the healing process may conferred by a faster an stronger bone formation, whereby more rapid loading of the implant can be allowed [1].

The effect of the titanium surface topography on bone integration was analysed and it revealed a clear influence of the implant surface topography on the micrometer level on the bone response [1]. For smooth surfaces ($S_a{}^1 < 0.5$ µm) and minimal rough surfaces (S_a 0.5-1 µm) less strong bone response was observed compared to the response for rougher surfaces. In some studies moderately rough surfaces ($S_a > 1$-2 µm) showed stronger bone response than rough surfaces ($S_a > 2$ µm).

Studies about the relationship between surface morphology and *cell behaviour* revealed that special surface morphology is beneficial for cell proliferation and preferable to cell adhesion.
A possible example is a porous titanium surface with a proper arrangement of pores, which improves cell adhesion and proliferation and supports the mechanical lock of implants. Such porous surfaces can be produced by utilisation of LENS (laser engineered net shaping), which is a CAD and layer-based manufacturing method [31, 32].
However, regarding the definition of optimal surface properties to improve tissue response no overall consensus has been reached yet and several authors have reported different values for optimal surface roughness. For example Bächle et.al. [33] reports that osteoblastic MG63 cells show high proliferation and differentiation rate on regularly textured pure titanium surfaces with R_a (arithmetic root mean square) roughness values of around 4 µm. According to Ref.[34], investigation of blasted Ti substrate indicated that a fine surface ($R_a = 0.036$ µm) is inferior to a rough surface ($R_a = 5.347$ µm, or 3.685 µm) with regard to initial adhesion and differentiation of Osteoblast like cells. However, according to another study which examined the adhesion and proliferation behaviour of mouse and primary human osteoblastic cells on Ti6Al4V samples with varied surface roughnesses (R_a values from 0.16 µm to 3.4 µm) a lower adhesion and proliferation was observed on rough surfaces than on smooth ones [35]. In vitro experiments on Ti samples, modified per polishing and acid etching indicate a higher differentiation degree for roughness values between 0.50 µm and 0.77 µm compared to a smooth surface with $R_a = 0.15$ µm. Regarding cell proliferation the best results were obtained for a roughness value of $R_a = 0.50$ µm [2].

Wennerberg et.al. [1] summarised many works related to the use of different techniques for roughness determination and surface topographical characterisation. It is concluding that the comparison of roughness values is very difficult for different techniques.

---

[1]3D equivalent of the 2D roughness parameter R_a (arithmetic root mean square)

2.4 Electron beam technology for surface structuring

The electron beam technology enables a controlled surface structuring and represents a novel and promising possibility to optimise the surface of implant materials.
In the present work an electron beam of an electron beam welding (EBW) machine was used, whereby a beam of accelerated and electromagnetically focused electrons serves as the energy source to melt material. The working principle is depicted in Fig. 13.
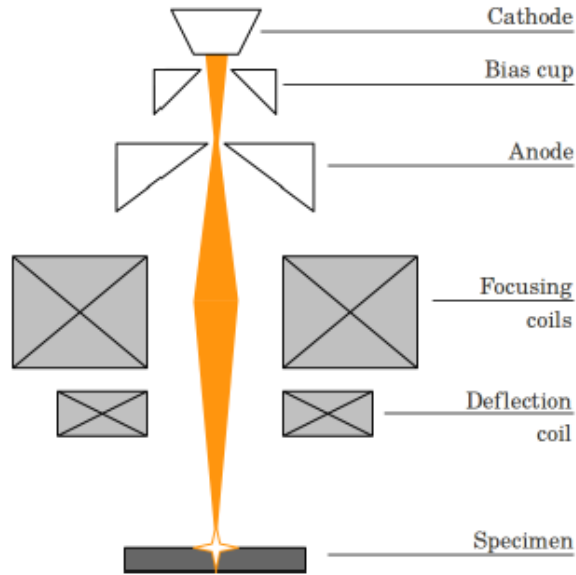
Figure 13: Schematic illustration of an EBW machine. [36]

The free electrons, supplied by the heated cathode (mostly tungsten) due to thermal emission, are accelerated in the direction of the anode, whereby an electric field between the two electrodes is the driving force. The electron current can be adjusted by varying the negative voltage of a control electrode (bias cup), also known as wehnelt cylinder. Depending on the level of the negative control voltage, the electrons can be repelled by the control electrode back towards the cathode, despite the applied acceleration voltage U_A and the effective emitting surface of the cathode can be reduced, which is accompanied by a reduction of the beam current I_B impinging on the workpiece. The two parameters beam current I_B and acceleration voltage U_A determine the beam power P_b (see Eq.1)

$$P_b = U_A \cdot I_B \tag{1}$$

For a typical acceleration voltage of 150 kV, electrons reach a speed of $2 \cdot 10^8$ m/s ($\hat{=}$ about two thirds the speed of light). The direct correspondence between the acceleration voltage and the kinetic energy of the electrons can be seen in the following equation:

$$E_{kin} = \frac{m_e \cdot v_e^2}{2} = e \cdot U_A \qquad (2)$$

where, E_{kin} is the kinetic energy of an electron with relative mass m_e and elementary charge e, accelerated to a velocity $\vec{v}_e$ by an acceleration voltage U_A. However, at this high velocities, relativistic effects become noticeable and the kinetic energy term $\frac{m_{e0} \cdot v_e^2}{2}$ with the electron rest mass m_{e0} has to be supplemented by a relative mass increase of the electrons of about 35% (see Eq. 3) [37]:

$$\frac{m_e \cdot v_e^2}{2} = \frac{m_{e0} \cdot v_e^2}{2} \cdot \frac{1}{\sqrt{1 - \frac{v_e^2}{c^2}}} \qquad (3)$$

After passing through the anode, the divergent electron beam gets focused using electromagnetic lenses. According to *Lorentz force law* $\vec{F} = q \cdot (\vec{v} \times \vec{B})$, with q representing the electrical charge of the particle ($\hat{=}$ elementary charge $-e$ for electrons), $\vec{v}$ the velocity of the particle and $\vec{B}$ the magnetic field strength, a particle with charge e, moving in an magnetic field $\vec{B}$ with velocity $\vec{v}$, experiences a force $\vec{F}$ acting perpendicular to $\vec{v}$ and $\vec{B}$. Thus, the flight paths of the electrons can be affected and a focusing of the electron beam to a small spot (focal point) can be achieved (see Fig. 14)
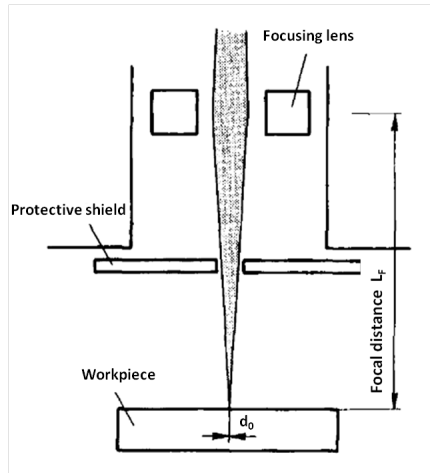
Figure 14: Focusing of the electron beam by electromagnetic lens (adapted from Ref. [38]).

Typical focal point diameters d_0 of (0.1-1.0) mm can be obtained when employing the electron beam welding. Power densities of about 10^7 W·cm^{-2} are achieved with this small focal diameter. To focus the electron beam on the workpiece surface, the current through the annular coils known as the *lens current* has to be varied. This lens current is the main determining factor for the focal length L_F (see Fig. 14) of the magnetic lens. The

focal length is inversely proportional to the square of the lens current ([38]).
The size of the beam diameter in the focal spot depends on the beam power P_b (determined by the current I_A and the voltage U_A) and the geometry related parameter beam divergence Θ_{full} (or focal distance L_F).
According to Fig. 15 the focal diameter decreases with increasing U_A and decreasing I_B ([38])
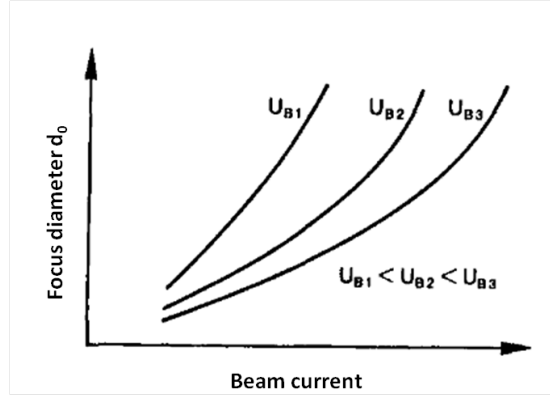
Figure 15: Effect of accelerating voltage U and beam current on the focus diameter d_0 (adapted from [38]).

In Fig. 16 the relation between the minimal focal diameter d_0, divergence angle (Θ_{full}) and the intensity of the beam is depicted.
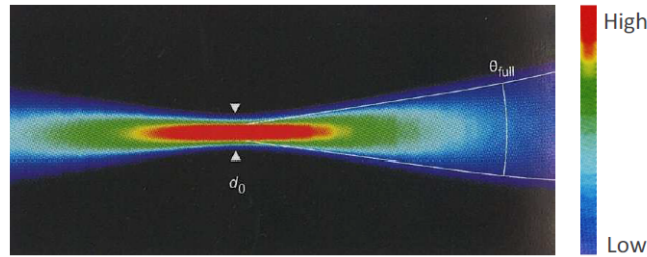
Figure 16: Intensity distribution along the electron beam (adapted from Ref.[39]).

The parameters divergence Θ_{full} and focal diameter d_0 are correlated and define the emittance ϵ, also known as beam parameter product, BPP,

$$\varepsilon\,[mm \cdot mrad] = \frac{d_0 \cdot \Theta_{full}}{4} \tag{4}$$

A decreasing focal length leads to increasing divergence and according to Eq. 4 to a

decreasing focal diameter, which is beneficial if a decreasing weld pool width is desired. The beam diameter for each divergence (focal position) can be calculated if the value for the emittance, which is a conserved quantity in this equation, is known [38, 39].

After passing the electromagnetic lens, the electrons enters the deflection system which can deflect the electron beam by application of a magnetic field. By means of the used deflection coils the direction of the electron beam can be shifted almost without inertia, which means that an instantaneous and very precise deflection can be achieved. The quasi simultaneous creation of two or more weld beads can be enabled by utilisation of this fast beam deflection function.

Creation of surface structures

The high power density which is transmitted into the material by the electron beam, causes a local melting and evaporation of the metal which results in the formation of a cavity, the so called "keyhole". Due to the high vapour pressure in the centre of the keyhole the molten material is pushed against the sidewalls of the cavity. When the beam moves along the surface during the welding process, the molten material flows to the back side of the electron beam and solidifies as depicted in Fig. 17a [38]. This movement of the melt causes an accumulation of material at the beginning of the weldment which results in a protrusion at this position and an intrusion at the end of the weldment. Figure 17b shows this resulting effect from a single beam swipe.

(a)   (b)
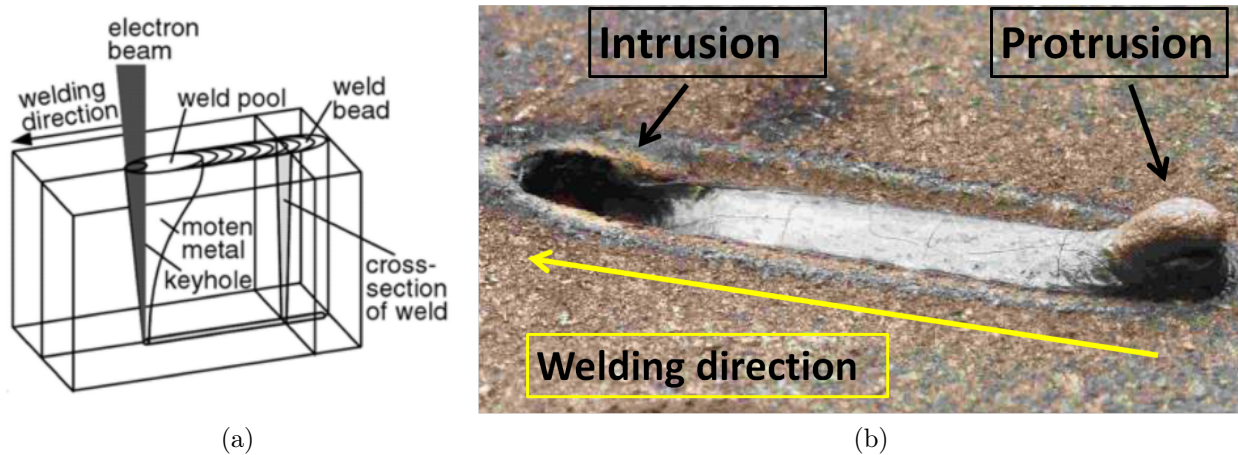
Figure 17: a) Scheme of the keyhole effect during welding [40], b) Resulting intrusion and protrusion effect from a single beam swipe (adapted from Ref.[41]).

By repeating the movement of the beam on the same path (depicted in Fig. 18) an increment of protrusions can be achieved, which is accompanied by a lowering of the intrusions. Protrusion patterns on the sample surface can be created when employing

22

this procedure. This effect of material transport was first described by Dance and Kellar in 2004 [42]. It was referred to as *surfi-sculpt* process.
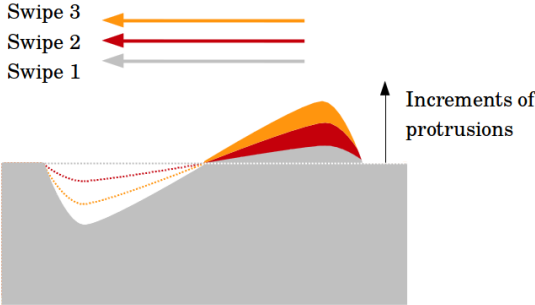
Figure 18: Schematic illustration of the keyhole effect of repeated beam swipes. [36]

Figure 19 shows an example of a "pin-like structure" which had been formed by the repeated passing trough of the cross as depicted in Fig. 19a. By moving the beam from the centre to the outer edges of the cross, material gets shifted from the outside to the inside which results in the creation of a "pin-like structure" (in Fig. 19b).

(a)

(b)
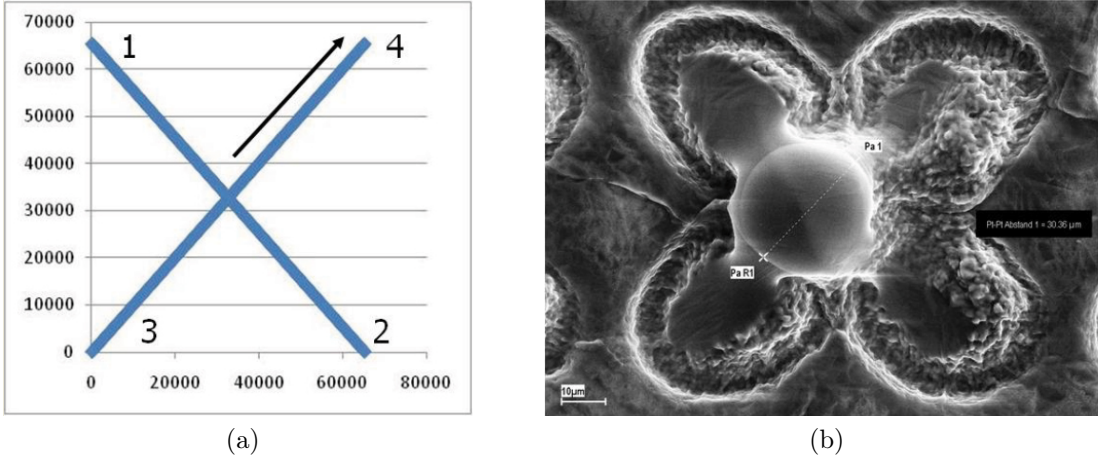
Figure 19: a) Beam deflection figure used for structure generation, b) SEM image of a "pin-like structure". [43]

A rapid deflection of the electron beam controlled by coordinate files enables the creation of complex surface structures. One possible way for the generation of the coordinate files is the application of routines, programmed with Matlab. A variety of different structure geometries (e.g., squares, circles, triangles and hexagons) and designs can be realised by the routines. A selection of criteria of designs for routines, programmed by Markus Stütz is listed below [36]:

- **Arm Number**

  Two structures with different arm numbers are depicted in Fig. 20. The number of arms equals the required amount of beam swipes needed for the creation of a surface structure and is directly proportional to the total beam travel distance, which influences the beam travel speed (see Eq. 6).

(a)	(b)
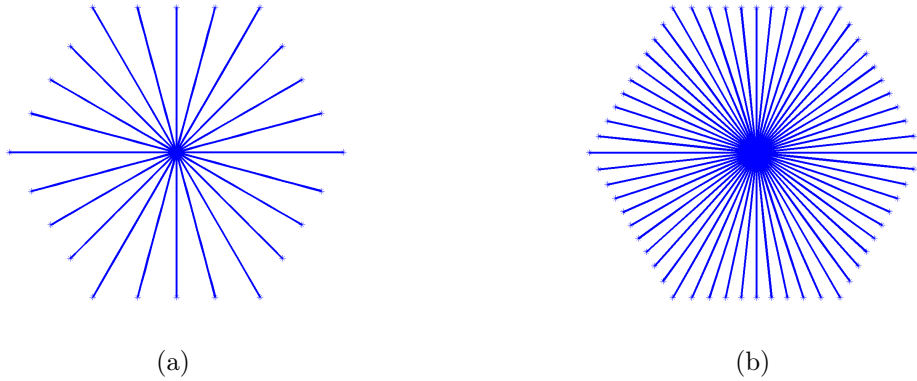
  Figure 20: Examples for: a) 24-arm and b) 60-arm deflection figure. [36]

- **Beam travel direction**

  Figure 21a depicts the beam travel direction from the centre to the perimeter of the figure which results in a protrusion at the centre of the figure ("pin-like structure"). For an inverse beam travel direction, from the perimeter to the centre, a movement of the material in opposite direction to the perimeter of the figure occurs, which results in an intrusion at the centre (see Fig. 21b ("wall-like structure")).

(a)	(b)
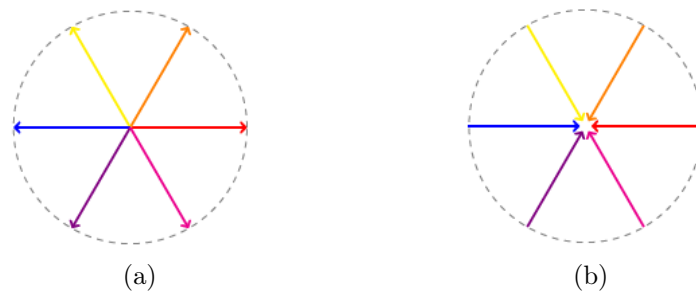
  Figure 21: Direction of beam travel in a) outward and b) inward direction. [36]

- **Figure arrays**

  Many different arrangements for structures with different geometry types can be realised. Figure 22 shows an example of a 2x4 array of hexagonal structures which can be used for the EBW surface structuring. The beam is deflected to travel the first arm of every single structure one after another before starting over at the position of the second arm of the first single structure in order to obtain a quasi simultaneous creation of multiple structures. The required creation sequence is depicted for the arms of a 2x4 hexagon array (Fig. 22).
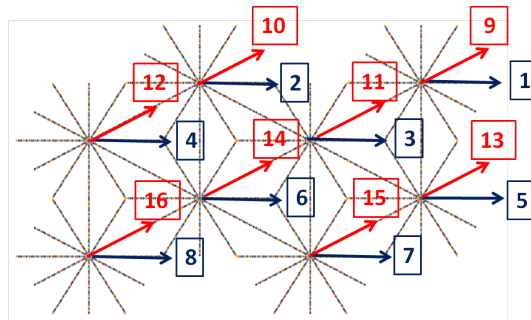
Figure 22: Quasi-simultaneous creation of 8 structures (2x4 array), with marked swipe sequence from arm 1 to arm 16.

3 Experimental procedure

The following section contains information regarding the physical and mechanical properties and the chemical composition of the investigated materials. Furthermore, a description of the surface structuring which was performed with the electron beam welding (EBW) machine is provided. Subsequently different analysis methods for topography characterisation and other performed investigations like metallography and micro hardness measurements are described. The chapter also goes into detail about the experiments executed in this thesis like cell experiments, heat treatments and dilatometry.

3.1 Materials

3.1.1 Titanium grade 2 (TiGr2)

Several structuring experiments were carried out on commercial pure TiGr2 (α-titanium alloy) which had been supplied in annealed condition [44]. Specimens of 15 x 15 mm^2 were cut by water jet from a sheet of 2 mm thickness. Table 1 shows the chemical composition limits for TiGr2 and the actual chemical composition [44]. Physical and mechanical properties of TiGr2 are listed in Table 2. Reference [44] corresponds to values for the delivered material).

3.1.2 Metastable β-titanium alloy (Ti15Mo)

The investigated material, near β-titanium alloy Ti15Mo, was delivered in β-annealed condition. The original round, wrought Ti15Mo bars (25 mm diam. x L) had been cut into plates (10 x 15 x 2 mm^3) produced by wirecutting.
In Table 3 chemical composition limits, specified in ASTM F 2066 standard [45] and the actual chemical composition are listed. Physical and mechanical properties of Ti15Mo in β-annealed condition are shown in Table 4.

Table 1: Composition limits and actual chemical composition (wt%) of TiGr2 according to producer [44].

Elements		Ti	Fe	C	N	O	H
Comp. limits	min	bal.	-	-	-	-	-
	max		0.30	0.08	0.03	0.25	0.015
Actual composition	min	bal.	0.06	0.02	0.01	0.12	0.002
	max		0.08				

Table 2: Physical and mechanical properties of TiGr2 as reported in literature.

Property		Value	Reference
Liquidus temperature		(1665 ± 5)°C	[46]
Density		4.50 g/cm^3	[47]
β-transus Temperature		913°C	[48]
Elastic modulus		(105-110) GPa	[15]
Thermal conductivity λ	at 20°C	22.6 W/(m K)	[47]
	at 400°C	19.3 W/(m K)	[47]
Tensile Strength		T: 472/482 MPa	[44]
		L: 488/495 MPa	
Yield Strength (0.2% offset)		T: 360/366 MPa	[44]
		L: 318/326 MPa	
Elongation		T: (30/30)%	[44]
		L: (29/28)%	
Reduction of Area		min 50%	[48]

Table 3: Composition limits and actual chemical composition (wt%) of Ti15Mo according to producer [49].

Elements		Ti	Mo	Fe	C	N	O	H
Composition limits	min	bal.	14.00	-	-	-	-	-
	max		16.00	0.10	0.10	0.05	0.20	0.015
Actual composition	min	bal.	15.6	0.04	0.001	0.012	0.15	0.002
	max		16.0	0.06		0.016		

Table 4: Physical and mechanical properties of Ti15Mo in β-annealed condition as reported in literature.

Property	Value	Reference
Melting range	(1.704-1.760)°C	[45]
Density	4.95 g/cm^3	[45]
β-transus temperature	(774 ± 14)°C	[45]
Modulus of elasticity	78 GPa (β-annealed condition)	[45]
Thermal conductivity λ at 31°C	0.03 cal/cm s °C (12.56 W/m K)	[50]
Tensile Strength	T: 785 MPa	[49]
	L: 775 MPa	
Yield Strength (0.2% offset)	T: 730 MPa	[49]
	L: 715 MPa	
Elongation	T: 26.5%	[49]
	L: 26.0%	
Reduction of Area	T: 74.5%	[49]
	L: 68.5%	

3.2 Surface modification

3.2.1 Electron beam (EB) technique

To produce surface structures on Ti15Mo and TiGr2 material an electron beam welding (EBW) machine type *EBG 45-150 K14* from *probeam* (Fig. 23) was used. The machine is equipped with several investigation and sensor systems such as a CCD camera for observations, an ELO-Tool for an electron-optical picturing of the processes and an X-ray sensor system. Furthermore, temperature measurements can be performed inside the EBW chamber. The machine can be controlled by a numerical control (NC) unit. Important technical specifications are shown in Table 5.

Table 5: Basic EBW machine data.

Electron Beam generator	
Max. Beam power	45 kW
Max. High voltage	150 kV^2
Beam current	(0.1-300) mA
Beam deflection speed	1°/μs
Chamber	
Volume	1.4 m^3
Table feed rate	(0.5-100) mm/s
Vacuum	
Evacuation time	< 6 min
EB generator	≤ 5 x 10^{-5} mbar
Chamber	≤ 5 x 10^{-3} mbar
^{2} for commonly used cathode type (pb350.7)	

Figure 23: Electron beam welding machine at IWS TU Graz.

The surface structuring was performed on TiGr2 boards as well as on Ti15Mo and TiGr2 plates. For all Ti15Mo and some TiGr2 plates a manual grinding had been performed in order to remove the layer produced by sandblast covering. This was achieved with a machine type: *Planopol-3* down to 4000 SiC-paper grit size. To prevent a shifting of the samples during the structuring process, an aluminium sample holder was used for plate fixation inside the vacuum chamber.

Creation of surface structures

To create surface structures with a desired geometry, a fast electromagnetic controlled deflection of the beam was used to guide the beam in a star like pattern across the surface. The deflection was controlled by a reading out of two dimensional coordinate point values located in a planar coordinate system of 65535 x 65535 points. In this thesis the coordinate points of selected deflection figures had been created using routines programmed with Matlab [36].
Figure 24 shows examples of figure arrays designed with the Matlab program.

(a)   (b)
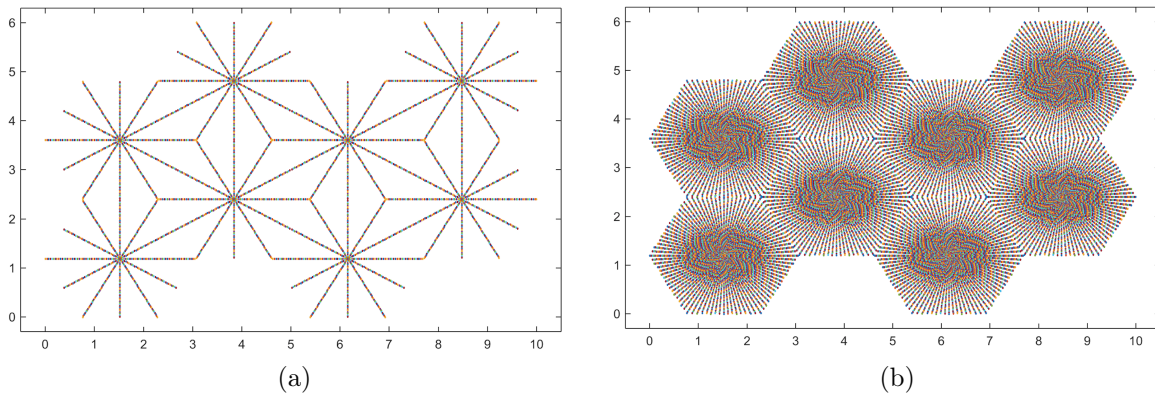
Figure 24: Layout of 2x4 figure arrays: a) 12 arm hexagons and b) 96 arm hexagons.

The following list contains parameter settings, used for the figure arrays:

- **Constant parameters used for all figure arrays created**
  - Polygon type of figure: hexagon
  - Single structure (hexagon) diameter: 4 mm
  - Constant distance between points
  - Figure array: 2x4

31

- **Varied parameters**

  - Beam guidance inwards (creating wall arrays) and outwards (creating pin arrays)
  - Single figure arm number: 12 and 96
  - Points: 4 032-39 984
  - Cycles (number of full cycles of the figure array): 0.5-10

To start the structuring process, the created figure deflection file was loaded into the EBW at a certain point storing position. Depending on the number of total coordinate points of the loaded figure file, a point storing position reserved for 1 000, or 10 000 points was chosen. Afterwards the values of structuring parameters were inserted into the NC program. In this context the understanding of correlations between machine parameters like READ RATE and WELDING TIME, specified in the NC program, and other important parameter like *cycles* and *beam travel speed* was important and is explained with the help of following examples:

We assume that a deflection file (programmed figure array) containing 40 000 coordinate points gets loaded into the EBW at a 10 000 point storing position and a value of 2 Hz is selected for the READ RATE in the NC program which means the following :
2 Hz $\hat{=}$ (2 x (point storing position)) Hz $\hat{=}$ (2 x 10 000) Hz, thus a readout of 20 000 coordinate points per second is executed by the program. In this case it takes 2 seconds to complete the whole deflection (40 000 figure array points) file. For this example a setting of 1 s for the WELDING TIME in the NC program, leads to an only half finished figure array ($\hat{=}$ 0.5 *cycles*) on the surface of the sample, because only 20 000 points (half of the 40 000 figure array points) are passed trough by the program. If a value of 4 s is selected for the WELDING TIME, the whole figure array is passed through 2 times (2 *cycles*). These connections result in the following Eq. 5:

$$cycles = \frac{read\ rate\ [points/s]\ .\ weld\ time\ [s]}{total\ number\ of\ figure\ array\ points} \tag{5}$$

Another important parameter is the *beam travel speed v*. It depends on the total travel distance of the beam which is determined by the programmed figure array and is directly dependent on the arm number (cf. Fig. 24). The following Eq. 6 is valid :

$$v\ [mm/s] = \frac{total\ travel\ distance\ [mm]\ .\ read\ rate\ [points/s]}{total\ number\ of\ figure\ array\ points} \tag{6}$$

The following list contains all used settings in the NC program of important machine

input parameters for the creation of surface structures.

- **Constant parameters used for all created figure arrays**

  - Focus setting: beam focused on the sample surface
  - Actual figure dimensions ($\hat{=}$ overall structure size created on the sample surface with a single structure diameter of 4 mm) : X amplitude = 13 mm, Y amplitude = 8.65 mm

- **Varied parameters**

  - Acceleration voltage : 80 kV and 150 kV
  - Beam current: (0.6-4.5) mA
  - Figure storing positions: (0-19) = reserved for 1 000-point figures, (20-39) = reserved for 10 000-point figures
  - Welding time: (0.5-4) s
  - File read rate: (1-20) Hz

  For the resulting parameters *cycles* and *beam travel speed v* the following values had been used:

  - Cycles : 0.25-20
  - v = (177.72-698.34) mm/s

3.2.2 Minimisation of weld pool width

The identification of optimal parameters for the structuring process to obtain a minimal width of the weld pool, was carried out by a series of structuring experiments on TiGr2 using 12 arm hexagon 2x4 pin arrays as pictured in Fig. 24a. An arm number of 12 for one hexagon had been chosen to prevent overlaps and facilitate the evaluation of the arm width.

After the execution of pretests, to identify parameters which exhibit an important influence on the weld pool width, the three factors: beam current (I_B), acceleration voltage (U_A) and beam travel speed (v) had been selected as input factors for a full factorial design of experiments (see Ref.[51]). The DoE schedule, and analysis, made with the help of the statistical software Minitab 16, was used to limit the amount of required experiments and obtain information about the influence of selected parameters on the arm width (output parameter). For more detailed information about DoE and the Minitab 16 program see Ref.[51] and Ref.[52] respectively.
After the selection of high and low level values for v and U_A, whereby the possible level choice for the latter was constrained by the minimum and maximum voltage limit of the used cathode, the possible levels for I_B had to be identified. To prevent a huge overlapping

of the arms, which would have hampered the measurement, the high U_A level (150 kV) was chosen to determine the upper level for I_B. The low level of U_A (80 kV) was used for determination of the low I_B level whereby the minimal necessary power for creation of a weld pool was the limiting factor.

Subsequently 8 single experiments according to a full factorial design including 3 factors at two levels ($2^3 = 8$) were performed. The constant parameters and variable factors incl. selected levels are listed below:

- **Constant parameters:**

  - Cycle: 1
  - Points : 4032
  - Arm number: 12

- **Variable factors:**

  - I_B: 1.2 and 3 mA
  - U_A: 80 and 150 kV
  - v : 177.72 and 355.44 mm/s

Eventually an analysis of the results regarding significance of the factors and identification of possible interactions was carried out with software support.

The parameter settings, used for TiGr2 were also used for subsequently performed experiments on Ti15Mo. This test series was carried out in order to ensure that the found relationships for TiGr2 are also valid for Ti15Mo. By comparing the results for the weld pool width for both materials the influence of the alloy type was investigated.

Subsequently the optimal parameter settings for I_B, U_A and v which were determined by the full factorial design of experiments on TiGr2, were used for the creation of 96 arm figure arrays on Ti15Mo to investigate the influence of the minimal weld pool width on the roughness values of the sample surface (see 3.3).

3.3   Characterisation of topography

Stereomicroscopy, light optical microscopy (LOM) and scanning electron microscopy (SEM) had been used to analyse the produced surface structures on Ti15Mo and TiGr2. Furthermore, roughness measurements of selected surface structures on Ti15Mo were performed by *Alicona Infinite Focus Microscope (IFM 2.0)*. Information about the overlapping process of the single weld pools and the formation of the whole figure had been attained and the influence of different structuring parameters (machine and figure) on the produced surface structures was studied.

3.3.1 Stereo microscopy

A macroscopic analysis of all surface modifications performed on Ti15Mo and TiGr2 samples was carried out by a *SteREO Discovery.V20 (Zeiss)* stereo microscope. A P*lanApoS 0,63x FWD81mm* objective was used for overview and detailed pictures of the created pin- and wall-arrays. The shape of the created structures was documented and investigations regarding reproducibility and appearance of macroscopic inhomogeneities or cracks had been executed. Figure 25 shows examples of created pin array structures.
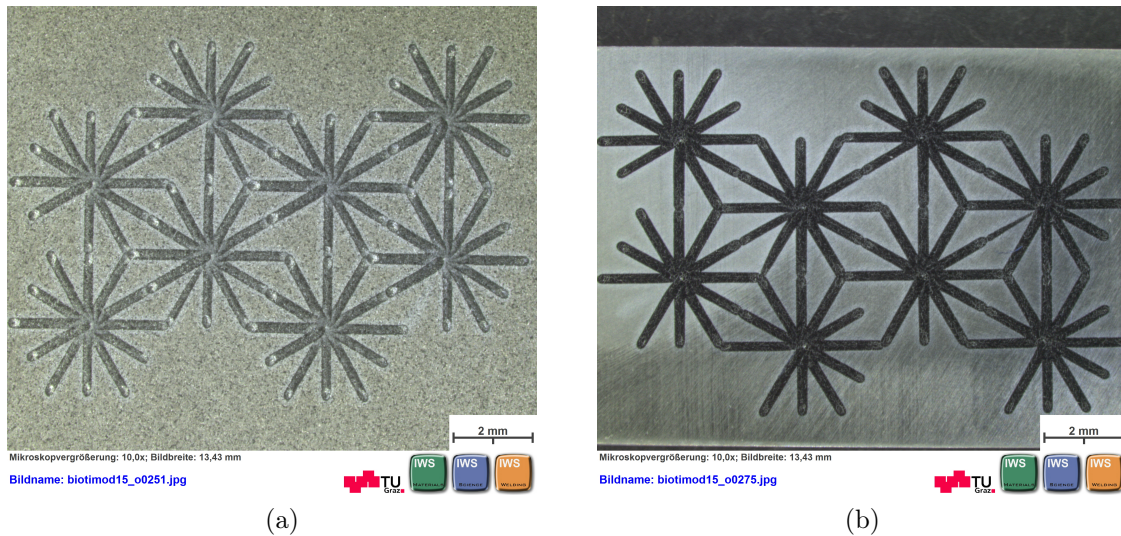
Figure 25: Examples of pin-arrays on a) TiGr2 and b) Ti15Mo.

3.3.2 Light optical microscopy (LOM)

For a more detailed investigation of the influence of structure parameter on the width of the weld pools created, a picture documentation of created pin arrays was carried out by a light optical microscope (*Zeiss- Axio Observer.Z1m*). To find the optimum set of parameters for the creation of a minimal width, monochrome images had been taken with a magnification of 25 x and bright field contrast. Subsequently an analysis of the "armwidth" of the created structures had been carried out using the Zeiss software *Axio Vision* (Release 4.7.1). To get reproducible results, the measurements were performed always at a fixed distance (1.6 mm) from the centre of a selected hexagon (shown in Fig. 26). After 8 measurements of arms located opposite to each other had been carried out, average and standard deviation were determined.
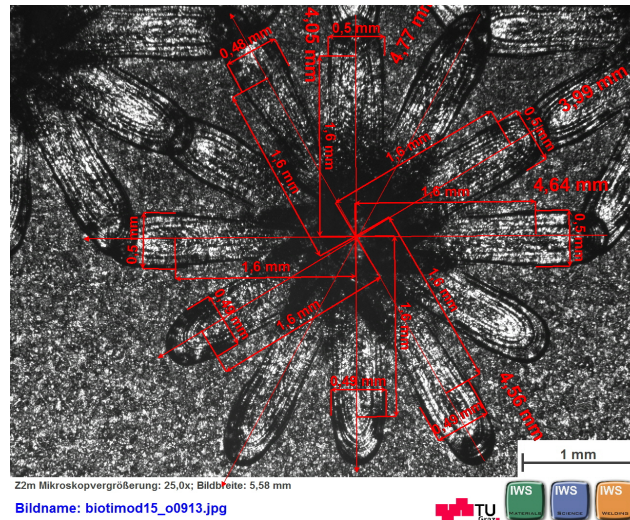
Figure 26: Image of 12 arm pin array incl. measurements of arm width.

3.3.3 Scanning electron microscopy (SEM)

The modified surfaces had been analysed by a scanning electron microscope type: *LEO 1450VP (Zeiss)*. Detailed information about the topography and roughness of pin and wall structures had been obtained using the signal of the secondary electrons (SE) for imaging. Investigation of the structures regarding reproducibility and the existence of cracks or pores in the microscopic scale was also carried out in SE mode.

3.3.4 Roughness measurements

3.3.4.1 3D profile measurement

3D profiles and roughness measurements of structured and unstructured Ti15Mo plate surfaces were done using an *Alicona Infinite Focus Microscope (IFM 2.0)*. The focus variation technique, provided by the microscope, allows the recording of 3D profiles. The sample is illuminated by white light which is reflected back by the surface and the picture is projected on a digital sensor. Figure 27a shows the optical path. Depending on the objective lens used different lateral and vertical resolutions can be realised. During the modulation of the distance between the sample and the objective a continuously recording of pictures takes place and because of the limited depth of focus of the system, for every height position z, different regions of the sample appear focused or unfocused depending on the 3D structure of the surface. For every coordinate point that appears focused, the correct height value z is identified (see Fig. 27b). Thereby a complete 3D representation (picture) of the surface can be created.
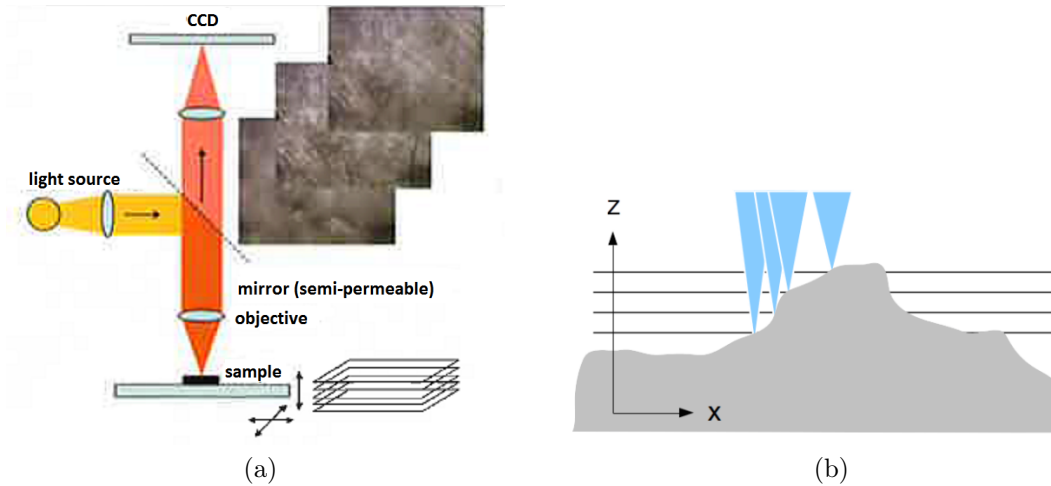
Figure 27: a) Set-up and optical path of an Alicona IFM G3, adapted from Ref.[53] and b) Focus variation principle.

Due to the expected roughness range of the structured Ti15Mo samples, an objective lens with 10 fold magnification was used for the recording of the 3D profiles. A vertical resolution of 100 nm and a lateral resolution of 3 µm had been chosen which produced recording result of a good quality. Table 6 shows the selected values for illumination, contrast and other selectable parameters for different investigated 96 arm hexagon figure arrays (see Fig. 24b) and one unstructured Ti15Mo sample.

Table 6: Parameters for 3D profile recording.

	wall/pin array I ((150 kV, 2 mA, 698.34 mm/s)see 3.4) /unstructured sample	wall array II ((opt. parameter: 80 kV, 1.2 mA, 349.03 mm/s) see 3.2.2)
Illumination	140 µs	130 µs
Contrast	0.5	0.51
Light	0.27	0.30
Ring light	1	no
Polarisation filter	no	no

After the recording process, different types of analysis of the 3D datasets, e.g., profile, area, or volume analysis are possible which are carried out by the software *Alicona IFM 2.0* (IFMeasureSuit).

A gold-palladium sputter process was used to cover the Ti15Mo surface due to the high reflectivity of the alloy, which hindered the recording of the 3D data set of the original surface. Coordinate points with very high light reflection appeared as black dots in the

picture. They could not be reconstructed because the height determination was not possible by the program. A sputter layer of about 70 nm led to good 3D data sets with high validation for the unstructured sample and wall/pin arrays I. The sputtering process was performed by a sputter machine type: *BALZERS Super Cool SCD 050*. The machine is equipped with a gold/palladium target with a rotary vane pump, in argon atmosphere. A working distance of approximately 50 mm and a working pressure of approximately 5x10-2 mbar with a current of 60 mA and exposure time of 154 sec was used. Because of the very high reflectivity of the wall array II sample, the sputter process was repeated 2 times which led to a gold/palladium layer of about 200 nm.

Profile analysis

A 3D surface profile can contain different frequency components. They can be separated into high frequency components (roughness) and low frequency components (waviness). Certain frequency components can be extracted by implementation of a filter. A high-pass filter extracts a roughness profile whereas a low-pass filter extracts a waviness profile (Fig. 28).
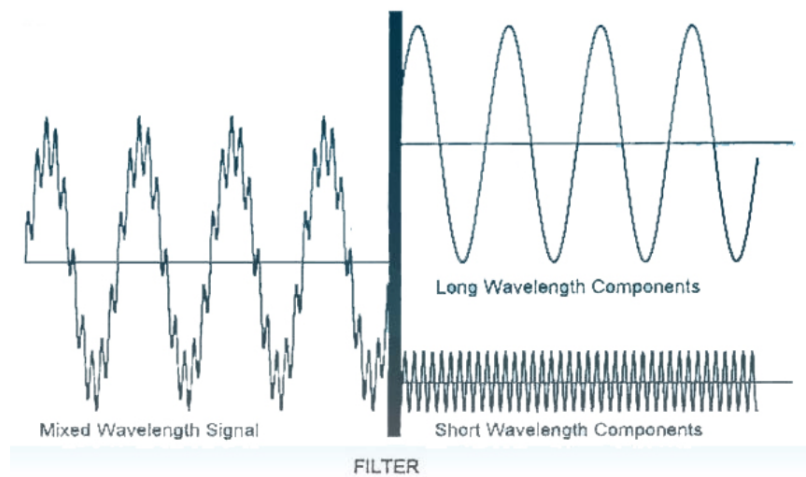
Figure 28: Display of filtering process. [54]

The threshold value for elimination or extraction of frequency components is the cutoff frequency λ_c of the utilised high-pass filter. The amplitude of a function with this frequency, is damped by 50% through applying the filter. To receive comparable results, the value of the cutoff frequency has to be the same in different measurements. For aperiodic profiles, the value for λ_c has to be chosen according to the *Ra* (arithmetic root mean square) roughness value (Eq. 7) expected for the surface. It represents the arithmetic mean of the absolute values of the roughness profile within the single section of measurement l_r and displays the average deviation of the profile from the midline (Fig. 29.).

$$R_a = \frac{1}{l_r} \int_0^{l_r} |z(x)| dx \tag{7}$$
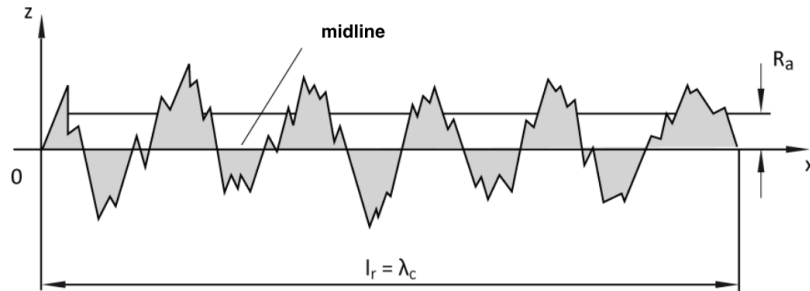
Figure 29: Arithmetic root mean square R_a, adapted from Ref.[55].

For periodic profiles, the choice of the right value for λ_c depends on the middle grove width R_{sm} (Eq. 8) see Fig. 30.
It displays the arithmetic mean of the widths of the roughness profile elements (profile uprising with neighbouring cavity) within a single section of measurement l_n.

$$R_{sm} = \frac{1}{n} \sum_{i=1}^{n} S_{mi} \tag{8}$$
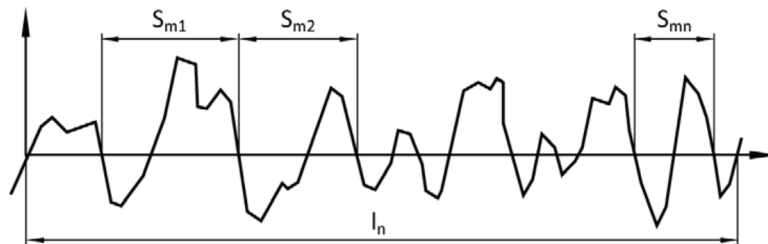
Figure 30: Middle grove width R_{sm}. [55]

This selection of a certain value for λ_c also determines the values for the *total measuring length* = (5 x λ_c) and the *key track* (6 x λ_c) according to DIN EN ISO 4288:1998 and DIN EN ISO 3274:1998 [55, 56].

Figure 31 shows 3D images of selected pin array I and wall array I-hexagons with marked scanning paths. For all investigated structures, 3 R_a roughness measurements were performed in regions where differences in roughness values had been expected. The scanning paths were set at 3 defined positions (red lines in Fig. 31) at certain distances from the centre (blue line in Fig. 31).

(a)   (b)
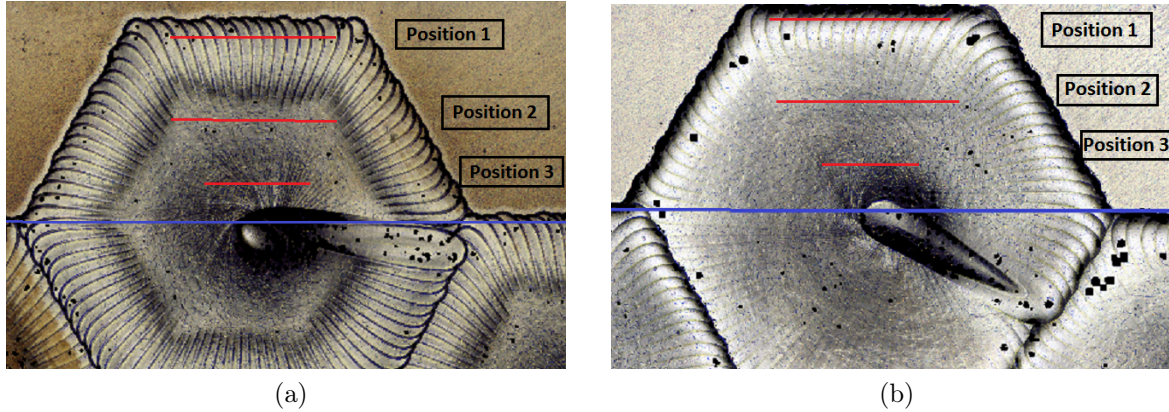
Figure 31: Positions of the measured profile lengths: a) Pin array I and b) Wall array I-hexagon.

The following list includes the 3 positions (measured distance between profile path and midline) with the measured profile lengths:

- Position 1: 1600 μm, profile length: (1504.6 ± 4.8) μm

- Position 2: 900 μm, profile length: (1504.6 ± 4.8) μm

- Position 3: 300 μm, profile length: (800.16 ± 3.4) μm

For position 1 and 2, the same profile length was used for the profile path. A smaller profile length was chosen for position 3, to prevent the influence of neighbouring regions with higher roughness values. The resulting values were generated by average and standard deviation determination because the profile length was not always the same value.
Because of the small size of the hexagons (diameter = 4 mm), the total measuring and key track length, required for an ISO conform determination of λ_c, could not be realised. An adjustment of the value for λ_c was performed instead as long as the shape of the surface was visible in the roughness profile [54]. This approach is explained with the help of following roughness profiles (Fig. 32 and Fig. 33):
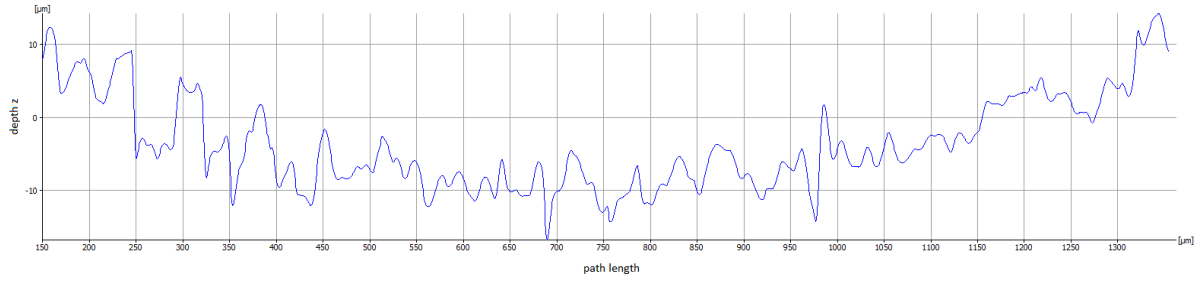
Figure 32: Roughness profile of wall array hexagon at position 2 obtained for $\lambda_c = 2500$ μm.
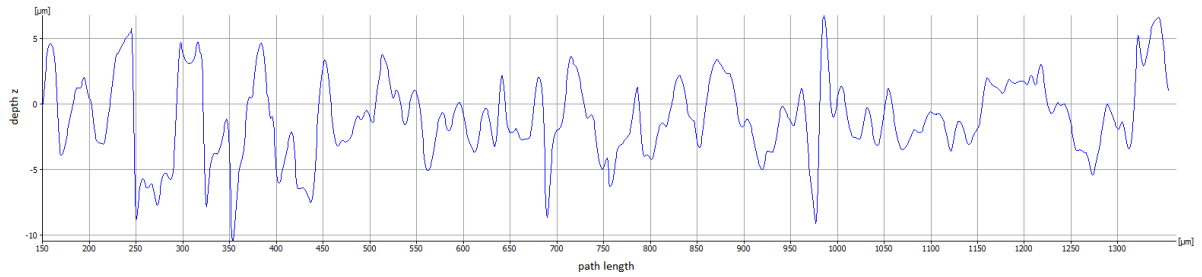
Figure 33: Roughness profile of wall array hexagon at position 2 obtained for $\lambda_c = 800$ μm.

For measurements at position 2 inside the wall array hexagon, a selection of $\lambda_c = 2500$ μm was the right choice to be ISO conform, for a R_a value between 2 and 10 μm and a R_{sm} value between 0.4 and 1.3 mm. However, this λ_c value produced a roughness profile with evident surface shape (see Fig. 32) and led to incorrect results for the roughness values. A choice of $\lambda_c = 800$ μm generated a flat profile, displayed in Fig. 33. The shape of the surface was removed and a reasonable value for the roughness was obtained.

At first sight, the surface, especially the edge of the hexagon, seemed to be periodic (Fig. 31). However, roughness measurements at positions between the edge and the centre of the hexagon revealed profiles similar to the one displayed in Fig. 32. Therefore, to make a comparison of roughness values possible for the whole hexagon, R_a (instead of R_{sm}) was selected for roughness characterisation. Besides the utilisation of R_a enabled a comparison with the aperiodic surface of an unstructured Ti15Mo plate.

To determine the height of the pin and the depth of the pit with respect to the unstructured sample surface, primary profiles (not filtered) were made near the centre of the hexagons, using the unstructured region as reference line. Figure 34a shows one example of a selected path on a wall array-hexagon. The obtained primary profile used for measuring the pit depth of the wall array-hexagon is displayed in Fig. 34b. Results were obtained by an average determination of 5 measured values including standard deviation.

41
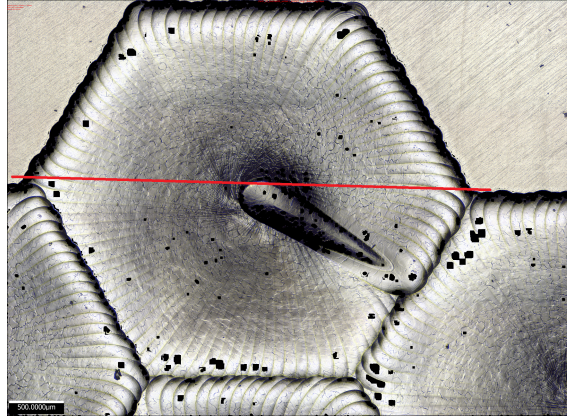
(a)
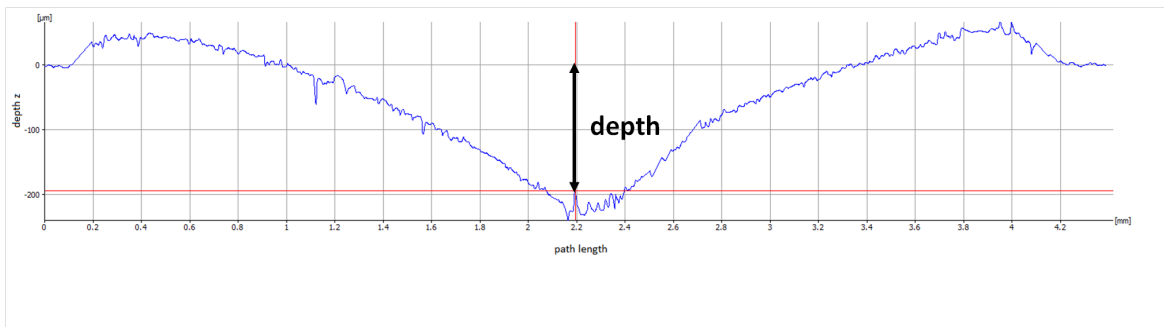
(b)

Figure 34: a) Profile path in the centre of a wall-hexagon, b) Resulting primary profile.

Area analysis

A certain hexagon of the pin or wall array was selected for surface texture measurements. The received data set was analysed regarding real surface, projected surface, and the surface enlargement. Surface roughness measurements were carried out, using the arithmetic root mean square surface roughness value S_a (3D equivalent of the 2D roughness parameter R_a). Again a manual adjustment of the cut off frequency λ_c was necessary to remove the shape of the surface [54]. Furthermore, surface roughness measurements of unstructured Ti15Mo plates, ground up to 4000 SiC paper, were executed for comparison with the structured ones. Three measurements were performed at different positions of the 3D data set of the plate, using S_a as characteristic roughness value.

3.4 Cell experiments

Cell experiments and the subsequent analysis of the results were performed to investigate the influence of surface modifications on the cell growth and morphology. The execution of the cell experiments was carried out at the medical university of Graz. The cultivation of cells was performed on structured (wall array I) Ti15Mo plates and on ground (4000 SiC paper) plates which were used as comparative samples. The following list contains

the chosen figure and machine parameters used for the surface modification of Ti15Mo for cell experiments:

- Polygon type: hexagonal inward (wall array)

- Arm number: 96

- Current: 2 mA

- Voltage: 150 kV

- Frequency: 2 Hz

- Welding time: 2 s

and the following resulting parameters:

- Cycle: 1

- Velocity: 698.34 mm/s

The experiments had been performed with the cell line MC3T3-E1 (Osteoblasts) and a density of 10 000 cells/cm^2. Table 7 gives an overview of the used Ti15Mo surfaces and corresponding cultivation times.

Table 7: Overview of executed cell experiments.

Ti15Mo surface	Cultivation time hs
structured (wall array)	6, 24, 48
ground (4000 SiC paper)	6

To investigate the influence of surface structures and different roughness values on the cell behaviour, analyses of the surfaces after cultivation were carried out by SEM (SE and BSE images). To avoid surface charging during the the observation with SEM a coating of the samples with gold palladium was necessary, which had been performed with the BALZERS Super Cool SCD 050 sputter machine. To obtain a sputter layer with a thickness between 3 and 10 nm a sputter time of 70 s and a current of 20 mA were used. BSE overview images were made to get information about a possible arising *orientation* of the cells and to characterise the cell *distribution* on the surface. A detailed analysis of the cell *morphology* was carried out by SE mode SEM images with higher magnification (500x).

3.5 Heat treatments and dilatometrie

To investigate phase transformations and changes in the microstructure and hardness, heat treatments of structured Ti15Mo samples and Ti15Mo material in as-delivered condition were carried out in a dilatometer, in order to reduce the oxidation of the sample surface.

For the structured Ti15Mo samples, dilatometer measurements were performed during the heat treatments to measure the change in length with temperature. Heat treatments as well as dilatometry experiments were performed in a *BÄHR Thermoanalyse DIL805 dilatometer*.

3.5.1 Heat treatments of samples in as-delivered condition

Heat treatments of the as-delivered samples were performed to analyse the influence of different cooling rates from above β-transus on the microstructure, especially the starting point of α-phase formation and hardness of the material. Ti15Mo pieces with a thickness between 4 and 5 mm and a height of 10 mm were used. Table 8 shows the utilised values of heat treatment parameters.

Table 8: Listing of heat treatment parameters.

Heating rate	Holding temperature	Holding time	Cooling/Cooling rate	Atmosphere
300 K/min	800 °C	5 min	Gas-quenched	Vacuum/He atmosphere
			100K/min	
			50 K/min	
			20 K/min	Vacuum
			5 K/min	Vacuum

The measurement of the sample temperature was carried out with a thermocouple type S (Pt-PtRh). The thermocouple had been fixed at the middle of the samples by spot welding.

Furthermore, one Ti15Mo sample was heat treated at 850°C for 20 min. and water quenched, to compare the obtained microstructure with the as-delivered condition.

3.5.2 Heat treatments of structured samples

Ti15Mo plates with a structured surface (pin array), were investigated regarding changes in the microstructure and hardness due to application of 2 different heating rates and ageing temperatures at 550 and 600°C. A thermocouple type K (NiCr-Ni) was used for measuring the temperature and experiments were performed in an Argon 4.6 atmosphere. Parameters used for heat treatments and dilatometer measurements are shown in Table 9.

Table 9: Parameter for heat treatments and dilatometer measurements.

Heating Rate	Ageing Temp.	Holding Time	Cooling
300 K/min	550°C	24 h	
	600°C		
			Gas quenching
5 K/min	550°C	24 h	
	600°C		

3.6 Metallography and microstructure analysis

To investigate changes in the microstructure and grain size of Ti15Mo due to structuring processes and heat treatments, LOM and SEM were used after the sample preparation. Besides a characterisation of the microstructure of the material in as-delivered condition and analysis of the structured samples concerning inhomogeneities and internal defects had been carried out. To get information about the element composition at selected regions EDX analysis was used.

3.6.1 Sample preparation

The determination of the separate preparation steps was a challenging process because the material tends to form a strong deformation and/or smear layer during the preparation [15, 57]. The deformation of the material can happen during the coarse grinding steps. If this layer can not be removed during polishing, the surface looks smeared and wavy after the final polishing step.
Figure 35 shows the micrograph after the last polishing step with OPS for 27 min. (has small etching effect).

(a)   (b)
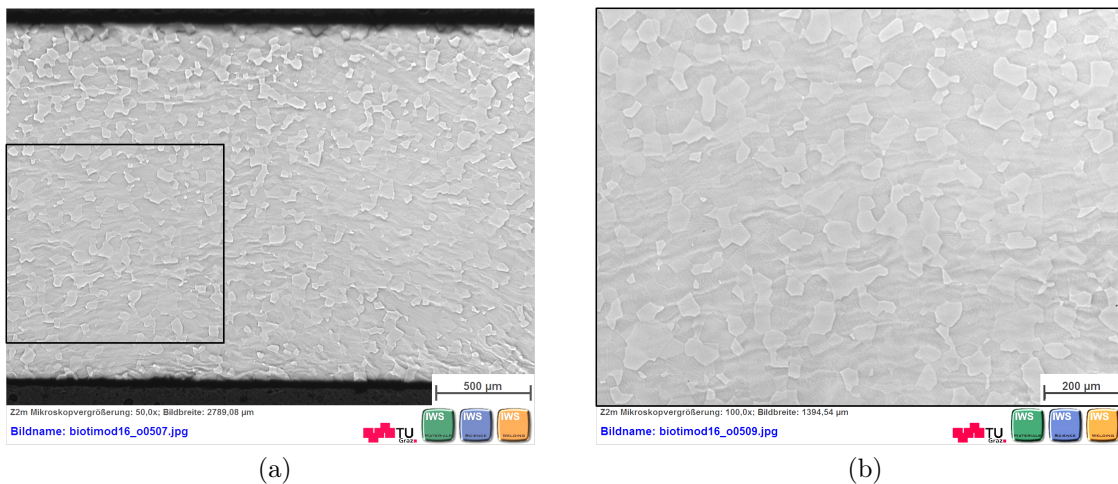
Figure 35: LOM images of Ti15Mo base material after polishing with OPS for 27 min.: a) Overview and b) Detailed view of the wavelike surface.

The surface seems to be covered by a "veil" which made the surface look wavy during LOM examination. A subsequent etching of the surface increased this effect.
After several trials, the preparation of the samples could not be improved.

Samples were embedded in DuroFast, an epoxy hot mounting resin, using the machine *Struers CitoPress-10* with fixed thermo and time settings for hot mounting (according to *Struers*). Subsequently the grinding of the specimen was performed by application of a machine type: *Struers Tegramin-30*. Silicon carbide abrasive papers with various grit sizes (grit: 320, 500, 800, 1200, 4000) and forces between 10 and 15 N per sample were applied. After each grinding step, the samples and sample holder were cleaned with water to prevent scratching of the sample surface in the following step because of potentially remaining particles. The various cloths and suspensions used for polishing the samples are listed in Table 10. The applied forces and polishing times are shown as well.

Table 10: Polishing steps.

	Cloth	Grit size [μm]	Suspension	Lubricant	Force per sample [N]	Time [min]
[3]	MD Mol	3	Nap Dia Duo-2	DP-Lubricant Blue	15	15
	MD Nap	1	Nap Dia Duo-2	DP-Lubricant Blue	15-20	15-(30)[4]
	MD Chem[5]	-	OP-S	-	10-15	20-30

[3] Step only used for preparation of heat treated samples with cooling rates of 20 and 5 K/min
[4] SEM preparation of heat treated pin array-structured samples
[5] Performed in counter rotation in contrast to all other grinding and polishing steps

Between each polishing step a rinsing of the samples was performed. The mentioned OPS suspension in the last step stands for a 1:5 blend of OPS *Nondry* and distilled water.
Subsequently, to remove OPS from the samples and the used *MD Chem* cloth, an additional "polishing" step using a force of 10 N per specimen and water lubrication was performed for 3 minutes. Eventually a cleaning of the samples in an ultrasonic bath type: *Bandelin Sonorex TK52* was carried out for 5 minutes.
To complete the preparation for investigations with SEM and EDX, the selected specimens were cleaned with alcohol and dried. For microstructure analysis with LOM a micro-etching in Kroll solution (*85 ml distilled H_2O, 10 ml nitric acid, 5 ml hydrofluoric acid*) had to be carried out for some of the polished samples. Depending on the sample condition (base material in as-delivered condition, heat treatment, structure), several etching times were applied. Long immerse times between 20 and 27 s were chosen for the base material. The time range of 5 to 27 s was applied to the structured and heat treated samples. Finally a cleaning with alcohol and drying of the samples was performed.
It should be mentioned that an application of chemical or electrolytical polishing tech-

niques, could prevent the formation of a deformation layer for this material [58].

3.6.2 Light optical microscopy (LOM)

To get detailed information about the microstructure of the samples, light optical microscopy was carried out after the sample preparation using the same microscope and settings as mentioned in 3.3.2. Images with various magnifications were taken to analyse the Ti15Mo base material (as-delivered condition) as well as structured Ti15Mo plates regarding inhomogeneities, pores or inclusions. Furthermore, analysis of changes in microstructure and grain size due to the structuring process or heat treatments were carried out by investigations in the different regions as *structure* (molten region), *heat affected zone* and *base material*. To obtain a better understanding of the overlapping process of the individual melting baths and the formation of solidification lines a detailed analysis of the molten region at the surface of structured samples was performed.

3.6.3 Scanning electron microscopy (SEM) and energy-dispersive X-ray spectroscopy (EDX)

Detailed microstructure analysis of selected samples was performed using SEM. To avoid charge processes during the investigations, a conductive connection between sample and sample holder was created using a copper strip. SEM micrographs of heat-treated base material and structured samples were taken in BSE and SE mode using accelerating voltages between 10 and 20 kV and a working distances between 7 and 9 mm.

EDX (energy dispersive X-ray) analysis was carried out to get information about the element distribution and to obtain a better understanding of the solidification process during the structuring of the material and possible segregation effects. For these purpose, spot measurements and linescans had been performed in the structured surface region and in the base material of Ti15Mo samples using a spectrometer type: *BRUKER QUANTAX 4000* and a working distance of 10 mm.

3.7 Microhardness measurements

Vickers hardness measurements were carried out for Ti15Mo in as-delivered condition as well as for all heat treated Ti15Mo samples (structured plates and base material) using a microhardness tester *MHT-4*. All tests were performed using the following parameter values:

- Force (applied on the sample by a diamond indenter): 30 pond[6]

- Dwell time (for indenter) = 15 s

- Slope = 5 (5 pond per second)

---

[6]kilopond = outdated, not SI conform unit of force
1 kp $\hat{=}$ g$_N$(9.81 m/s^2) x 1 kg = 9.81 (kg m) /s^2 = 9.81 N
1 pond $\hat{=}$ 9.81 m/s^2 x 10^{-3}kg 0 0.00981 Newton

The square shaped holes created in the material by the pyramid shaped diamond intender with a square base, were analysed with the *MeF Axio Vision software.* A measurement of the diagonals of the stamps were carried out to obtain the HV0.030 values (see Fig. 36)
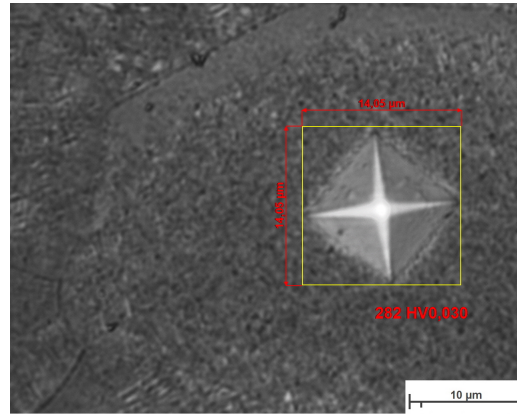
Figure 36: Evaluation of HV0.030 value by measuring the diagonal distance of indentation.

To obtain reliable values for the hardness, 7 measurements were performed at different positions on the sample (for heat treated samples near to the former thermoelement position). For the structured Ti15Mo samples, 7 measurements had to be carried out in the regions *structured zone* (SZ), *heat affected zone (HAZ)* and *base material (BM),* respectively. After the highest and lowest hardness values had been kicked out of the calculation, an average determination of the remaining values and an error analysis using the "Größtfehler" method were performed.

4 Results and Discussion

4.1 Characterisation of base material

4.1.1 Ti15Mo

Figure 37a shows the microstructure of Ti15Mo base material after the final OPS polishing step. The microstructure only consists of metastable β grains as assumed in section 3.1.2 for as-delivered condition. In Fig. 37b same microstructure was observed for a water quenched Ti15Mo sample after heat treatment above the β-transus temperature (850°C for 20 min.). No indication of α-phase could be found in both materials.
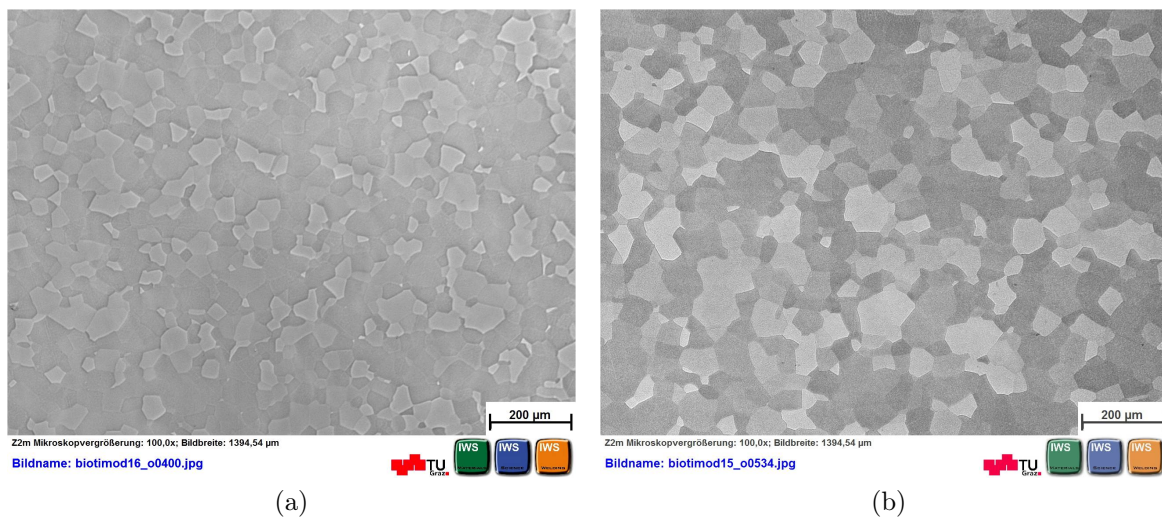
Figure 37: LOM images of a) Ti15Mo microstructure in as-delivered condition (after 27 min OPS polishing) and b) Heat treated Ti15Mo microstructure after 15 min OPS-polishing and etching for 7 sec..

4.2 Surface modification of Ti15Mo and TiGr2-plates

4.2.1 Optimisation of weld pool width on TiGr2 and Ti15Mo

To evaluate the influence of the process parameters on the weld pool, a singular cycle was chosen for the figure creation on TiGr2. According to Eq. 3.2.1 the welding time was set to 1 s. Table 11 shows the DoE schedule for a full factorial design of experiments created with the statistical software Minitab 16. The levels for the three factors and the results for the weld pool width measurements (output parameter) including standard deviations are also presented.

Table 11: DoE schedule for selected factors and output parameter for the figure (weld pool width) created on TiGr2.

Exp.	Factors			Output Parameter
No.	U_A [kV]	I_B [mA]	v [mm/s]	*weld pool width* [mm]
1	80	1.2	177.72	0.283±0.023
2	150	1.2	177.72	0.445±0.013
3	80	3	177.72	0.511±0.022
4	150	3	177.72	0.676±0.052
5	**80**	**1.2**	**355.44**	**0.159±0.006**
6	150	1.2	355.44	0.313±0.031
7	80	3	355.44	0.419±0.008
8	150	3	355.44	0.494±0.007

The minimal weld pool width of (0.159 ± 0.006) mm were obtained for 80 kV and 1.2 mA, with a beam travel speed of 355.44 mm/s.

An analysis of the results was done graphically using plots of Pareto, Main effect, and Interactions between the factors. The results are depicted in Fig. 38. The significant factors A, B and C, were identified as acceleration voltage U_A, beam current I_B, and beam travel speed v respectively. The current (B) was the factor with the strongest influence (see Fig. 38a and Fig. 38b). The effect of the interactions between the factors (AC, ABC, AB and BC) on the target parameter (weld pool width) was very small (see Fig. 38a). The Main effect plot in Fig. 38b shows the reasonable change of the target parameter value during a modification of the significant factors. The width of the weld pool increases with decreasing values for beam travel speed and increasing current and voltage values. It can be correlated with the energy input per unit length *(EL)*:

$$EL[J/mm] = \frac{U[kV] \cdot I[mA]}{v[mm/s]}$$ (9)

The optimal parameter setting corresponds to an *EL* of 0.270 J/mm, which represents the minimal required value for the formation of a weld pool on TiGr2 for this parameter setting. The graphs in the Interaction plots (see Fig. 38c) are almost parallel which demonstrates that there is no strong interactions between the three significant factors I_B , U_A and v.
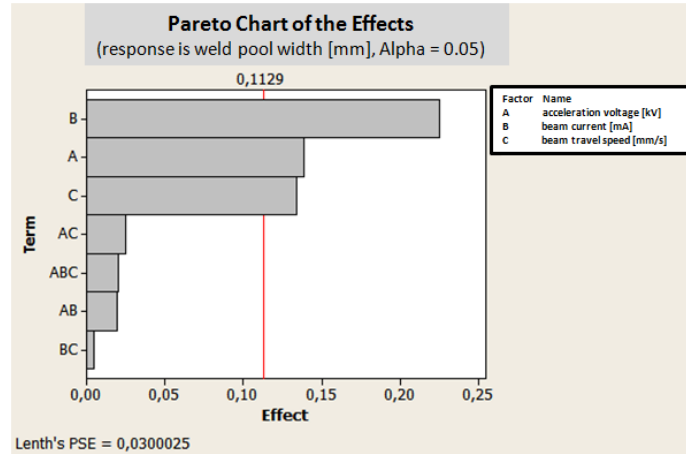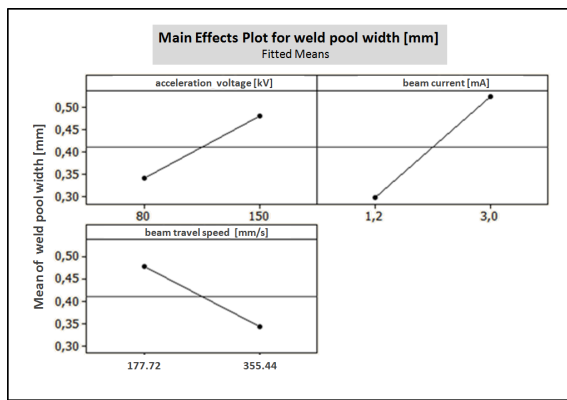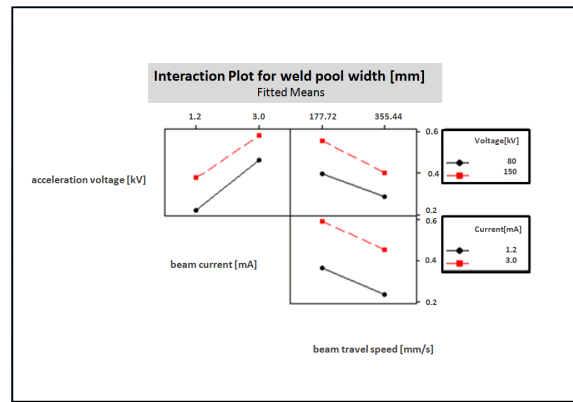
Figure 38: a) Pareto diagram of the effect of the factors and their interactions on the weld pool width, b) Main effect plot and c) Interaction plot for weld pool width.

The selection of the low level value for I_B (1.2 mA) in the full factorial design of experiments had been limited by the 80 kV level value of U_A, because a certain amount of power was necessary to melt the material. Because of identification of the current I_B as being the most important influencing factor, post-tests using the high levels for v and U_A while lowering the I_B values were executed for identification of a possible new minimum for a low I_B value.

Another reason for this investigation was the influence of U_A and I_B on the focal diameter d_0 of the beam, which represents an additional determining factor for the weld pool width. With increasing I_B or decreasing U_A an increase of the focal diameter can be assumed (see Fig. 15 and Ref.[38], p.40).

A minimum was found for $v = 355.44$ mm/s, $U_A = 150$ kV and $I_B = 0.8$ mA (corresponding to an EL of 0.337 J/mm). However, the value for the weld pool width was the same as for the first settings ($v = 355.44$ mm/s, $U_A = 80$ kV, $I_B = 1.2$ mA) and could therefore not be improved.

To investigate if the obtained relationships between I_B, U_A, v and the weld pool width were also valid for Ti15Mo, experiments using the 12 arm pin array figure were carried out on Ti15Mo and TiGr2 with the following parameters:

- 150 kV, 1.2 mA, 4 Hz, 1 s weldtime, $v = 177.72$ mm/s

- 80 kV, 1.2 mA, 4 Hz, 1 s weldtime, $v = 177.72$ mm/s

- 80 kV, 3 mA, 4 Hz, 1 s weldtime, $v = 177.72$ mm/s

- 80 kV, 1.2 mA, 8 Hz, 0.5 s weldtime, $v = 355.44$ mm/s

Figure 39 shows the relationship between the weld pool width and energy input per unit length (*EL*) for Ti15Mo and TiGr2.
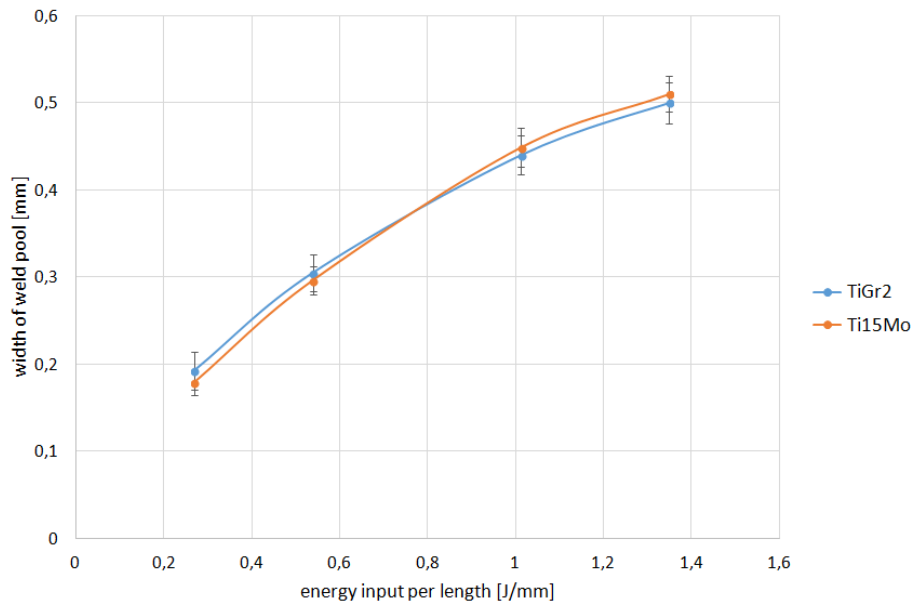
Figure 39: Width of weld pool vs. energy input per length for TiGr2 (blue) and Ti15Mo (orange).

The results for the weld pool widths, obtained for the two studied materials, were similar. For relatively "high" energy input per length TiGr2 shows a thinner width of the weld pool which is in accordance with the higher thermal conductivity of TiGr2 compared to Ti15Mo. However, for very low energy input a reversed effect is visible.

In order to fully understand the development of a weld pool with a certain width for different materials, factors like *specific heat capacity, heat of fusion* and the *dimensions*

of the specimens which influences the heat dissipation, must also be taken into account. Furthermore, because of the fact, that not all of the experiments were carried out at the same day, additional influencing factors like the applied vacuum, the working time of the used cathode and of course the not always perfect manual focus setting on the surface of the material have to be involved in the error analysis. For experiments with high energy input per length, this influence lies within the standard deviation and can be neglected. However, for experiments with low energy input per length, the difference between two measurements carried out on two different days, can be up to 17 %. Such a discrepancy relativises the reversed tendency of the influence of the two materials on the weld pool width in this region.

Nevertheless, because of the very small deviations of the weld pool width measurements for the two materials, the first optimal parameter settings, which were identified after the full factorial design of experiments (see Table 11) on TiGr2 were chosen for further structuring experiments, whereby the influence of the weld pool width on the roughness of created structures on Ti15Mo was investigated. It must be noted, that because of the utilisation of a 96 arm hexagon figure array in the further studies and the resulting total length of 1396 mm of the whole figure array, an exact setting of $v = 355.44$ mm/s was not possible. The experiments were performed with a beam travel speed of $\boldsymbol{v = 349.03}$ **mm/s** using a welding time of 4 s and a read rate of 1 Hz.

4.2.2 Topography and roughness analysis of Ti15Mo

Topography

Figure 40 shows Stereo microscopy images of pin and wall array-hexagons, created with optimal parameters (80 kV, 1.2 mA, 349.03 mm/s).

(a)   (b)
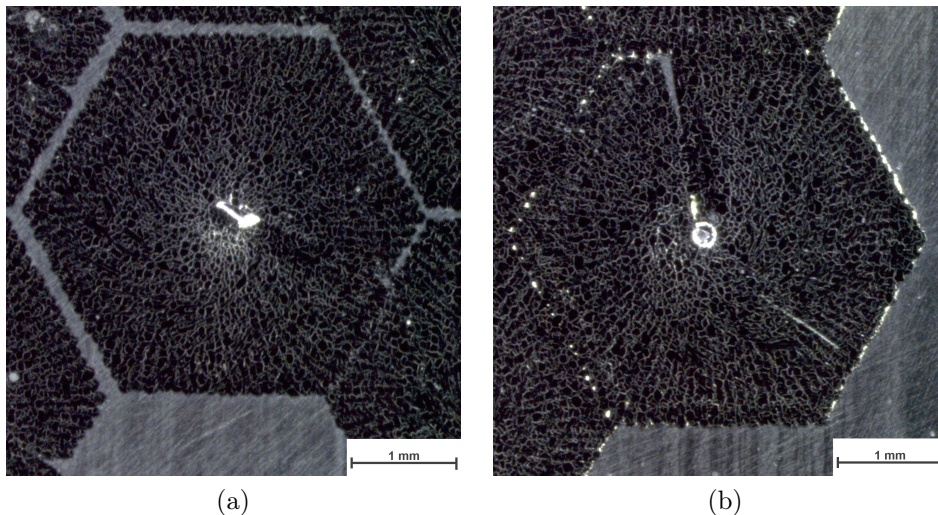
Figure 40: Stereo images of a) Wall array-hexagon and b) Pin array-hexagon produced with optimal parameters.

The surface texture of both figures appears to be smooth and homogenous. However, for these parameters, the edges of the wall-hexagons and for the pin-hexagons the centres of the figures are not molten. This effect can be explained by the starting point of the beam in these two figure arrays. For the wall array, the starting point of the electron beam and each weld pool is located at the edge of the hexagons and the beam in moving inwards. At the starting point, the power of the beam heats up the material, but is not high enough to melt it. Along the traveling way of the beam, the area is heated up, the material starts to melt and the weld pool is formed. After the creation of the first arm of hexagon 1, the beam moves to the next hexagon of the 2x4 array and the creation of the first arm for hexagon 2 starts. Once again, the material does not melt at the starting point at the edge of the hexagon. After traveling the first arm of every single hexagon, the beam starts over at the position of the second arm of hexagon 1 and so on (see Fig. 22). Such a beam movement results in a not melted area surrounding the edge of each hexagon.

In the case of the pin array, the beam starts in the centre of the hexagon and moves from inside to its edge, which results in a not melted region in the centre of each hexagon. Furthermore, a not molten first arm was visible for each pin array-hexagon. To prevent this effect an adjustment of I_B, U_A or v values has to be executed to obtain a higher EL. Figure 41 shows detailed views of wall and pin array hexagons, created with parameters: 150 kV, 2 mA, 698.34 mm/s, used for cell experiments.
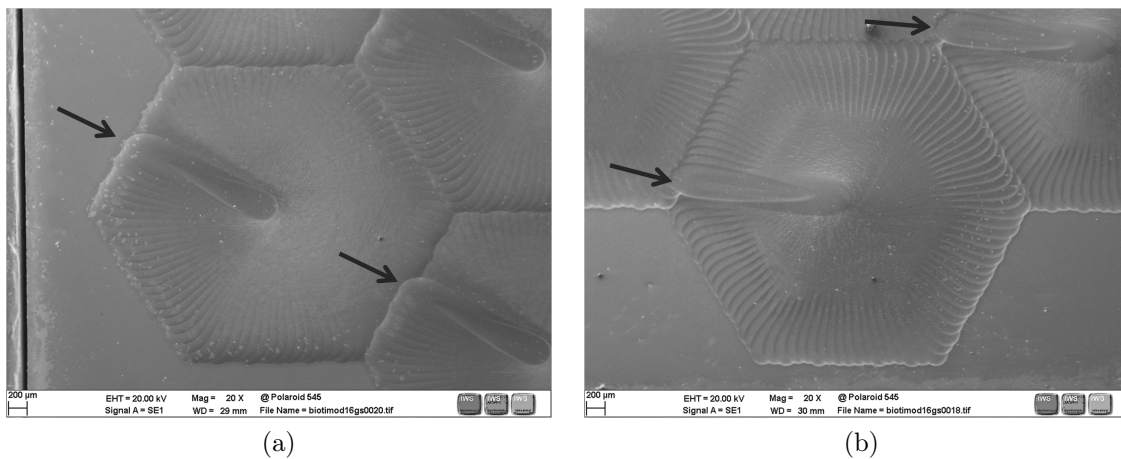
Figure 41: SE images of pin and wall array-hexagon, topography of a) wall array-hexagon and b) pin array-hexagon. Arrows identify the last arms created.

Areas with different levels of roughness are visible for both structures and it seems that the topography becomes more smooth in the centre of the hexagons, which could be explained by the strong arm overlap in this area. Overall, no defects are visible on the surface and the wall array-hexagon appears more smooth than the pin array-hexagon,

especially in the area at the edge of the hexagon. The final arm created in the hexagon (marked by arrows in Fig. 41) is denoted by a wide flat area.

Roughness measurements

Surface texture/ roughness measurements and profile roughness measurements were carried out for the following samples:

- wall array I (generated with parameters for cell experiments: 150 kV, 2 mA, 698.34 mm/s)

- pin array I (generated with parameters: 150 kV, 2 mA, 698.34 mm/s)

- wall array II (generated with optimal parameters: 80 kV, 1.2 mA, 349.03 mm/s)

After the finished recording of a 3D data set, the area of the investigated hexagon of the figure array was selected to perform **surface texture measurements**. Table 12 shows the measured values for the three investigated samples.

Table 12: Selected surface texture parameters.

Structure	Real surface [mm^2]	Projected surface [mm^2]	Surface enlargement [%]	S_a[µm] (λ_c= 800 µm)
pin array I	15.8	10.5	50.5	5.1
wall array I	13.2	9.8	34.7	4.5
wall array II	9.8	8.0	22.7	2.7

Pin array I showed the highest value for the surface enlargement and also the highest S_a (see Table 12). The values for the wall array I were higher compared to the values obtained for the wall array II. The lower energy input per unit length (EL) obtained for the structuring of the wall array II ($EL = 0.2750$ J/mm, compared to a value of $EL = 0.4296$ J/mm for wall and pin array I), resulted in a smaller width of the weld pool. This is the reason for the lower values for the surface enlargement and S_a.
Regarding the influence of the surface structure on the strength of adhesion between an implant and the surrounding tissue, a rougher, structured surface has to be preferred in comparison to a smooth ground surface. A high value for the surface enlargement, obtained from a higher roughness value, results in a larger area of contact to the tissue. This causes higher adhesions strengths compared to a smooth ground surface with smaller area of contact [15].

For **surface roughness measurements** of unstructured Ti15Mo plates, ground up to 4000 SiC paper, a value of $\lambda_c = 800$ µm was chosen for the cut off frequency. The mean value for S_a was (776 ± 21) nm.

The investigation of the structures regarding pin height and wall depth was carried out by **profile roughness measurements** at positions close to the centre of the examined hexagon (Fig. 34b). For all measurements the unstructured part of the surface functioned as reference zero point. The average value for each studied figure was:

- pin array I figure: pin height = (240.7 ± 5.2) μm

- wall array I figure: pit depth = (227 ± 3.8) μm

- wall array II figure: pit depth = (55.2 ± 2.2) μm

Table 13 shows R_a roughness values obtained for different investigated structures, for different scanning path positions and corresponding λ_c values used for the roughness filtering. The error measurement was considered to be around 7.8 %.

Table 13: Roughness values for pin and wall arrays at different positions in the hexagon.

	λ_c [μm]	Pin I	Wall I	Wall II
		R_a [μm]	R_a [μm]	R_a [μm]
Position 1 (1600 μm)	2500	5.4 ± 0.4	3.3 ± 0.3	2.8 ± 0.2
Position 2 (900 μm)	800	2.6 ± 0.2	2.6 ± 0.2	2.4 ± 0.2
Position 3 (300 μm)	250	1.7 ± 0.1	1.7 ± 0.1	1.5 ± 0.1

It can be seen, that the depth for the wall array II-hexagon, generated with optimal parameters for a minimal weld pool width, was much smaller compared to the value for the wall and pin array I-hexagon. This effect was also caused by the lower EL used for the structuring of the wall array II hexagon. The consequence is a smaller weld pool width. Thus, less molten material could be shifted during the structuring process.

At position 1, where the overlap of the arms is relatively small, the pin array I-hexagon showed the highest roughness values. The roughness decreased when the centre is approached. This tendency correlates with the results of the topography analysis, whereby the region with high arm overlap in the centre of the pin array-hexagon appeared more smooth than the edge region in the SE images (see Fig. 41b). The same roughness tendency was found for the wall II and wall array I-hexagon, which also matches very well with the topography analysis findings (Fig. 41 and Fig. 40a). Furthermore, the coarser appearance of the edge of the pin array-hexagon compared to the wall array-hexagon correlates with the roughness values at position 1 for the pin I and wall array I-hexagon. The wall array figure with optimised parameters showed the lowest values of roughness in each measured position.

4.2.3 Cell experiments

Figure 42 shows a selection of SEM images (BSE mode) of cell experiments after different cultivation times on different Ti15Mo surfaces. Cell experiments on ground surface (4000 SiC paper) (Fig. 42a) and wall array structured surface (Fig. 42b) after a cultivation time of 6 hs and experiments on structured wall array samples after cultivation times of 24 hs (Fig. 42c) and 48 hs (Fig. 42d) are compared. The investigated regions within the wall array-hexagons are marked in schematic hexagon representations.
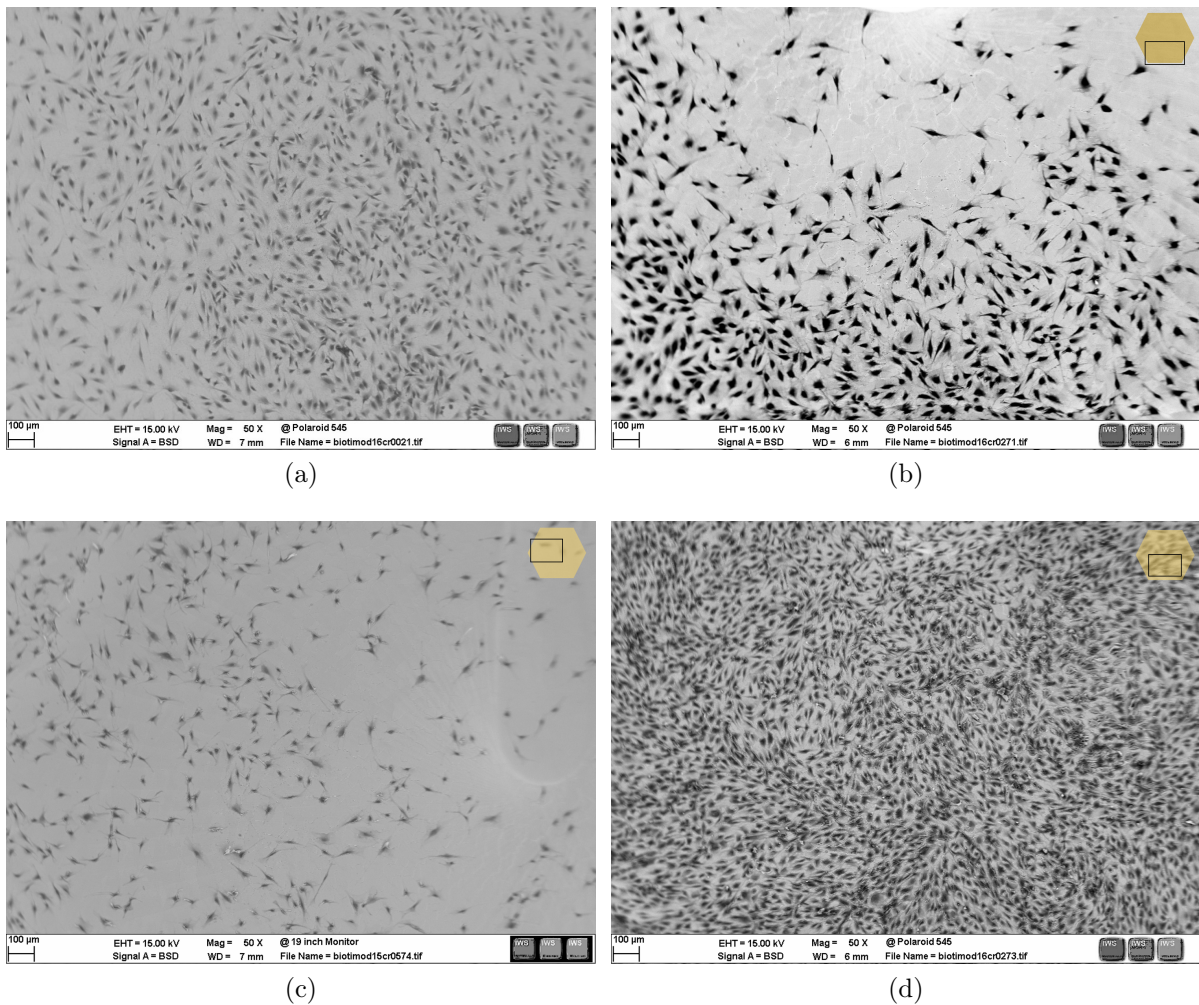
Figure 42: SEM images (BSE) of cell experiments on a) unstructured surface after 6 hs cultivation time and b), c) and d) wall array structured surface, after 6, 24 and 48 hs respectively.

For the unstructured ground surface (Fig. 42a), an uniform distribution of the cells was visible after a cultivation time of 6 hs. Compared to this behaviour, the pictures (42b) and (42c) reveal a reduced cell number for smooth areas within the wall array-hexagon

(Fig. 31) on the structured surfaces after cultivation times of 6 hs and 24 hs. However, after a cultivation time of 48 hs (Fig. 42d) this effect was no longer visible.

With increasing cultivation time, a raised amount of cells was visible on the structured surface. This is especially the case when comparing a 24 hs (Fig. 42c) and 48 hs (Fig. 42d) cultivation time. Therefore, a proliferation of the cells could be assumed.

No particular orientation of the cells due to the surface structure was visible for both types of surfaces even after longer cultivation times for wall array-hexagons.

Examples of morphologies obtained for 6 hs cultivation experiments on ground Ti15Mo (4000 SiC paper) (Fig. 43a) and wall array structured surface (Fig. 43b) are depicted. Furthermore, experiments on wall array samples after cultivation times of 24 hs (Fig. 43c) and 48 hs (Fig. 43d) are compared.
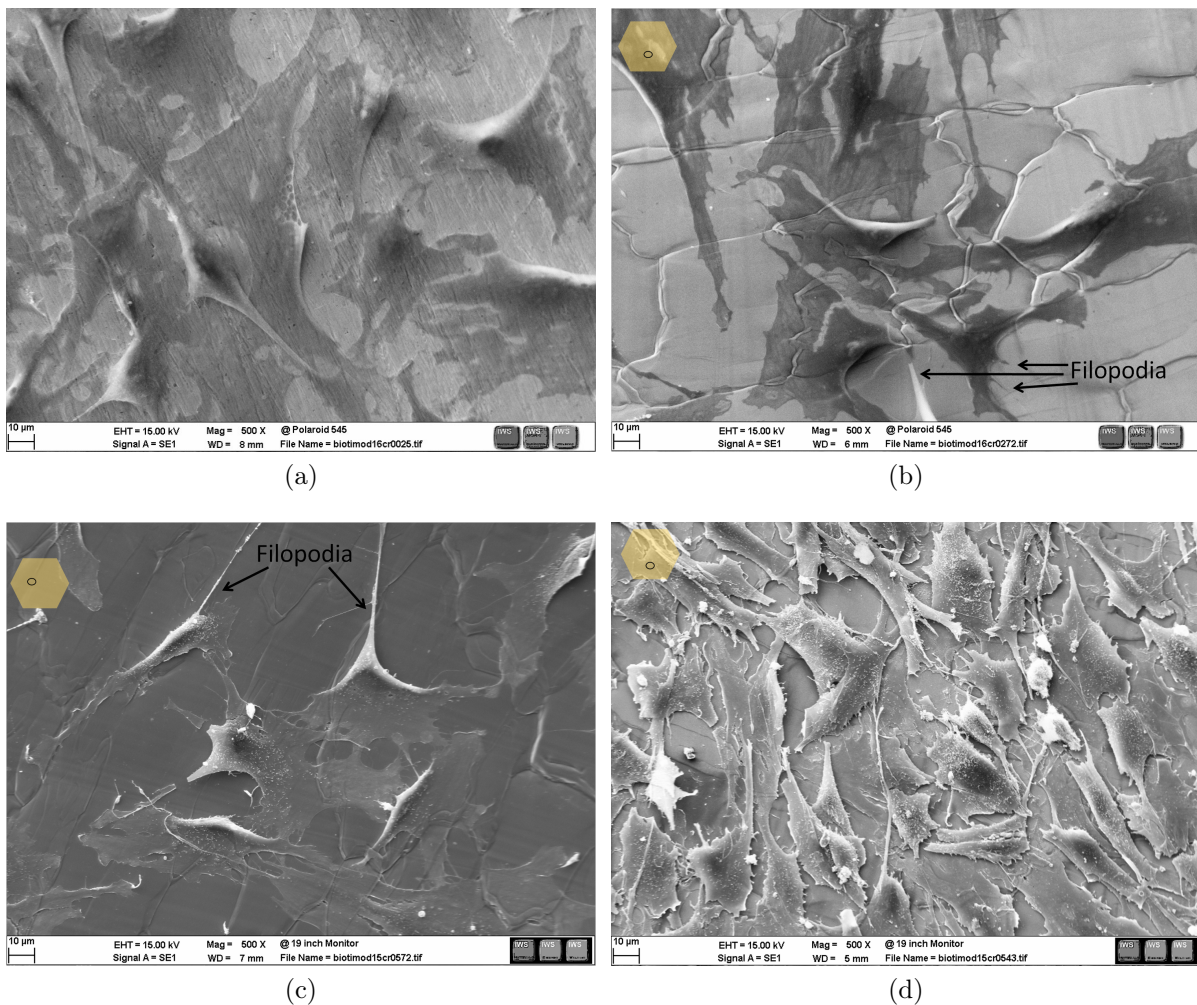
Figure 43: SEM images (SE) of cell experiments after 6 hs cultivation time on a) ground surface, b) wall array structured surface, c) after 24 hs on wall array array structured surface, d) after 48 hs on wall array structured surface.

The cells showed no significant discrepancy regarding their morphology on ground and wall array structured surface after a cultivation time of 6 hs. The cells appeared spread out, exhibited a polygonal morphology and showed long elongated actin filaments, known as filopodia (marked in Fig. 43c and Fig. 43b) which were extended in various directions. This filopodia anchor the cells with the surface and enable the cells to stay in contact with each other. After a longer cultivation time of 48 hs (Fig. 43d), the distribution was tighter and a strong overlapping of the cells was visible.

4.3 Influence of structuring process and heat treatments

4.3.1 Effect of structuring on microstructure

4.3.1.1 Pin and wall arrays created on the surface of Ti15Mo plates

An overview image of a pin array I structure (Fig. 44a) and a cross section of one pin structure, after a short etching time (Fig. 44b) are shown in Fig. 44. The end position of the electron beam for each single structure of the array (last arm of each hexagon) is highlighted in yellow. The white line indicates the position were the metallographic cross sections were made. The LOM image of one cross section shows the sequence of single weld pools, created by the electron beam process (Fig. 44b). The final arm of the single structure (marked by red arrow) indicates the shape of the weld pool.

(a)   (b)
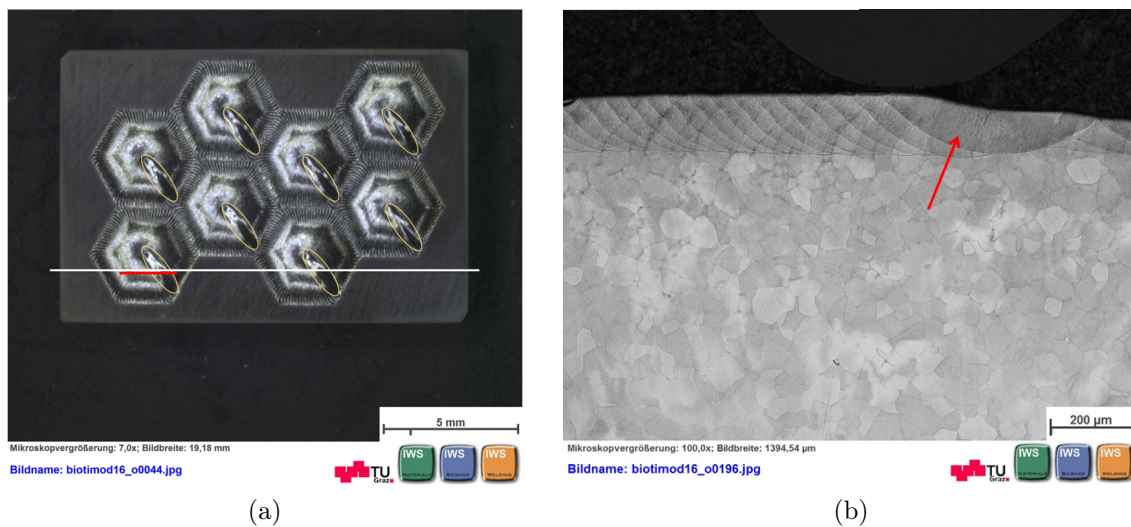
Figure 44: Pin array I: a) Stereo image of investigated 2x4 pin array, b) Cross section of single pin structure.

Figure 45a shows an overview image of a wall array I structure. The creation direction of figure arms (red arrow) and the cross section position (white line) are displayed. A detailed view of the left sector of a wall-hexagon is shown in the cross section depicted in Fig.

45b. The creation of the arms by the electron beam was carried out in counterclockwise direction. Consequently, the melt pools were created from left to right. Zones with different microstructures were observed, similar as in the pin array figure.

(a) (b)
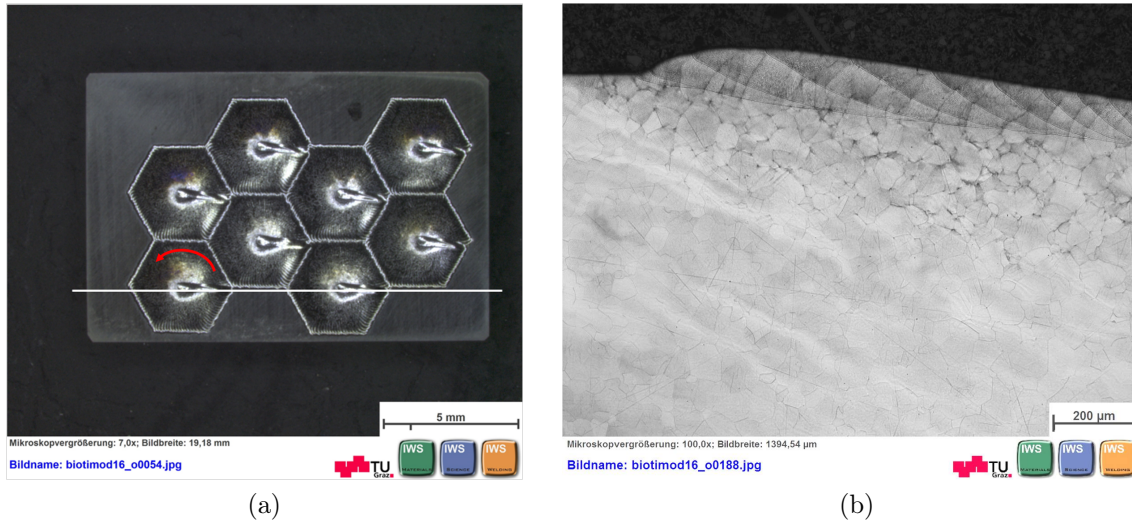
Figure 45: Wall array I: a) Stereo image of investigated 2x4 wall array with marked creation direction (red arrow), b) Cross section of single wall structure.

Structured zone

Figure 46 shows a cross sections of the centre region of a wall array-hexagon after a short etching time. Large columnar β grains with evident orientation and a width of 10-70 µm are visible in Fig. 46a. This kind of large grains produced during solidification was also reported in the context of selective laser melting (SLM) of α+β- and β-titanium alloys [59]. The melt pools were delimited by bright boundaries (marked by white arrows in Fig. 46b). An enrichment of these bands with Mo was assumed. The melt pool boundaries are potential nucleation sites for new β grains, but most of the grains grow across the melt pool boundaries (see Fig. 46b and Fig. 46c) in an epitaxial way and are forming elongated grains. The orientation of the elongated grains can be explained by the fact, that the grain growth is directed towards the top centre of the melt pool, in opposition to the thermal gradient maximum [59]. The elongated grains are tilted rightwards due to the sequence of structuring (counterclockwise) and partial remelting of previously created arms. A cellular substructure is visible inside the grains oriented to the top centre of the melt pool as well. According to literature [14, 15, 19] an amount of 10 wt. % Mo alloying element in titanium is enough to suppress the martensitic transformation during quenching and based on results in [60], this kind of structure inside the grains was identified as fine laminar β-phase.

Small displacements of melt pool boundaries are evident at certain positions (see Fig. 46b and Fig. 46c). This is possibly caused by slightly grain growth in the heat affected zone

60

beneath the new created weld pool.

With the help of Fig. 46c, which depicts a detailed view of the structured zone in the centre of the wall array-hexagon pit, the transition of the solidification mode from planar to cellular should be explained. Two exemplary chosen thin planar solidification regions at melt pool boundaries are enclosed by red striped lines.

(a)

(b)

(c)
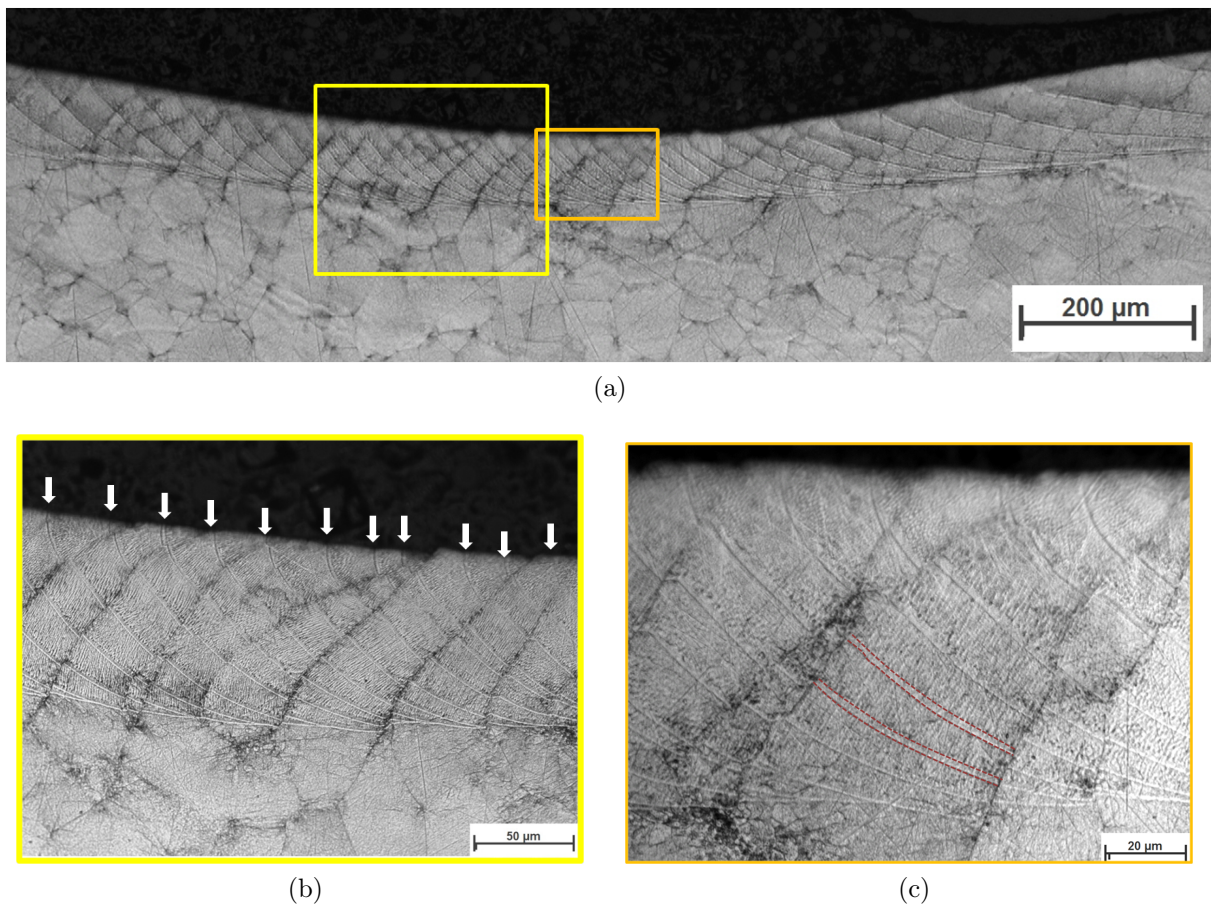
Figure 46: LOM images of wall array I-hexagon: a) Overview of region in the centre of a wall array-hexagon with a high amount of arm overlap, b) and c) Detailed views of region in the centre of the wall array figure in a).

The solidification of melt can be planar, cellular or dendritic. If for example during SLM the nascent solidification heat is dissipated to the solid layer beneath, the solidification front is stable and a planar solidification takes place, which can be achieved for pure metals in a wide process window. In this case the real temperature of the melt is always greater than the liquidus temperature of the material and randomly developing protrusions grow into a region with increased temperature and they melt again.

The solidification morphology for alloys is not only determined by the temperature gradient and the cooling rate but also by the concentration gradient on the liquid/solid phase boundary. In this context, the constitutional undercooling is essential [61, 62]. Figure 47 depicts the important correlations.
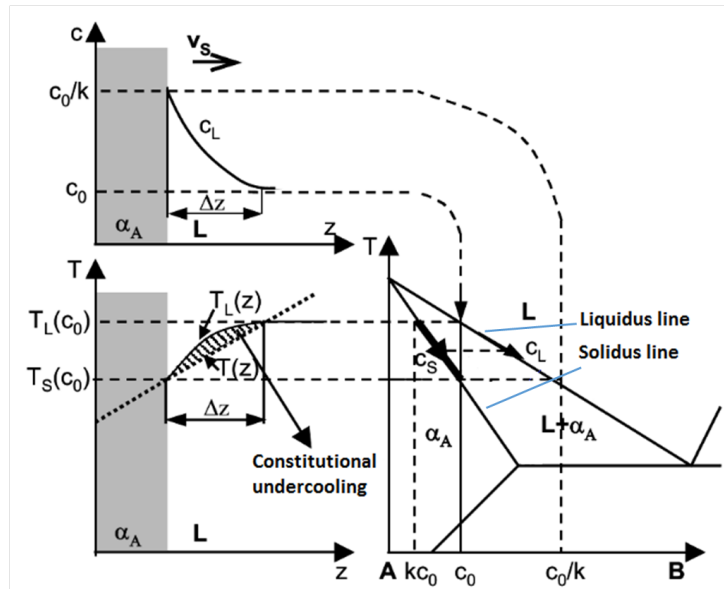
Figure 47: Constitutional undercooling, explained for a binary phase diagram A-B with solid solution formation (bottom right graph), top left graph: concentration gradient of B in the solid solution and in the melt (Acceptance: extremely small diffusion in the crystal), bottom left graph: course of the real temperature $T(z)$ in the melt and the liquidus temperature $T_L(z)$ in case of constitutional undercooling (adapted from [62]).

The graph on the right hand side shows a schematic phase diagram A-B with solid solution formation. The liquidus temperature decreases with increasing concentration of element B. L indicates the melt and α_A the solid solution. c_o is the initial concentration of the melt, $T_L(c_0)$ the liquidus- and $T_S(c_0)$ the solidus temperature. The equilibrium concentrations for a certain temperature within the solidification interval $\Delta T = (T_L(c_0) - T_S(c_0))$ (indicated by the bold line) are labelled by c_L and c_S. Their ratio $(k = c_S / c_L)$ is specified as partition coefficient. In the case of the considered phase diagram k<1 is valid. Because of the fact that k$\neq$1 a constant variation of the concentration takes place in the solidification interval. During the solidification of the melt (see arrow in the phase diagram A-B), the first forming crystals, with a concentration of kc_0, have a smaller B content, than the melt (c_0). An enrichment of the melt with element B occurs during further temperature lowering.

For very high cooling rates, only a partially diffusion equalisation takes place which leads to a concentration elevation of B-atoms with respect to c_0. This elevation drops exponentially along the distance Δz into the melt (top left image). Because the concentration

of element B drops along the distance Δz in front of the phase boundary, the liquidus temperature $T_L(z)$ will rise along Δz. The result is that despite an increasing temperature gradient, the real temperature of the melt $T(z)$ (with the gradient $G_z = dT/dz$) falls below the liquidus temperature $T_L(z)$, in front of the solidification front. This region (indicated by the hatched area in the bottom left graph) is defined as region of constitutional undercooling. The solidification front becomes unstable. Local fluctuation induced bulges of the solidification boundary are now able to grow into the undercooled melt and a cellular or even dendritic solidification starts [62]. According to Ref.[59], stability exists if the thermal gradient in the liquid phase at the solidification boundary is higher than the critical gradient $\delta T/\delta z_{crit}$ indicated in Eq. 10,

$$\frac{\delta T}{\delta z_{crit}} = -\frac{C_0}{\frac{D_L}{R}}\frac{(1-k)}{k}\frac{\delta T_L}{\delta C} \tag{10}$$

with:

C_0..............overall solute concentration
D_L ....solute diffusion coefficient in the liquid phase
k ....solute partition coefficient
R .... solidification grow rate
$\delta T_L/\delta C$.......gradient of the equilibrium melting point

In this case the local liquidus temperature $T_L(z)$ is always smaller than the temperature of the melt and planar solidification occurs. If it becomes lower than the critical gradient, a transition from planar to cellular solidification takes place. In Fig. 46c the transition from planar to cellular solidification mode is depicted. The concentration gradients (at the liquid/solid boundary) start to increase and the steady state is not reached as the solidification commences. This leads to a low value for the critical thermal gradient for planar solidification and results in a stable planar solidification front. The detailed view shows the thin regions (marked by red striped lines) at the melt pool boundaries where planar solidification is stable. After a certain time, when sufficient solute distribution has happened to raise the value of the critical thermal gradient above the value for the real thermal gradient, the transition from a planar to a cellular solidification occurs [59]. For this confirmation in the present work more studies will be needed.

Heat affected zone

To reveal the heat affected zone more clearly in the metallographic cross sections of the pin and wall arrays, a longer etching time was chosen for the samples before the LOM documentation was carried out.
Figure 48 shows overview and detailed images of the wall array-hexagon marked in Fig. 45a.
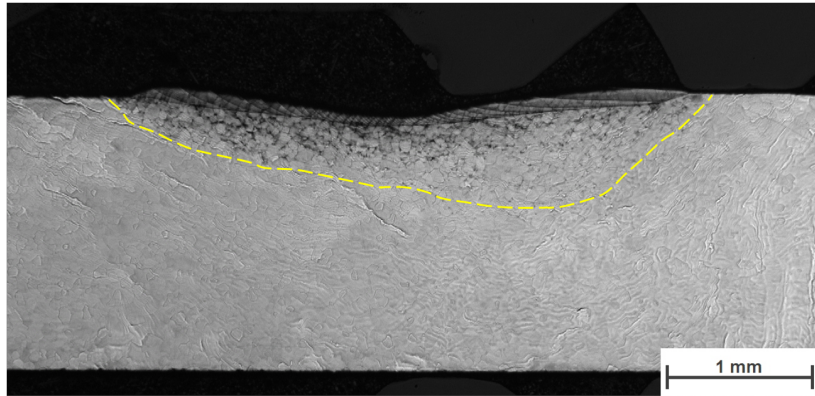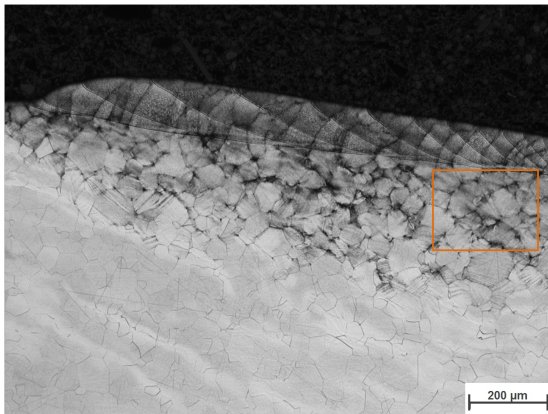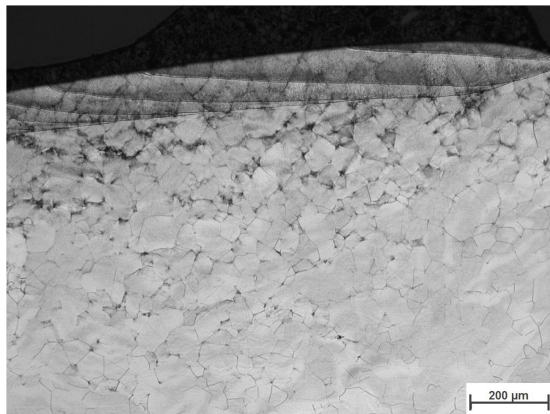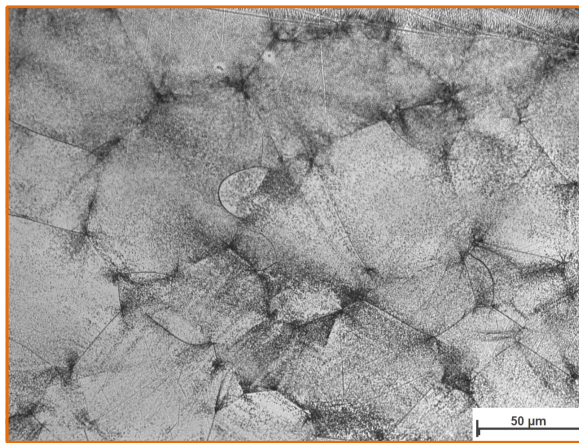
Figure 48: LOM images of wall array-hexagon: a) Overview with marked (yellow striped line) heat affected zone, b) View of the left sector, c) View of the right sector, d) Detailed view (500x) of selected region in the left sector.

After the preparation and etching of the samples, a region which had a different appearance compared to the base material was found. During the structuring process, the

microstructure in the region near to the melted area has changed. Very fine points, partially distributed over the grains, were identified (see Fig. 48d and Fig. 49).
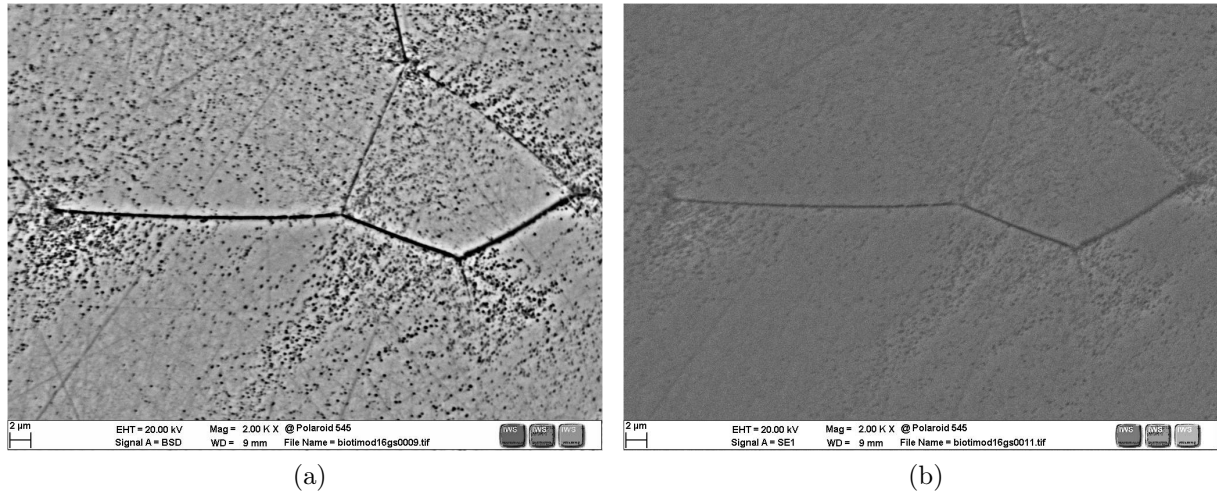
Figure 49: SEM images of grain in the heat affected zone (HAZ): a) BSE image, b) SE image.

The possibility, that the appearance of this zone was caused by etching artefacts had also been taken into account. A delineation of these regions was difficult to identify (see Fig. 48a). The region was more extended into the base material in the right sector of the wall array-hexagons. This could be caused by the fact, that the first and the last arm of the hexagons are located at this position as depicted in Fig. 45a. The consequence is a higher amount of heat input at this position. Furthermore, a larger width of the region was observed for the hexagon located on the right side in the front row of the wall array. Such a phenomenon is explained by the fact that this hexagon has three instead of two bordering hexagons. Hence, generation of an additional heat input is possible during the structuring process. This effect was also observed for the pin array-hexagons. It should be noted that the difference between these regions and the base material was weaker for the investigated pin array-hexagons. The differentiation was challenging, most likely due to the selected position of the metallographic cross sections. The selected position of the pin array was at a small distance away from the maximum pin height as shown in Fig. 44a, rather than directly at the pin's centre.

The difference in etching attack between the HAZ region and the base material could be related to the formation of thermal stress in the material. Very high heating and cooling rates are obtained during the processing. which can cause the thermal expansion and shrinking of the material, almost simultaneously, provoking the formation of internal stresses in the region below the structured surface (see Ref.[38] and Ref.[63] for detailed information).

65

Base material

In Fig. 50 the microstructure consisting of β grains of the base material is shown. The grain sizes are very similar to as observed for the as-delivered material (Fig. 37).
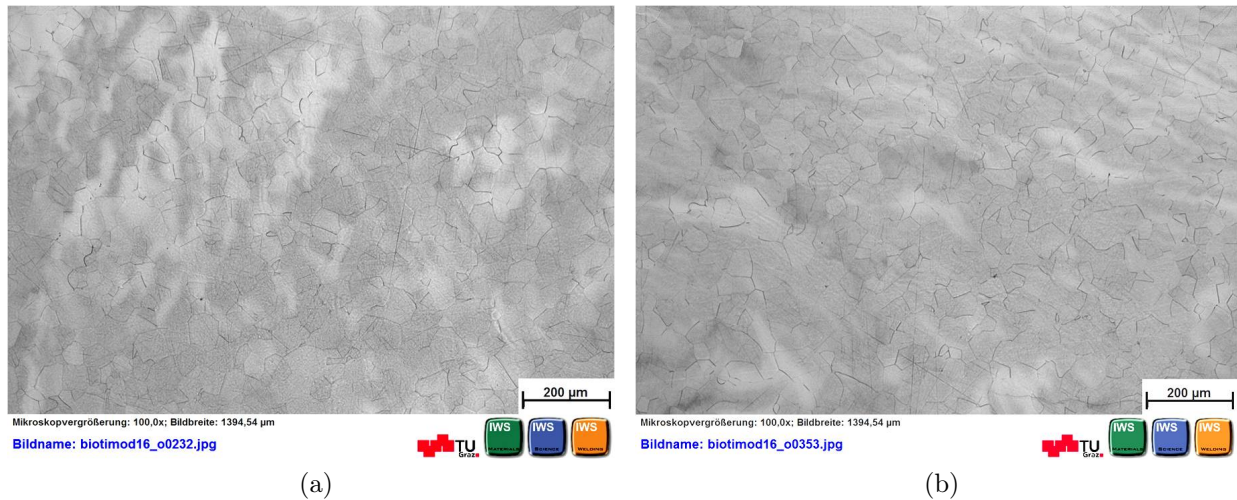
Figure 50: LOM images of base material beneath the structured region of a) pin array-hexagon and b) wall array-hexagon.

4.3.2   Effect of heat treatment on microstructure

4.3.2.1   As-delivered condition

A microstructure analysis of heat treated Ti15Mo base material, was carried out by LOM examination of the etched samples. A selection of optical micrographs is depicted in Fig. 51, for different cooling rates from β-phase. The microstructure depicted in Fig. 51a and Fig. 51b was obtained for a cooling rate of 100 K/min. Only metastable β grains were visible for this sample. No sign of α-phase precipitation could be observed. Similar observations were found for gas quenched samples and samples cooled by 50 K/min. However, a small amount of fine α-phase lamellae is visible at the grain boundaries and within the grains in the micrographs for samples cooled at rates of 20 K/min and 5 K/min. The lower cooling rate of 5 K/min led to a longer residence time for the sample at high temperatures which resulted in a higher amount of α-plate formation. No increment of the β grain size was visible for any of the different cooling rates.

(a)

(b)

(c)

(d)

(e)

(f)
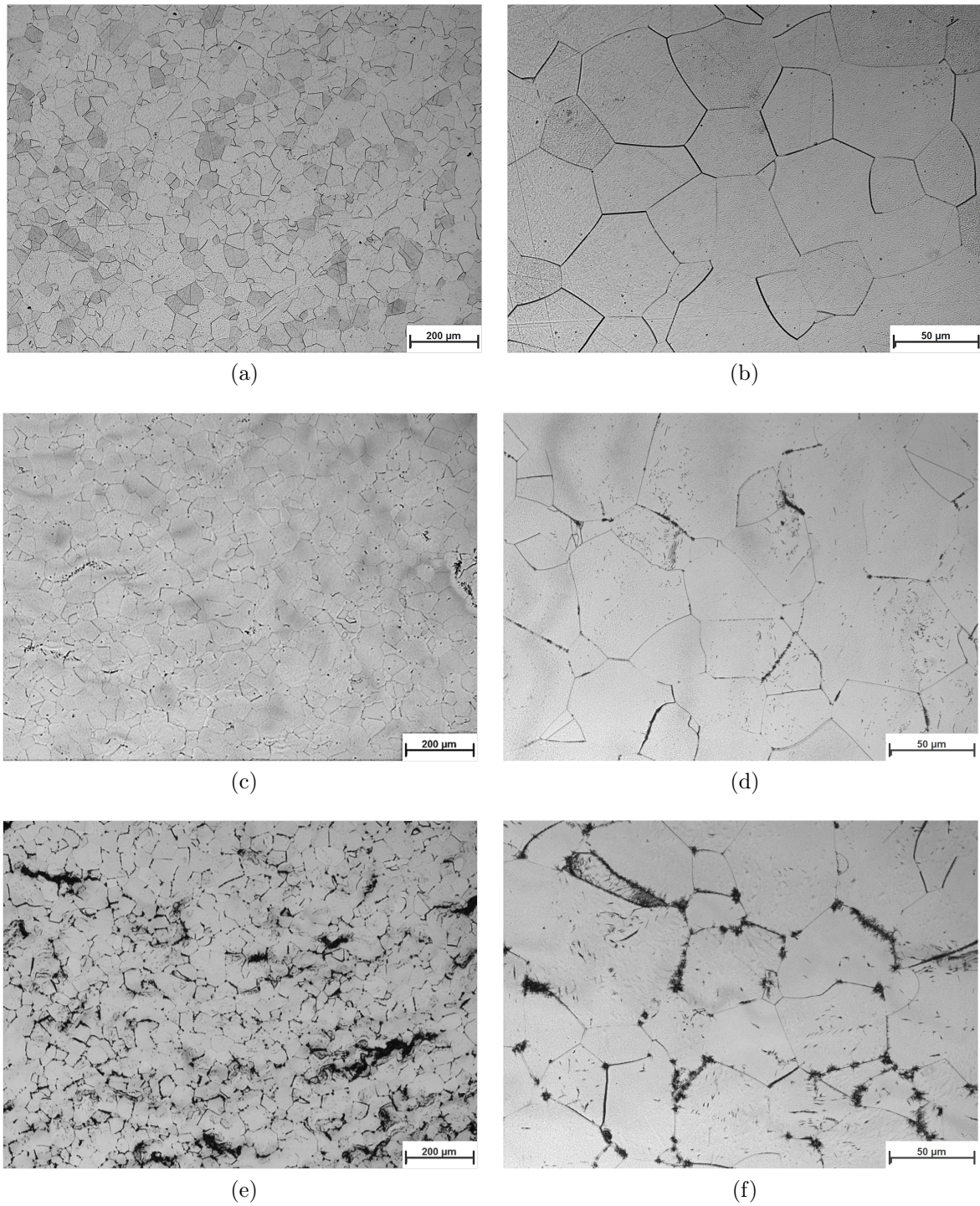
Figure 51: LOM images with different magnifications (100x and 500x) of the microstructure obtained for different cooling rates: a) and b) 100 K/min, c) and d) 20 K/min, e) and f) 5 K/min.

SEM investigation was carried out for the 5 K/min sample in order to perform a more detailed investigation of the α-precipitations. A selection of the results is depicted in Fig. 52. A predominant formation of fine α-Widmanstätten grain boundary (α_{WGB}) side plates, growing off the grain boundaries and grain boundary α-phase (α_{GB}) into the interior of the β grains (marked by the yellow arrows in Fig. 52a and Fig. 52b) was visible. Furthermore, a small amount of α-Widmanstätten Intragranular was observed for samples cooled by 5 K/min.
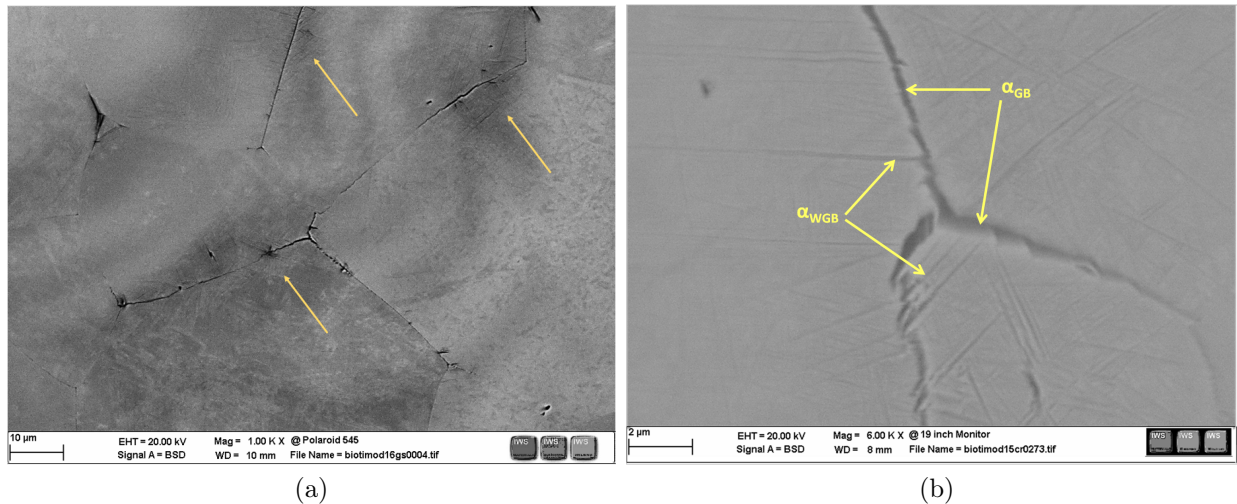
Figure 52: SEM images of samples cooled at 5 K/min: a) Distribution of α-phase at the grain boundary, b) Detail of the grain boundary with α-side plates.

4.3.2.2 Investigation of ageing treatment in structured Ti15Mo samples

Dilatometrie

Dilatometer measurements and certain heat treatments (shown in Table 9) of cut pin array structured Ti15Mo plates were carried out in order to obtain information about occurring phase transformations. Figure 53 shows the change in length with temperature during the heating process for all four samples.

The linear behaviour of the curves has a slope of $10 \cdot 10^{(-6)}$/K for a heating rate of 300 K/min. This value is similar to the thermal expansion of the material reported in [50] ($8.5 \cdot 10^{(-6)}$).
For a heating rate of 5 K/min a divergence from the linear growth is evident in an approximate temperature range from (220-550)°C. This behaviour can be caused by phase transformations happening in this temperature field [20, 64]. During heating, the volume expanded linearly up to ~ 220°C where a reduction of the expansion rate was observed. From 430°C to 550°C the volume expansion rate increased faster and then it became lin-

ear, as observed for 300 K/min. The deviation of the 5 K/min curves from the initial region of linear growth can be assumed as a measure of a volume effect caused by transformation [65].
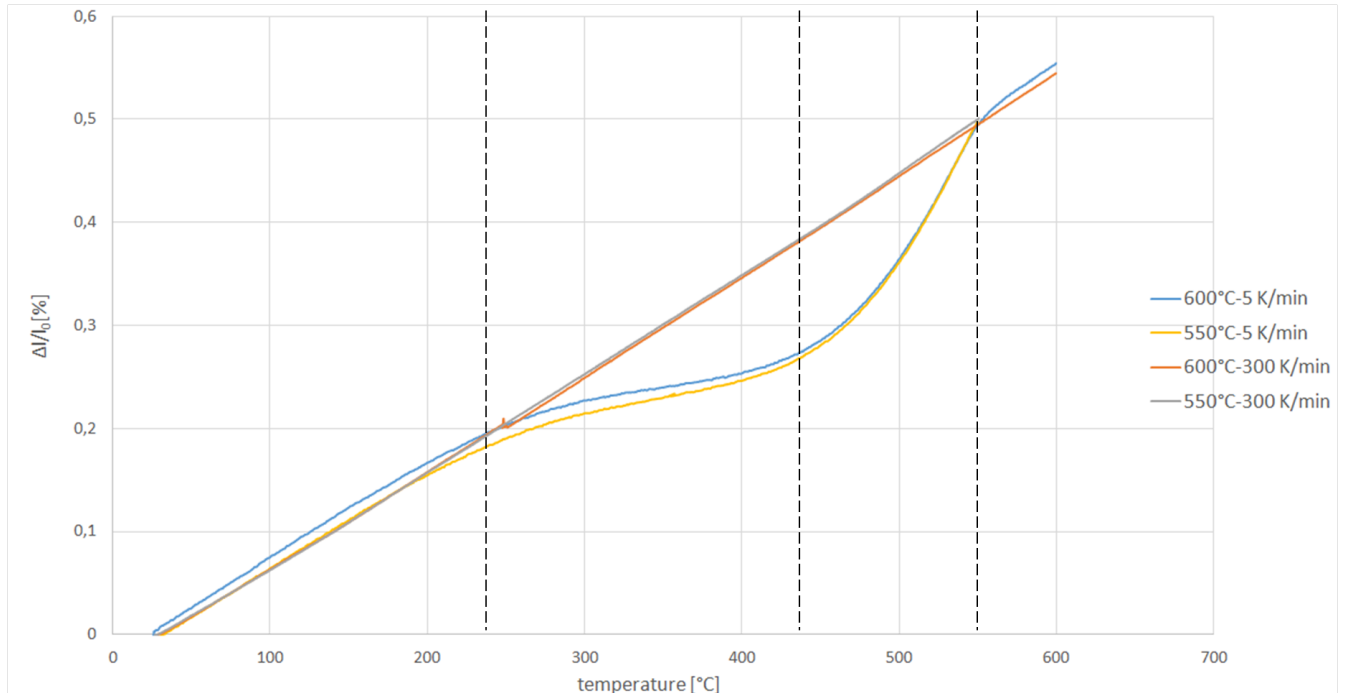
Figure 53: Change in length during heating for different heating rates.

The transformation processes, active during slow heating at a temperature range of 220°C to 550°C, are explained in more detail:

- **Region 220°C - 430°C**

  A $\omega_{ath} \to \omega_{iso}$ -phase transformation, the precipitation and the growth of ω_{iso}-particles are all expected during the slow heating in a temperature range of 225 to 356 °C [64]. In [66] the presence of ω_{iso}-phase was detected between ∼350 and 400°C during slow heating (5 K/min) for a metastable β-alloy (Ti-5Al-5Mo-5V-3Cr-1Zr). Moreover, Banerjee et.al. reports a linear contraction of approximately 5% associated with the isothermal β → ω-phase transition by a comparison between the corresponding lattice dimensions of the phases [16]. This could be an explanation for the region of slowed growth in the dilatometer curve.

- **Region 430°C - 550°C**

  The slope at a temperature of approximately 430°C reaches a larger value than during the linear growth. The expansion mechanism is a consequence of different occuring phase transitions in this temperature range. According to literature [64] a growth of the ω_{iso}-phase phase takes place up to a temperature of about 480°C. However, a simultaneous precipitation and growth of α-phase, with ω-phase acting as preferred nucleation site is happening. Ref.[20] reports the progressive vanishing of ω_{iso}-phase due to ω/α-phase transformation starting from a temperature of $\sim$300°C for a heating rate of 5 K/min for Ti12Mo. Ref.[66] also confirms the appearance of α-phase at $\sim$400°C while heating at 5 K/min.

  During the $\beta \rightarrow \alpha$-phase transition, a reduction of the c/a ratio below the ideal value for the hexagonal close packed structure takes place. Such a ratio decrease causes a decrease of the atomic density per volume compared to the value for the ideal closed packed structure. A small macroscopic increase of the volume occurs during the $\beta \rightarrow \alpha$-phase transition [15, 67].

  A complete dissolution of the ω-phase was observed in [64] at a temperature of 560°C. This temperature accords with the temperature in the end zone of the obtained dilatometer curve (Fig. 53), after which a linear behaviour is depicted. After this temperature (550°C) which indicates the expected ending of the phase transformation from ω_{iso}-to α-phase, conventional $\beta \rightarrow \alpha$-phase transformation occurs. This result is in good agreement with [20], in which the end of the phase transformation is reported in a temperature region below but close to 593°C for the metastable β-titanium alloy Ti12Mo during slow heating (5 K/min).

The course of the obtained dilatometer curve for 300 K/min and results in literature [66] suggest a suppression of the ω_{iso}-phase formation and the $\omega \rightarrow \alpha$-phase transformation mechanism for this heating rate. A direct $\beta \rightarrow \alpha$-phase formation is expected at higher temperatures.

Microstructure after ageing

To investigate the influence of different heating rates (5 K/min and 300 K/min) on the microstructure, micrographs were analysed via LOM, for heating temperatures up to 550°C and 600°C.

Figure 54 shows a comparison of microstructures in the structured zone (SZ), heat affected zone (HAZ) and base material (BM).
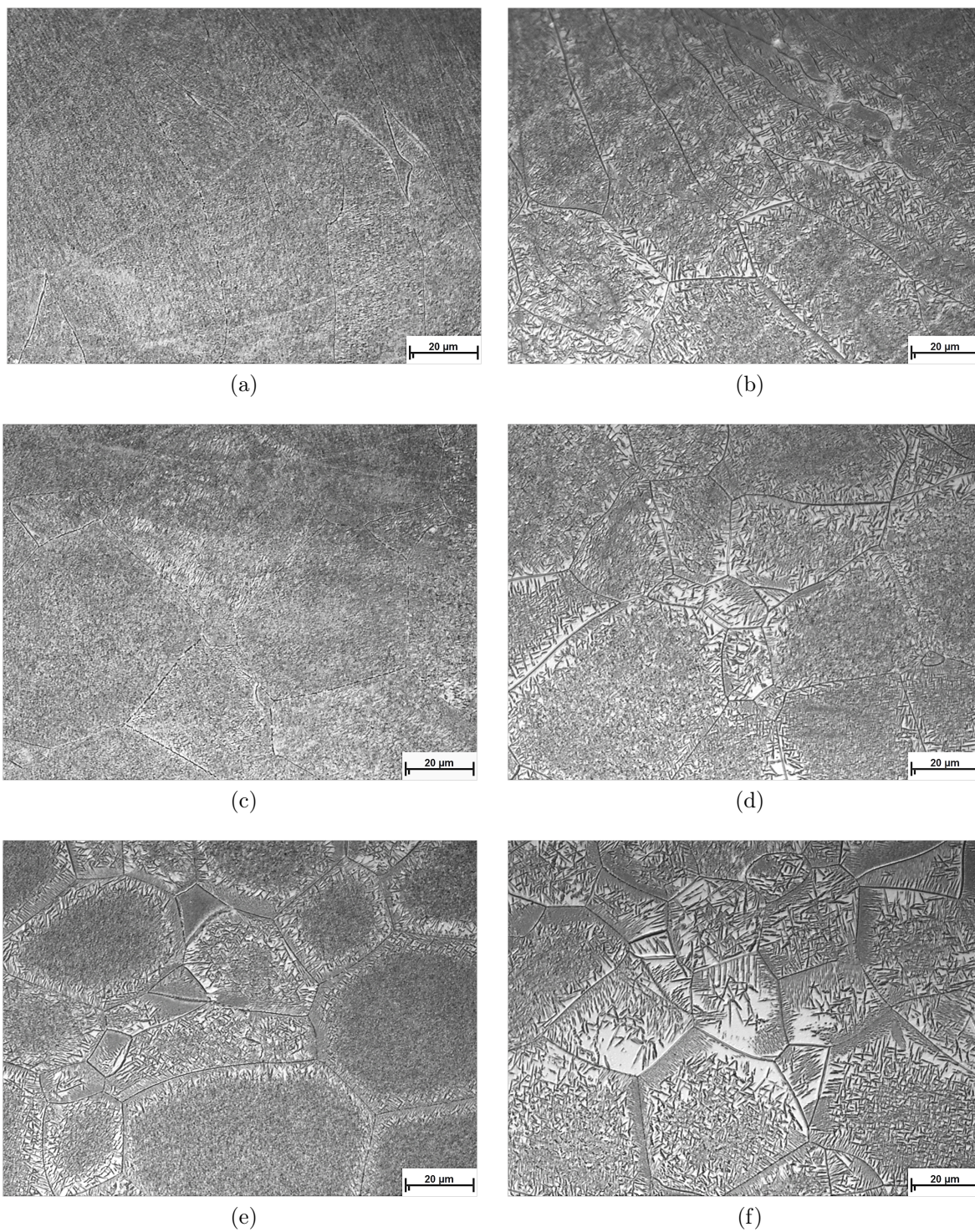
Figure 54: LOM images of the microstructure in the regions SZ, HAZ and BM obtained for two different heating rates and an ageing temperature of 600°C: 5 K/min a) SZ, c) HAZ and e) BM; 300 K/min b) SZ, d) HAZ and f) BM.

The material exhibited an α-β structure after the heat treatment. The melt pools in the SZ are separated by bright boundaries similarly as observed for the structured samples without heat treatment (see Fig. 46b).

A comparison between the two heating rates (5 K/min and 300 K/min) shows that a heating rate of 5 K/min results in a finer secondary α-lamella structure in all three regions. This fact can be caused by the difference in the formation mechanism of the α-plates. According to Ref.[66] a slow heating rate results in a homogeneous distribution of very fine α-plates. The developing ω_{iso}-phase can act as nucleation site for the α-phase in this case, which results in an increase of nucleation rate and the formation of very fine scale α-phase. This evolution of ω-phase can be correlated with the dilatometer measurements (Fig. 53). For high heating rates, the $\omega_{iso} \rightarrow$ α-phase transformation mechanism is suppressed and the only remaining direct transformation path $\beta \rightarrow$ α-phase is promoted. Starting from the β grain boundaries the α-transformation is followed by the grow of α-colonies (Widmanstätten grain boundary α-phase) from the grain boundary α (α_{GB}) / β interface [66].

Furthermore, a tendency of refinement of the α-lamella structure was observed in the three regions, following the order BM, HAZ, SZ. Unfortunately, the reasons for this tendency could not be fully clarified till the end of the thesis.

Several regions with white areas located around the boundaries of former β grains and partially within the grains were detected in the LOM images of both samples (in both HAZ and BM). However, this effect was much stronger in the sample heated up with 300 K/min (see Fig. 54f).

These areas can be related to segregations of β-stabilising elements like molybdenum and iron. Because of the dependence of the backscattering coefficient on the mean atomic number [68], the bright appearance of this area in SEM images (BSE mode) indicated an enrichment of elements with higher atomic number compared to titanium (Z=22). This would have been valid for the β-stabilising elements iron (Z=26) and molybdenum (Z=42), but unfortunately, the local variation of the composition was too small to be measured via EDX because of the limited resolution of the used detector. However, hardness measurements carried out in the BM within white areas (see Fig. 54f), suggested an enrichment of the more soft β-phase in this regions.

Figure 55 depicts a selection of SEM images of two samples heated up to 550°C with different heating rates (5 K/min and 300 K/min). The microstructure is compared in the SZ and BM.

(a)

(b)

(c)

(d)
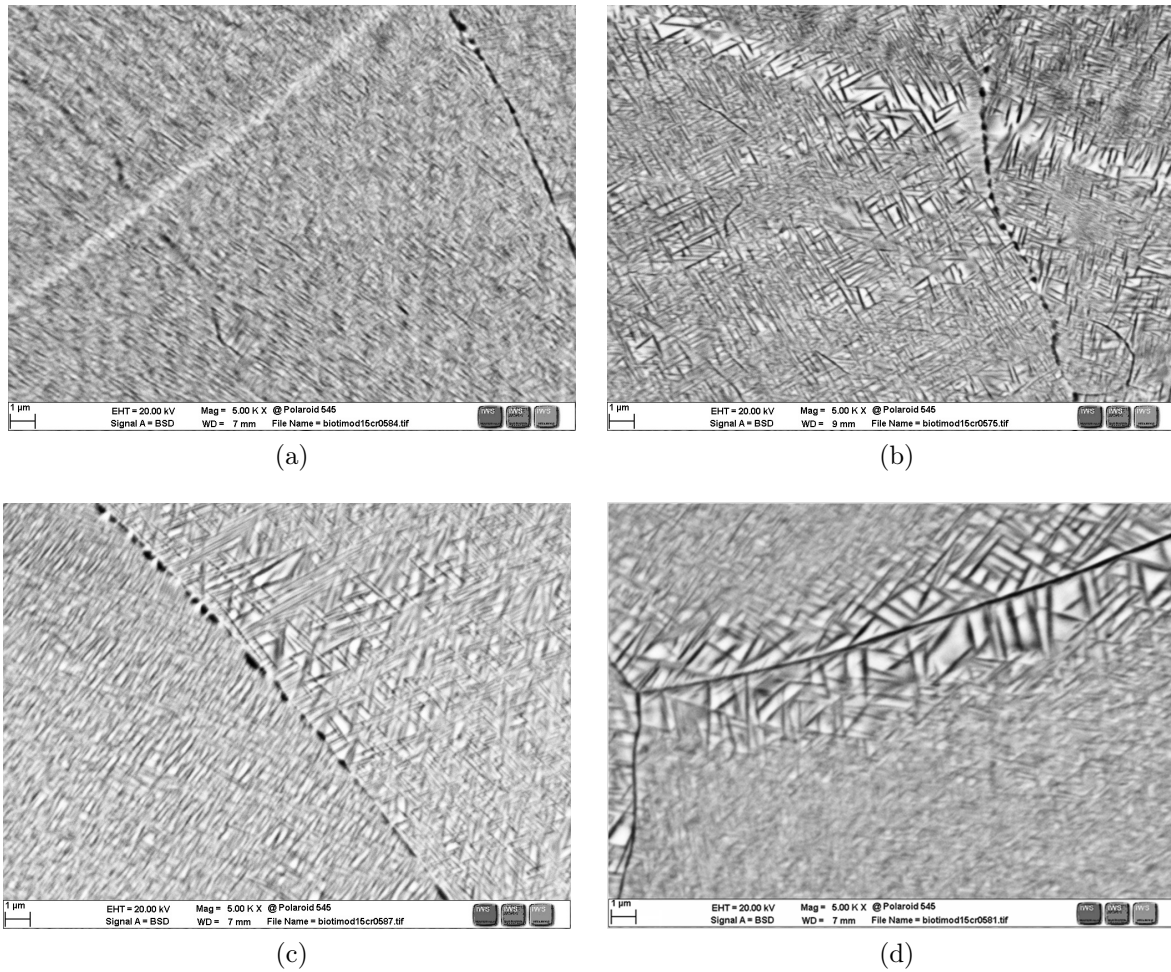
Figure 55: SEM images (BSE mode) in the regions SZ and BM of samples heated up to an ageing temperature of 550°C with two different heating rates: 5 K/min a) SZ, c) BM; 300 K/min b) SZ, d) BM.

The finer microstructure obtained for a heating rate of 5 K/min is clearly visible, which matches with the results from the LOM investigations. Fine α-lamellae appear black in the BSE images because of their lower Mo content. The melt pool boundaries in the structured zone appear bright in the BSE images. Such finding would suggest that there is an accumulation of high Z elements in this region. It also confirms the assumption of segregation effects and an enrichment of Mo along the melt pool boundaries due to the structuring process. The effect was more evident for the 300 K/min sample.

Figure 56 shows LOM images of the microstructure in SZ, HAZ and BM of a sample heated up to a temperature of 550°C with a heating rate of 300 K/min. By a comparison with the microstructure of a sample which was heated up to 600°C with the same heating rate (Fig. 54b, d, f), the influence of the heating temperature on the microstructure is discussed.

(a)
(b)

(c)
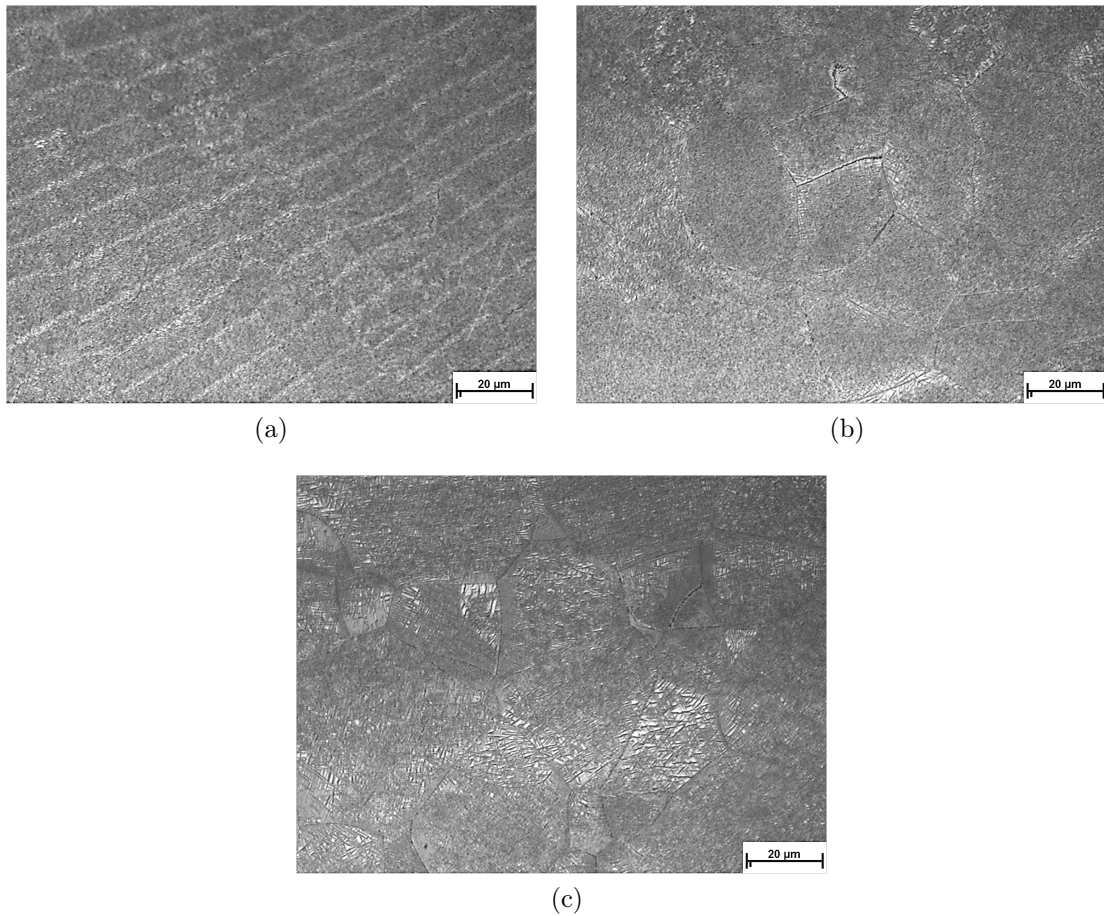
Figure 56: LOM images of the microstructure obtained for a heating rate of 300 K/min and an ageing temperature of 550°C in the regions a) SZ, b) HAZ and c) BM.

The comparison shows the more inhomogeneous distribution and coarser structure of α-lamellae for the heat treatment at 600°C compared to the microstructure obtained for a heating temperature of 550°C. Such a finding can be explained by an additional growing of the α-plates between 550°C and 600°C. Furthermore, a change in the transformation mechanism of the α-phase between 600°C and 550°C, which can result in a nucleation rate increase and decrease of the α-precipitate size is possible. [69] reports the formation of refined α-precipitates during isothermal ageing in the intermediate temperature range in contrast to the formation of coarse alpha precipitates for ageing at higher temperatures (700°C) for Ti15Mo. A new transformation pathway including β-phase separation and spinodal composition instability acting as precursor of refined α-precipitates was proposed in this context.

A comparison of the microstructure obtained for the samples of figures 56 and 54a, c and e (300 K/min, 550°C and 5 K/min, 600°C respectively) with respect of the fineness of the α-phase is somewhat more complex due to the high level of similarity. In the first sample, the high heating rate leads to a formation of thicker α-laths but the lower tem-

perature limits the size of α-precipitates. For the second sample, the opposite is valid. However, a tendency of more fine scale α-phase in the (300 K/min, 550°C) sample within the SZ and the HAZ could be determined via LOM images. This effect could not be confirmed for the BM. An REM documentation would have been necessary for a detailed investigation of the microstructure in the BM region.

4.3.3 Hardness measurements

Figure 57 compares the hardness values obtained for the investigated base material in different Ti15Mo samples. The results were analysed in 4 different groups:
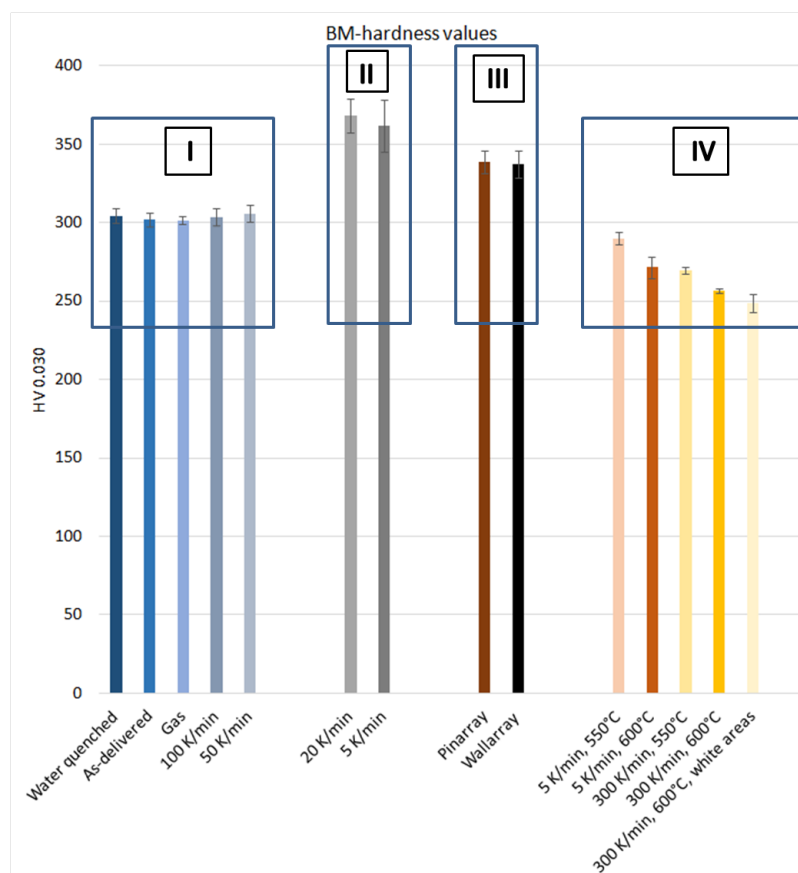
Figure 57: Comparison of the values of the base material hardness of different Ti15Mo samples.

Group I, samples heated above the β-transus temperature and cooled at fast cooling rates show similar hardness values. During quenching/cooling of the material from the β-phase field, formation of ω_{ath}-phase occurs [17, 19]. The microstructure consists of β grains and nanometer sized ω_{ath}-precipitates.

Group II, samples heated above the β-transus temperature and cooled at 20 K/min and 5 K/min

The slow cooling rate enables the formation of very fine α-plates, which can cause a hardening of the material. An additional strengthening effect can be attributed to the formation of ω_{iso}-phase, which can be enabled by the longer residence time of the samples at higher temperatures, allowing an increased solute diffusion during cooling. [70] reports the formation of ω_{iso}-phase in a β-titanium alloy for slow cooling from temperature above β-transus (cooling rate < 1°C/s below 500°C).

Group III, base material of structured samples

The hardness values for this group are between the values of group I and II. No indication of α-phase precipitation was found in this region of structured samples. It is assumed, that a warming up of the whole Ti15Mo plate occurs during the structuring process. The consequence is a formation of ω_{iso}-phase in the material. Such a formation would explain the slightly higher hardness values compared to group I. Various studies have proved the precipitation of this metastable phase during ageing [17, 18, 71], even for very short ageing times (e.g., 60 s at 500°C in [70]). A very rapid growth of ω-domains, existing in the material after quenching from temperatures above β-transus, during short term-ageing was reported in Ref.[70]. Furthermore, Cardoso et al. report a connection between a rapid hardening of Ti15Mo during the first minutes of ageing at 450°C and intense ω-phase precipitation during this time range [71].

Group IV, structured samples after heat treatment

According to Ref.[71] a complete depletion of the ω-phase occurs in Ti15Mo after ageing for 12 hs at 450°C, which is why a lack of ω_{iso}-particles is assumed for the 24 hs aged samples of group IV. Despite the appearance of α-lamellae in these samples, the hardness values are lower when compared to group II and III. Is has been reported in literature [71, 18] that the influence of the ω-phase concerning the strengthening of Ti15Mo is higher compared to the influence of refined scale secondary α-phase, formed during ageing treatment. During increasing ageing time, the ω-phase dissolves and is replaced by α-phase, which leads to a reduction in hardness [71]. The long ageing time of 24 hs results in a coarsening and strong overageing of the α-phase, which causes a reduction of hardness below the values obtained for group I. This correlates well with results in [57] for Ti15Mo heat treated at ageing temperatures of 600°C and 575°C for 24 hs.

A possible reason for the different hardness values within the group can be found by looking at the microstructure of the samples, especially at the size and distribution of the α-laths (Fig. 54). Uniformly distributed fine scale α-phase leads to high hardness values. Lower hardness values are related to a more coarser microstructure. [24] also reports a correlation between refinement of α-precipitates and increasing hardness values. The low hardness value, obtained for white areas in the base material of the (300 K/min, 600°C) sample, indicates the enrichment of β-stabilising elements in this areas.

Figure 58 shows a comparison and ranking of hardness values obtained for structured and

structured+heat treated samples in the regions SZ, HAZ and BM.
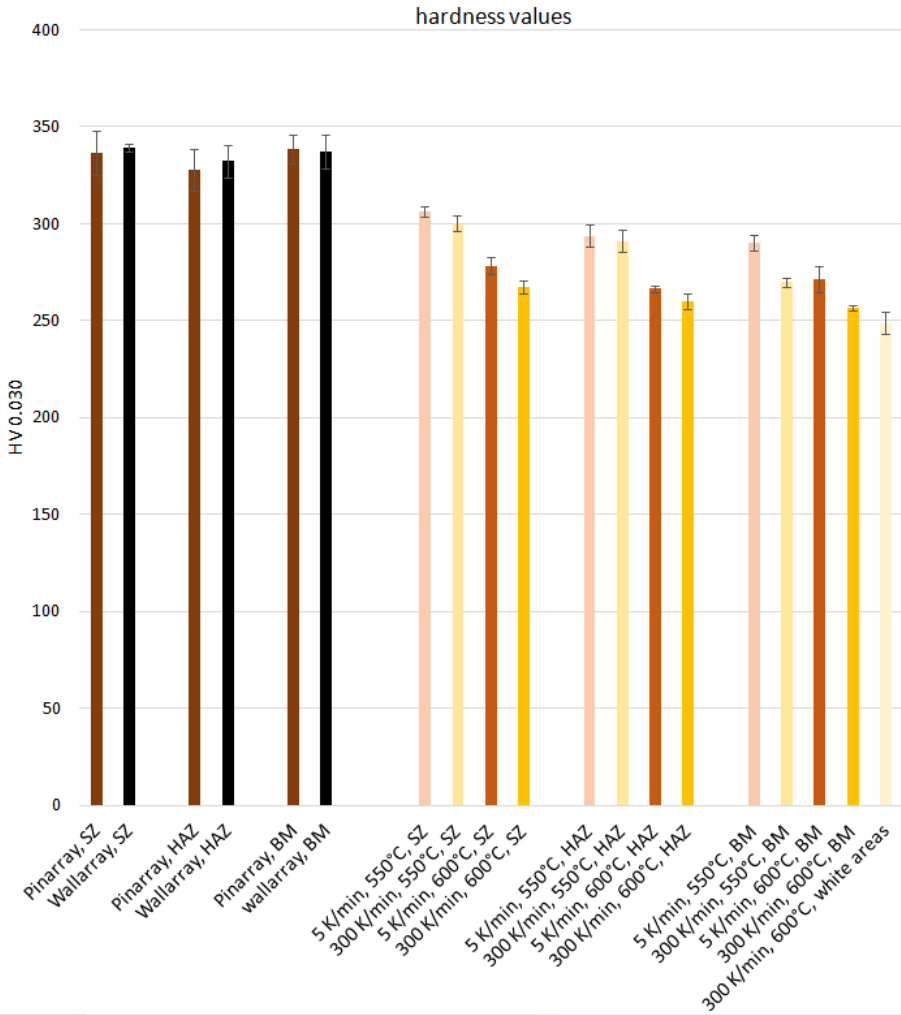
Figure 58: Comparison of the hardness values of structured, heat affected and base material zone of pin and wall array samples.

The previously mentioned observation for the base material regarding the lower hardness values for the structured+heat treated samples (group IV) compared to the values for the structured ones (group III) is also valid for the SZ and the HAZ of these samples (see Fig. 58). It is also assumed that a large amount of ω_{iso}-phase forms during the structuring process in the SZ and HAZ. For the structured+heat treated samples, an $\alpha+\beta$-microstructure was obtained also in the SZ and HAZ (Fig. 54 and Fig. 56). The connection between hardness values and distribution/size of the α-phase could also be observed for the SZ and HAZ of the structured+heat treated samples.

No strong difference of the hardness values in the different regions is visible for the structured samples while a SZ-HAZ-BM-decreasing tendency of the hardness is portrayed for the structured+heat treated samples.

5 Summary and Conclusion

As a part of this work, surface structures were created on Ti15Mo and TiGr2 by electron beam technique. Optimal parameters for the structuring process were identified to enable the production of a minimal weld pool width. An examination of generated surface structures was carried out by stereo microscopy, light optical microscopy, scanning electron microscopy and roughness measurements. Cell experiments with pre-osteoblast cells (MC3T3-E1) were performed on structured Ti15Mo plates to investigate the influence of surface modifications on the cell growth and morphology. The main results are the following:

- A minimal *weld pool width* of (0.159 ± 0.006) mm was obtained on TiGr2 with a parameter setting of: U_A = 80 kV, I_B = 1.2 mA and v = 355.44 mm/s, which corresponds to an energy input per length (EL) of 0.270 J/mm.

- The surface of pin and wall array structures on Ti15Mo created with parameters used for cell experiments appeared homogeneous, without defects or pores. Areas in the centre of the hexagon figures appeared more smooth than regions with small arm overlap at the edge regions of the hexagons.

- For the pin and wall arrays, created with optimal parameters for a minimal weld pool width, on Ti15Mo the possibly too low EL led to a lack of molten areas within the structure.

- The choice of the figure (wall or pin array) and the EL had influence on roughness, surface enlargement (SE) and the achieved pin height and pit depth. Furthermore, different roughness values were obtained within a single hexagon structure of a figure array due to different arm overlap levels. The lowest value was obtained for a wall array II structure, created with optimal parameters in a region with high arm overlap level close to the centre of the figure: R_a = (1.5 ± 0.1) μm. Regions with low arm overlap at the edge of the hexagons exhibited the highest roughness values, whereby the highest value: R_a = (5.4 ± 0.4) μm was achieved for a pin I structure created with parameters used for cell experiments. The wall array II figure also exhibited the lowest values for S_a (2.7 μm), SE (22.7 %) and the pit depth (55.2 ± 2.2) μm, while the highest values were obtained for the pin I structure: S_a (5.1 μm), SE (50.5 %) and pin height (240.7 ± 5.2) μm.

- After a cultivation time of 6 hs and 24 hs, a reduced cell number was observed for smooth areas (R_a < 2.6 μm) within the wall array-hexagon while an uniform distribution of the cells was visible on ground Ti15Mo surface after culturing for 6 hs. After culturing for 48 hs this effect was no longer visible and the structured Ti15Mo surface was uniformly covered. By increasing the incubation time a raised amount of cells was visible on the structured surface. Therefore, a proliferation of the cells can be assumed. No significant discrepancy regarding the morphology of the cells on ground or structured Ti15Mo surface was visible after a cultivation time of 6 hs. The cells were flat, exhibited a polygonal morphology and showed numerous filopodia extensions. After a longer cultivation time a tight distribution and strong

overlap of the cells was observed. In summary the cell behaviour on structured Ti15Mo surface can be assessed as positive.

The microstructure of the base material in as-delivered condition and microstructural changes due to the structuring process and performed heat treatments were investigated using light optical microscopy and scanning electron microscopy. Furthermore, dilatometer measurements were performed to obtain information about occurring phase transformations during heat treatments. Examinations regarding the influence of the structuring process and heat treatments on hardness values were carried out. The summarised results are listed below:

- The microstructure of the base material in as-delivered condition only consisted of metastable β grains. No indication of α-phase could be found. In this sample the measured hardness was (302 ± 4) HV0.030.

- Three zones with different microstructure were observed in cross sections of pin and wall array structured Ti15Mo plates: In the **structured zone (SZ)** large columnar grains of β-phase with a width of (10-70) μm were observed. Furthermore, a cellular substructure consisting of fine lamellar β-phase was visible within the grains. This substructure as well as the columnar grains are oriented towards the top centre of the melt pool. Furthermore, narrow regions generated by planar solidification which occurs at the beginning of the solidification process are visible. The shape of the visible melt pools are defined by Mo bands. The reason for the different appearance of the **heat affected zone (HAZ)** could not be conclusively clarified. It is assumed, that the very fine black points which were observed in this region after etching represented etching artefacts. A possible cause of the difference in etching attack can be the formation of thermal stress in the region below the structured surface due to the very high heating and cooling rates which occur during the process. The microstructure of the **base material (BM)** was very similar for as-observed and for the as-delivered material.
The values for the hardness measurements in the three zones were higher compared to the value obtained for the base material, which is explained by the formation of ω_{iso} -phase in each of the three regions.

- An examination of the influence of different cooling rates from β-phase on the microstructure and hardness of Ti15Mo base material revealed the appearance of fine α-phase lamellae at the grain boundaries and inside the β-phase grains for a cooling rate of 20 K/min. A lower cooling rate of 5 K/min led to a higher amount of α-phase formation. These two samples exhibited the highest hardness values ((362 ± 17) HV0.030 for 5 K/min, and (368 ± 11) HV0.030 for 20 K/min), which was attributed to the existence of very fine α-phase and the hardening ω_{iso} -phase in these samples. The microstructure and hardness of samples cooled with higher rates from the β-phase field were comparable with the results for the as-delivered material.

- Dilatometer curves showed a divergence from the linear growth in an approximate temperature range from (220-550)°C for a heating rate of **5 K/min** which was attributed to phase transformations happening in this temperature range. A distinction was made between the temperature region (220-430)°C for which a reduction in

the expansion was observed in the curve and the adjacent region (430-550)°C which was characterised by a faster increase of volume compared to the linear growth. Within the first region a high amount of $\omega_{ath} \to \omega_{iso}$-phase transformation, precipitation of ω_{iso}-phase and a growing of ω_{iso}-particles was expected whereby the second region was governed by the precipitation and growing of α-phase, with ω-phase acting as preferred nucleation site. At the temperatures higher than 550°C an ending of the phase transformation from ω_{iso}-to α-phase was assumed. Conventional $\beta \to$ α-phase transformation was expected to occur at higher temperatures.

The course of the obtained curve for a heating rate of **300 K/min** suggested a suppression of the $\omega \to \alpha$-phase transformation for this heating rate and a direct β $\to \alpha$-phase formation was expected.

- Investigations of the microstructure of structured Ti15Mo samples after different heat treatments, revealed the significant influence of the applied heating rate (5 K/min and 300 K/min) and ageing temperature (550°C and 600°C) on the distribution, size and amount of α-lamellae within the developed α-β structure. The finest α-plates in all three region (SZ, HAZ and BM) were obtained for a heating rate of 5 K/min and an ageing temperature of 550°C, which was attributed to ω-phase assisted nucleation. This microstructure also led to the highest hardness values in this sample group, whereby a decreasing tendency regarding the fineness of the α-plates from SZ to HAZ to BM was observed which was reflected in the hardness values: (SZ: (306 ± 3) HV0.030, HAZ: (294 ± 6) HV0.030 and BM: (290 ± 4) HV0.030). For higher heating rates of 300 K/min the only remaining direct transformation path $\beta \to \alpha$-phase was promoted which led to a more coarse α-lamellae structure and corresponding smaller hardness values. The ageing time of 24 hs led to overageing of the α-phase which resulted in reduced hardness values lying partially below the value for the as-delivered material.

Conclusion

The creation of surface structures with different roughness, free of defects and pores, using EBW is possible. High values for the surface enlargement could be obtained which is preferable regarding the enlarged area of contact between an implant and the surrounding tissue, leading to higher adhesions strengths compared to a smooth ground surface with smaller contact area. Regarding the utilisation of optimal parameters to obtain a minimal weld pool width, an adjustment of parameters should be carried out to prevent not melted areas within the figure array and ensure a complete structuring of the surface. The cell behaviour on structured Ti15Mo surface can be assessed as positive. The cells exhibited a polygonal morphology and showed long elongated actin filaments (filopodia). Proliferation of the cells was visible after longer cultivation time.

Investigations of the microstructure in the three different regions SZ, HAZ and BM revealed that no formation of α-phase occurs during the structuring process. Such result is beneficial due to the increase of the elastic modulus with increasing volume fraction of fine α-phase, which plays a more dominant role than the ω-phase in this context. This is important because low elastic modulus values are preferred for implant materials to prevent stress shielding. The only slightly higher hardness values of the structured samples

compared to the values for the as-delivered condition suggest the formation of only a small amount of ω_{iso}-phase which is important because of the embrittling behaviour of this phase if precipitated in higher quantities.

The amount of secondary α-phase must be kept as low as possible during the heat treatment of structured samples if considering the application as implant material. Furthermore, a limitation of the ω-phase needs to be done due to its modulus raising property in order to utilise the positive strengthening effect without the occurrence of embrittlement.

Outlook

By utilisation of optimal parameters for the structuring a possible reduction of the beam focus, which represents an additional determining factor for the weld pool width, could be obtained by lowering of the working distance.
To obtain more precise information about the processes which occur during the structuring process, transmission electron microscopy could be used to reveal ω-particles. Furthermore, especially the structured region should be investigated in more detail using high resolution SEM, and EBSD. Thermodynamic modelling should be performed in order to obtain a better understanding of the different solidification processes which occur in this region.
To clarify the influence of different surface structures and roughness values on the adhesion, proliferations activity and morphology of osteoblastic cells, further studies including improved cell number counting strategies need to be done. It would be desirable to obtain the information about size and shape of the cell nucleus and shape and orientation of the cytoskeleton with the use of fluorescence microscopy. A colouring of the focal adhesions can give information about the cell-surface interaction.

References

[1] A. Wennerberg and T. Albrektsson. Effects of titanium surface topography on bone integration: a systematic review. *Clinical Oral Implants Research*, 20(SUPPL. 4):172–184, 2009.

[2] T.S.N. Silva, D.C. Machado, C. Viezzer, A.N. Silva Júnior, and M.G.d. Oliveira. Effect of Titanium Surface Roughness on Human Bone Marrow Cell Proliferation and Differentiation: An Experimental Study. *Acta Cirurgica Brasileira*, vol.24:200–205, 2009.

[3] D. F. Williams. *Definitions in biomaterials: proceedings of a consensus conference of the European Society for Biomaterials, Chester, England, March 3-5, 1986*, volume 4. Elsevier Science Ltd, 1987.

[4] G. Heimke and D. Stock. Clinical application of ceramic osseo - or soft tissue - integrated implant. *Orthopedic Ceramic Implants*, 1984.

[5] B.D. Ratner, A.S. Hoffman, F.I. Schoen, and J.E. Lemons. *Biomaterials Science: An Introduction to Materials in Medicine*. Academic Press, 1996.

[6] R.B. Heimann and H.D. Lehmann. *Bioceramic Coatings for Medical Implants-Trends and Techniques*. Wiley-VCH, Weinheim, Germany, 1st edition, 2015.

[7] M.J. Yaszemski, D.J. Trantolo, K. Lewandrowski, and V. Hasirci. *Biomaterials in Orthopedics*. Marcel Dekker, Inc., New York, 2004.

[8] H.J. Rack and J.I. Qazi. Titanium alloys for biomedical applications. *Materials Science and Engineering: C*, 26(8):1269–1277, 2006.

[9] M. Long and H.J. Rack. Titanium alloys in total joint replacement–a materials science perspective. *Biomaterials*, 19(18):1621–39, 1998.

[10] M.A.-H. Gepreel and M. Niinomi. Biocompatibility of Ti-alloys for long-term implantation. *Journal of the Mechanical Behavior of Biomedical Materials*, 20:407–415, 2013.

[11] J.A. Disegi. Titanium alloys for fracture fixation implants. *Injury*, 31(SUPPL. 4):D14–D17, 2000.

[12] G. Lütjering and J.C. Williams. *Titanium*. Engineering Materials, Processes. Springer Berlin Heidelberg, 2007.

[13] M. Niinomi. Mechanical properties of biomedical titanium alloys. *Materials Science and Engineering: A*, 243(1-2):231–236, 1998.

[14] I.P. Polmear. *Light Alloys-From Traditional Alloys to Nanocrystals*, volume 2. Elsevier, 2006.

[15] C. Leyens and M. Peters. *Titanium and Titanium Alloys*. Wiley-VCH, 2003.

[16] S. Banerjee and P. Mukhopadhyay. *Phase Transformations - Examples from Titanium and Zirconium Alloys*. 2007.

[17] M. Sabeena, A. George, S. Murugesan, R. Divakar, E. Mohandas, and M. Vijayalakshmi. Microstructural characterization of transformation products of bcc β in Ti-15 Mo alloy. *Journal of Alloys and Compounds*, 658:301–315, 2016.

[18] S. Nag, R. Banerjee, and H.L. Fraser. Microstructural evolution and strengthening mechanisms in Ti-Nb-Zr-Ta, Ti-Mo-Zr-Fe and Ti-15Mo biocompatible alloys. *Materials Science and Engineering: C*, 25(3):357–362, 2005.

[19] W.F. Ho. Effect of omega phase on mechanical properties of Ti-Mo alloys for biomedical applications. *Journal of Medical and Biological Engineering*, 28(1):47–51, 2008.

[20] F. Sun, F. Prima, and T. Gloriant. High-strength nanostructured Ti-12Mo alloy from ductile metastable beta state precursor. *Materials Science and Engineering: A*, 527(16-17):4262–4269, 2010.

[21] J.D.C Teixeira, B. Appolaire, E. Aeby-Gautier, S. Denis, G. Cailletaud, and N. Späth. Transformation kinetics and microstructures of Ti17 titanium alloy during continuous cooling. *Materials Science and Engineering: A*, 448(1-2):135–145, 2007.

[22] S.M.C. van Bohemen, A. Kamp, R.H. Petrov, L.A.I. Kestens, and J. Sietsma. Nucleation and variant selection of secondary α plates in a β Ti alloy. *Acta Materialia*, 56(20):5907–5914, 2008.

[23] F. Prima, P. Vermaut, G. Texier, D. Ansel, and T. Gloriant. Evidence of α-nanophase heterogeneous nucleation from ω particles in a β-metastable Ti-based alloy by high-resolution electron microscopy. *Scripta Materialia*, 54(4):645–648, 2006.

[24] N. Clément, A. Lenain, and P.J. Jacques. Mechanical property optimization via microstructural control of new metastable beta titanium alloys. *JOM*, 59(1):50–53, 2007.

[25] Y. Ohmori, T. Ogo, K. Nakai, and S. Kobayashi. Effects of omega-phase precipitation on beta to alpha, alpha'' transformations in a metastable beta titanium alloy. *Materials Science and Engineering: A*, 312(1-2):182–188, 2001.

[26] S. Azimzadeh and H.J. Rack. Phase transformations in Ti-6.8Mo-4.5Fe-1.5Al. *Metallurgical and Materials Transactions A*, 29(10):2455–2467, 1998.

[27] D. Kuroda, M. Niinomi, M. Morinaga, Y. Kato, and T. Yashiro. Design and mechanical properties of new beta type titanium alloys for implant materials. *Materials Science and Engineering: A*, 243(1-2):244–249, 1998.

[28] X. Liu, P. Chu, and C. Ding. Surface modification of titanium, titanium alloys, and related materials for biomedical applications. *Materials Science and Engineering: R: Reports*, 47(3-4):49–121, 2004.

[29] M. Kulkarni, A. Mazare, P. Schmuki, and A. Iglic. Biomaterial surface modification of titanium and titanium alloys for medical applications. In *Nanomedicine*, pages 111–136. One Central Press, 2014.

[30] J. Davies. Understanding peri-implant endosseous healing. *Journal of dental education*, 67(8):932–949, 2003.

[31] A. Bandyopadhyay, F. Espana, V.K Balla, S. Bose, Y. Ohgami, and N.M. Davies. Influence of Porosity on Mechanical Properties and in Vivo Response of Ti6Al4V Implants. *Acta Biomaterialia*, 6:1640–1648, 2010.

[32] W. Xue, B.V. Krishna, A. Bandyopadhyay, and S. Bose. Processing and biocompatibility evaluation of laser processed porous titanium. *Acta Biomaterialia*, 3(6):1007–1018, 2007.

[33] M. Bächle and R.J. Kohal. A systematic review of the influence of different titanium surfaces on proliferation, differentiation and protein synthesis of osteoblast-like MG63 cells, 2004.

[34] S. Kakehi, S. Takeda, and M. Nakamura. Effect of Titanium Surface Roughness on the Cytocompatibility of Osteoblast-like Cells. *Journal of Oral Tissue Engineering*, 4(2):77–88, 2006.

[35] K. Anselme, P. Linez, M. Bigerelle, D. Le Maguer, A. Le Maguer, P. Hardouin, H. F. Hildebrand, A. Iost, and J. M. Leroy. The relative influence of the topography and chemistry of TiAl6V4 surfaces on osteoblastic cell behaviour. *Biomaterials*, 21(15):1567–1577, 2000.

[36] M. Stütz. *Surface Structuring of Biodegradable Mg-alloys by Electron Beam Technique*. Master's Thesis, 2014.

[37] H. Kuchling. *Taschenbuch der Physik*. Carl Hanser Verlag, München,Germany, 19. edition, 2007.

[38] H. Schultz. *Electron beam welding*. Abington Publishing, Cambridge, UK, 1993.

[39] V. Adam, U. Clauß, Dr.h.c.Dietrich v. Dobeneck, Dr.K. Thomas, and Dr.T. Löwer. *Elektronenstrahlschweißen-Grundlagen einer faszinierenden Technik*. pro-beam AG & Co. KGaA, Germany, 1. edition, 2011.

[40] S. Kou. *Welding Metallurgy*. John Wiley and Sons, New York, USA, 2nd edition, 2003.

[41] B. Dance and A. Buxton. An introduction to Surfi-Sculpt technology-new opportunities, new challenges. *7th International conference on Beam Technology*, 2007.

[42] B. Dance, I. Guy, E. Kellar, and C. James. Workpiece structure modification. 2004.

[43] U. Reisgen, C. Otten, H. Fischer, and C. Panfil. Electron beam structurisation of titanium materials for medical applications: potential for improved bone ingrowth behaviour. In *2nd International Electron Beam Welding Conference*. Aachen, 2012.

[44] Material certification by Baoji Titanium Industry Co, LTD; NO: C2013335026; DATE: Mar.21,2013; provided by company Hempel & Co Erze und Metalle GmbH & Co.

[45] *ATI Technical Data Sheet: ATI 15Mo Titanium Alloy*, volume 2. (4/23/2014).

[46] R. Boyer et al. *Materials Properties Handbook: Titanium Alloys*. ASM International, 1993.

[47] *Titan-Werkstoff mit Perspektive, Titanium-The material with a future*. ThyssenKrupp Schulte GmbH, 2012.

[48] J.R. Davis et al. *ASM Handbook Volume 2: Properties and Selection: Nonferrous Alloys and Special-Purpose Materials*. ASM International, 2007.

[49] Inspection Certificate of Quality by Western Superconduction Technologies Co. LTD; Cert No: 14091194; DATE: 2014-9-30; provided by company Hempel & Co Erze und Metalle GmbH & Co.

[50] J. Disegi. *Implant Materials. Wrought Titanium-15% Molybdenum*. Synthes (USA), 2009.

[51] W. Kleppmann. *Taschenbuch Versuchsplanung*. Carl Hauser Verlag, München, Germany, 2009.

[52] Minitab, Inc. "Einführung in Minitab 16", 2010.

[53] Moderne Topografiebewertung in der Papierindustrie, Wochenblatt für Papierfabrikation 1/2013.

[54] *IFM 2.0 Hilfedokument*. Alicona Imaging GmbH, 01.08.2006.

[55] W. Haas and B. Bertsche. Oberflächenbeurteilung-Rauheitsmessung, Uni Stuttgart, Allgemeines Praktikum Maschinenbau und Hauptfachversuch.

[56] Rauheitsmesssysteme von Jenoptik- Oberflächenkenngrößen in der Praxis, 1003 7108, 03/2015.

[57] Dr.C. Siemers. Optimierung der spanenden Bearbeitung der molybdänhaltigen Titanlegierung Ti15Mo für den Einsatz in der Medizintechnik: Schlussbericht, 2015.

[58] P. Günter. *Metallographisches, Keramographisches, Plastographisches Ätzen*. Gebrüder Borntraeger, Berlin-Stuttgart, 2006.

[59] B. Vrancken, L. Thijs, J.-P. Kruth, and J. Van Humbeeck. Microstructure and mechanical properties of a novel β titanium metallic composite by selective laser melting. *Acta Materialia*, 68:150–158, 2014.

[60] S.L. Sing, W.Y. Yeong, and F.E. Wiria. Selective laser melting of titanium alloy with 50 wt% tantalum: Microstructure and mechanical properties. *Journal of Alloys and Compounds*, 660:461–470, 2016.

[61] R. Poprawe. *Lasertechnik für die Fertigung-Grundlagen, Perspektiven und Beispiele für den innovativen Ingenieur.* Springer Berlin Heidelberg, 2005.

[62] A. Ott. *Oberflächenmodifikation von Aluminiumlegierungen mit Laserstrahlung: Prozessverständnis und Schichtcharakterisierung.* Herbert Utz Verlag GmbH, 2009.

[63] H.-J. Bargel and G. Schulze. *Werkstoffkunde.* Springer-Verlag Berlin Heidelberg, 2008.

[64] P. Zhanal. *Study of Phase Transformations in Ti Alloys.* Master's Thesis, Prague, 2014.

[65] W. Szkliniarz and G. Smolka. Analysis of volume effects of phase transformation in titanium alloys. *Journal of Materials Processing Technology*, 53(1-2):413–422, 1995.

[66] P. Barriobero-Vila, G. Requena, S. Schwarz, F. Warchomicka, and T. Buslaps. Influence of phase transformation kinetics on the formation of alpha in a beta-quenched Ti-5Al-5Mo-5V-3Cr-1Zr alloy. *Acta Materialia*, 95:90–101, 2015.

[67] Z. Ignjatov. *Phasenbestimmung bei Titan mittels Dilatometrie.* Master's Thesis, 2005.

[68] L. Reimer. *Scanning Electron Microscopy-Physics of Image Formation and Microanalysis.* Springer-Verlag Berlin Heidelberg, 2 edition, 1998.

[69] Y. Zheng. *Nucleation Mechanisms of refined Alpha Microstructure in Beta Titanium Alloys.* Dissertation, 2013.

[70] A. Devaraj. Phase separation and second phase precipitation in beta titanium alloys. *Material Science and Engineering*, 2011.

[71] F.F. Cardoso, P.L. Ferrandini, E.S.N. Lopes, A. Cremasco, and R. Caram. Ti-Mo alloys employed as biomaterials: Effects of composition and aging heat treatment on microstructure and mechanical behavior. *Journal of the Mechanical Behavior of Biomedical Materials*, 32:31–38, 2014.